Studies of Mixing and Combustion in Hypervelocity Flows with Hot Hydrogen Injection

Thesis by

Jacques Bélanger

In Partial Fulfillment of the Requirements

for the Degree of

Doctor of Philosophy

1993

(Submitted April 9, 1993)

To my parents.

Acknowledgments

My gratitude goes to the whole GALCIT community for making it such a challenging place to be, but at the same time such a friendly one. It would be impossible for me to name every professor, every student, every technician and every secretary that has helped me over the years. The only thing I can do is to thank you, each one of you, for making this work possible.

Research in a big facility, like T5, would not be possible without the help and advice of each member of the team, thanks to all of you. I am particularly grateful to Simon Sanderson, Eric Cummings, Prof. Sturtevant, and Bahram Valiferdowsi.

Thanks to George Yates and the Caltech Ice Hockey Team not only for taking me away from my books twice a week, but also for all those great memories that I will be able to take back with me.

I would like to express my thanks to all the friends who made these years at GALCIT enjoyable, especially Michèle, Andrea and Nicole, who were always there to listen and to support me.

I would also like to thank my family for their continuous support; they never failed to make me believe in myself.

Finally, and most importantly, I would like to express my deepest gratitude to Professor Hans Hornung. I will always cherish the time he shared with me as an advisor and as a friend, and I hope that I will be able to communicate to others what he was able to teach me.

This research was supported by the Fonds F.C.A.R. of Québec and NASA, under grant NAG-1-1209.

Abstract

The ability to build an air-breathing single-stage-to-orbit propulsion system requires examination of key elements such as turbulent mixing rates, especially at the "zero shear" fuel-air mixing condition, and combustion efficiency. The required data can only be obtained in experiments which simultaneously match the flight total pressure and total enthalpy as well as the fuel conditions. GALCIT, with its new free piston shock tunnel T5, has the capability to do some of these combustion experiments. But prior to these tests, it was felt that there was a need to simulate the gas dynamical processes in the free piston shock tunnel and also in a new combustion driven shock tunnel built for these experiments so that both systems could be used as efficiently as possible. The numerical code helped explain the piston motion in the free piston shock tunnel. The code was also very useful for the design of the combustion driven shock tunnel.

Because hydrogen has to be injected into the combustion chamber of the propulsion system after being used as a cooling fluid, a combustion driven shock tunnel was built to reproduce this "hot" hydrogen fuel. The system has been used successfully to supply hydrogen at up to 1500 K for the experiments. To reduce the complexity of the problem, a very basic configuration for the hydrogen injection system was tested. This was first done with an injection system mounted flush with the surface of a flat plate in the test section of T5. Different test conditions as well as Mach 2 and 5 nozzle injectors at angles of 15^{o} or 30^{o} were tested to determine criteria for significant combustion. Lower limits in pressure and enthalpy were found where hydrogen combustion becomes very limited using this "hot" hydrogen fuel. The second set of experiments still used an injection system mounted flush with the surface but involved a small combustor model previously tested in the hypervelocity HYPULSE facility. Low pressure experiments were performed to reproduce some of the HYPULSE tests and excellent agreement was found. Experiments at high pressure were also performed to better match the real flight total pressure and some hydrogen combustion was detected in these tests.

Table of Contents

List of Figures

List of Tables

List of Symbols

a	speed of sound
a_1	initial speed of sound in the driven section
a_4	speed of sound in the driver section at diaphragm rupture
a_{air}	initial speed of sound of the air behind the piston
A	section area
A_1	section area of the driven section
A_4	section area of the driver section
A_o	section area of the piston
A^*	driven section end-wall throat area
b_1	virtual postion of the minus characteristic at $t = 0$
b_2	virtual postion of the piston at $t = 0$
c	specific heat
c_p	specific heat at constant pressure
d	exit diameter of the injector
F_+ , F_-	Riemann invariants
g	shock tube area change factor
h	enthalpy
k	thermal conductivity
L	total length of the driver section
m	mass of the piston
Ms	incident shock Mach number
p	static pressure
p_{air}	initial pressure of the air behind the piston
p_{dif}	pressure difference between the front and the back of the piston
p_{driver}	initial pressure in the driver section before piston launch
P_0	stagnation pressure in the driven section during test time
P_1	initial pressure in the driven section
P_4	initial pressure in the driver section

P_4'	stagnation pressure in the driver section after combustion
Pr	Prandtl number
$\dot{q}$	heat flux
Q	cumulative heat input
r	recovery factor
s	entropy
St	Stanton number
t	time
T	temperature
T_0	stagnation temperature in the driven section during test time
T_1	initial temperature in the driven section
T_4	initial temperature in the driver section
T_4'	stagnation temperature in the driver section after combustion
u	flow velocity
u_w	end-wall velocity
v	piston velocity
W	shock velocity
x	location
γ	ratio of specific heats
γ_1	ratio of specific heats for the gas in the driven section
γ_4	ratio of specific heats for the gas in the driver section
γ_{air}	ratio of specific heats for the air behind the piston
δ	boundary layer thickness
λ	compression ratio
ρ	density

Chapter 1
Introduction

The ability to build an air-breathing single-stage-to-orbit vehicle in the near future resides largely in the understanding of the combustion process which occurs in a scramjet engine operating in the hypervelocity regime ($M_\infty > 10$). The main issues related to this type of engine cannot be extrapolated with confidence from the accumulated supersonic and low hypersonic ($M_\infty \leq 8$) scramjet data base. Some of the key elements requiring examination are the fuel penetration, the turbulent mixing rates, especially at the "zero shear" fuel-air mixing condition, and the combustion efficiency. Ultimately, the required data can only be obtained in experiments which simultaneously match the flight total pressure and total enthalpy as well as the fuel conditions.

The free piston shock tunnel T5 has been built at GALCIT to experimentally study flows with free stream velocity up to 6 km/s. Some information about T5 is presented in section 4.2 but for more details see Hornung (1988), Hornung and Bélanger (1990), or Hornung et al. (1991). The free piston shock tunnel T5 is a suitable facility for studying the flow fields near a vehicle traveling at those speeds, and also for air-breathing propulsion systems for such a vehicle. In air-breathing propulsion systems of this kind, the fuel used, most likely hydrogen, must be injected into the combustion chamber after being used as a cooling fluid for critical parts of the vehicle. This process significantly increases the enthalpy of the fuel, so a "hot" hydrogen supply system had to be designed to reproduce such hydrogen fuel in a propulsion type experiment in T5.

Only a few practical ways are available to produce such "hot" hydrogen. A Ludwieg tube, in which the temperature of the hydrogen is increased significantly before the test by heating elements, is one. This technique has been used extensively and is

considered a proven technology. For a detailed description of such a system, there is an excellent reference book by Lukasiewicz (1973); it also contains a description of the free piston shock tunnel. The biggest problem with the Ludwieg tube is that the maximum temperature is limited to 1000 K. There is also a safety concern with this technique, since for 5 to 10 minutes before the test, there is a tube inside the laboratory with hydrogen at around 20 MPa and near 1000 K. Thus, due to the limited temperature range and the safety concern, this method was not chosen. Rocketdyne, during tests with T5 in 1991-92, used this technique successfully, but compromised on their temperature requirements and added many necessary safety features on their supply system.

Another technique that could be used is an electrically heated shock tunnel, where the driver gas, most likely hydrogen, is heated a few minutes before the test. Such a driver gas can be used to create a strong shock even in a hydrogen-filled driven section of the shock tunnel. A temperature of 2000 K at the end of the driven section can be reached with this technique but, once again, the "steady" heating of the hydrogen in the driver section and the large amount of hydrogen involved are serious safety concerns.

The method chosen to supply the "hot" hydrogen in our device is a combustion driven shock tunnel. It offers an excellent range of temperatures and pressures and is also viewed as the safest method which is very important. This technique minimizes the total amount of hydrogen, does not require electrical heating elements, and is the safest of the three methods.

In combustion driven facilities, the driver gas is usually a mixture of mainly helium with a stoichiometric mixture of hydrogen and oxygen. The combustion of the mixture creates a high pressure driver gas which has a speed of sound of about 2000 m/s. This high speed of sound when used with a hydrogen driven gas will produce hydrogen temperatures up to 2000 K. The tunnel is used in a reflected shock mode with the hydrogen injection nozzle at the end of the driven section.

This combustion-driven shock tunnel can also be used for other purposes. Used with air as the driven gas, it is possible to get shock waves of about Mach 6, well into the range of conditions where dissociating flows can occur, making it an excellent tool for

instrumentation development. The combustion-driven shock tube offers a simple inexpensive alternative to T5 for this purpose, with a turn-around time of less than one hour.

The construction of T5 at GALCIT was also the main driving force to develop an integrated computer program able to simulate the gas-dynamical processes in such a facility. All the necessary tools to simulate the shock tunnel are well known; the major problem was to incorporate all these into one program. A need to help in the design of the combustion driven shock tunnel and predict its performance was also felt. The result is a versatile computer code using a characteristics method that can not only simulate the flow of shock tunnels like T5 but also the flow of more commonly used shock tubes.

The program begins with the rupture of the main diaphragm between the driver section and the driven section, and usually ends at a time predetermined by the user. The piston velocity at diaphragm rupture for the free piston shock tunnel simulation is determined using the analysis of Hornung (1988) and computed in a separate program. If, like in the case of T5 or the case of the combustion driven shock tunnel, a nozzle and a second diaphragm can be installed at the driven section end-wall, the program can evaluate the flow rate through the nozzle and determine when driver gas contamination will occur. It does not evaluate the conditions at the exit of that nozzle, which is the test section of the facility. To get this information, one can use the pressure and temperature at the driven section end-wall given by the program as inputs to a high enthalpy nozzle flow program like the quasi one-dimensional reacting nozzle flow code NENZFG (Lordi, 1965) or the fully two-dimensional code SURF (Rein, 1989).

Once all the pieces of this research were put together, a first set of experiments in T5 was started. A very basic configuration for the hydrogen injection system was used to reduce the complexity of the problem and give a better insight into the combustion process. For these tests, the exit nozzle of the hydrogen injection system was mounted flush with the surface of a flat plate in the test section of T5 as shown in figure 1.1. To minimize the free-stream momentum and total pressure losses and improve fuel distribution, the hot hydrogen is injected at angles of 15^{o} or 30^{o} relative to the flow

direction. Mach 2 and Mach 5 nozzles were tested to see if the fuel injection temperature changed the combustion characteristics.

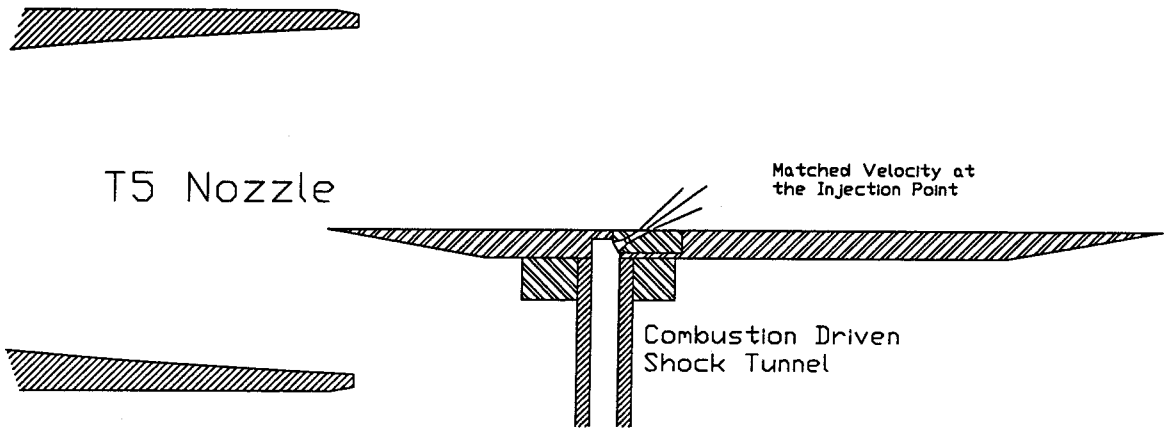

Figure 1.1 Sketch of the flat plate and the hydrogen injection system for the experiments presented in chapter 5.

These combustion experiments were done with matching velocity at the injection point between the main flow of T5 and the hydrogen jet. This is considered a critical point in a single-stage-to-orbit flight trajectory called the "zero shear" fuel-air mixing condition. Air and nitrogen flows were tested to see differences between combustion and non-combustion experiments. Furthermore, to understand the differences between the air and the nitrogen flow, the same tests were repeated with helium injection instead of the hydrogen.

The second set of experiments involved a small combustor model instead of the flat plate. This small combustor was previously tested in the HYPULSE facility expansion tube at the General Applied Science Laboratories in Ronkonkoma, New York. The combustor is a rectangular duct with a cross section of 50.8 mm by 25.4 mm and length of 711 mm. Low pressure experiments with cold hydrogen injection were performed here to reproduce the HYPULSE tests. The combustion driven shock tunnel was converted into a Ludwieg tube during these tests to provide the cold hydrogen.

Experiments with hot injection at high pressure were also performed to better match the real flight total pressure.

The thesis is divided into seven chapters, including this introduction. Chapter 2 describes the numerical code and shows sample simulations of the free piston shock tunnel T5 and the combustion driven shock tunnel. Chapter 3 is a description of the actual combustion driven shock tunnel built and its operation, including a section on the overall efficiency of the system. A short presentation of the free piston shock tunnel T5 with a description of the instrumentation, the data acquisition system, and the flow visualization techniques is presented in chapter 4. The first set of experiments on the flat plate is then presented in chapter 5 followed by the experiments with the combustor in chapter 6. Chapter 7 is an overall conclusion of the research.

Chapter 2
Numerical Simulations

2.1 Introduction

The numerical code described here started as a simple calculation of shock tube flows using a characteristics method for the flow behind the shock and a simple subroutine to evaluate the strength of the incident shock and the reflected shock using perfect gas equations. Later, an area change between the driver and the driven part of the shock tube was added using quasi one-dimensional steady flow relations in that part of the system. Other improvements involved the addition of a nozzle at the end of the driven section to simulate shock tunnels and the option of a moving end-wall in the driver section, so that a free piston shock tunnel, like T5 at GALCIT, could be simulated. Most of the elements needed for the code were first introduced to the author in the Non-Steady Gasdynamics course by Sturtevant (1989). Efforts to introduce viscous losses due to boundary layer in the driven section have not been successful and will not be presented here.

The real difficulty was to integrate the real gas effects into the code. It was necessary to do so if any attempt to simulate a facility like T5, where the stagnation temperature at the end of the driven section can reach close to 10,000 K, was to be made. Since most of the oxygen and some of the nitrogen is dissociated at these high temperatures, real gas simulation is essential.

The perfect gas characteristics method can be modified to compute real gas flows. The approach taken assumes the gas to be in chemical equilibrium. This is a good approximation in the driven section of a free piston shock tunnel because the gas temperature and pressure are so high that the gas can almost always be considered in equilibrium. The only part of the shock tunnel where nonequilibrium effects are important

is the nozzle and the nozzle flow is not computed in these simulations. The program evaluates the flow up to the nozzle throat by using equilibrium approximations, but does not go further downstream.

The program allows only the driven gas to be real; the driver gas is always considered perfect. This is not a serious restriction because a monatomic driver gas without gas imperfections is desirable. By far the most used driver gas in free piston shock tunnels is helium, and for some tests a small percentage of argon is added to the helium, making this driver gas "perfect" even for very high temperatures. The maximum temperature of the driver gas is 5000 K where neither helium nor argon shows gas imperfections.

Two important subroutines of the program involved in the real gas characteristics method were taken from McIntosh (1971) and are used to evaluate the equilibrium conditions of the flow and composition of the gas either after an isentropic process or after a shock. The details of these two subroutines will not be discussed here. A complete description is included in Lordi et al.(1965).

This chapter includes a research review of numerical simulations of free-piston shock tunnels, section 2.2. Section 2.3 looks at the basic characteristics method used for perfect gas and for real gas. The integration into the program of the area change between the driver and driven section and the driven section end-wall with a draining nozzle using quasi one-dimensional relations is discussed in section 2.4 . The decelerating piston, or the driver section end-wall motion, and the special case of an interaction between the shock and the interface are discussed in section 2.5. Section 2.6 details three sample calculations, two involving the free piston shock tunnel T5 and the third involving a combustion driven shock tunnel. Concluding remarks are presented in section 2.7.

More examples and a detailed description of the numerical code itself can also be found in the GALCIT Report FM 90-3 by Bélanger.

2.2 Research Review

The construction of large free-piston shock tunnels with piston mass of up to 800 kg, e.q., HEG in Germany (see Eitelberg et al., 1991), made it crucial to understand very well the piston motion. Hornung (1988) addressed that problem and was able to predict the piston motion quite accurately even with a rather simple model. The equations developed in Hornung's GALCIT Report for the first part of the piston trajectory up to the main diaphragm rupture are used in the present program for the T5 simulations shown in section 2.6.

In 1989, when the characteristics program was written, there were also efforts by Lacey and Long (1990) at FluiDyne and by Maus et al. (1992) at Calspan to simulate complete free-piston shock tunnels. Lacey used a finite difference based computational approach but did not include real gas effects or viscosity in his simulations. The work by Maus is more extensive and covers problems such as friction losses and heat transfer to the walls. Simulations of T5 experiments with his program were very successful.

In the last few years, there have also been efforts to simulate free-piston shock tunnels by Jacobs (1993). Jacobs uses an approach very close to the one used by Maus with the same features. The biggest weakness with both programs is the inability to realistically determine the position of the interface between the driver and driven gas. This inability leads to an optimistic estimate of the time when contamination of the driven gas by the driver gas will occur.

2.3 Method of Characteristics for Unsteady One-Dimensional Flows

A review of the main equations of the method of characteristics for unsteady flows will be presented here. For the case of a perfect gas, presented in section 2.3.1, the derivation of the equations and the application to different interactions is very straight-forward. The material presented here can be found in books on compressible fluid dynamics; Anderson (1982) and Liepmann and Roshko (1957) were used extensively in

the present work. In the case of a real gas, presented in section 2.3.2, the material is much less common. Most of the material was found in Becker (1965) and Anderson (1989).

2.3.1 Perfect Gas

The required equations are the unsteady one-dimensional continuity equation and the momentum equation,

$$\frac{\partial \rho}{\partial t} + \frac{\partial (\rho u)}{\partial x} = 0 \,, \tag{2.1}$$

$$\rho \frac{\partial u}{\partial t} + \rho u \frac{\partial u}{\partial x} + \frac{\partial p}{\partial x} = 0 \,. \tag{2.2}$$

Assuming the flow to be isentropic (ds = 0), it can be shown that the compatibility equations

$$du \pm \frac{dp}{\rho a} = 0 \tag{2.3}$$

hold along paths called characteristic lines

$$\frac{dx}{dt} = u \pm a \,, \tag{2.4}$$

where the speed of sound, a, is defined by

$$a = \sqrt{\left(\frac{\partial p}{\partial \rho}\right)_s} \,. \tag{2.5}$$

For the case of an isentropic flow with a calorically perfect gas, we can derive

$$\frac{dp}{\rho} = \frac{2a}{\gamma - 1} da \,. \tag{2.6}$$

Substituting equation 2.6 in equation 2.3 and integrating along the characteristic lines we get

$$F_+ = u + \frac{2a}{\gamma - 1} = \text{constant (along plus characteristic)}, \tag{2.7}$$

$$F_- = u - \frac{2a}{\gamma - 1} = \text{constant (along minus characteristic)}. \tag{2.8}$$

Solving these two equations for the intersection point of a plus characteristic and a minus characteristic gives

$$u = \frac{1}{2}(F_+ - F_-), \tag{2.9}$$

$$a = \frac{\gamma - 1}{4}(F_+ - F_-). \tag{2.10}$$

These results are summarized in figure 2.1 .

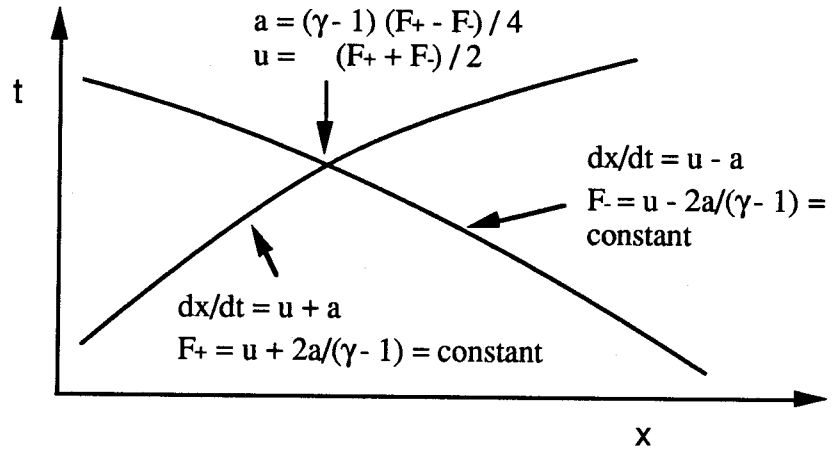

Figure 2.1 Illustration of the intersection of characteristic lines in the x-t plane.

There are also three other types of intersection that can occur in the flow. A characteristic line can reach one of the end-walls and be reflected. A characteristic line can intersect an interface between two gases and create a transmitted wave and a reflected one, or finally, it can intersect a shock wave and create a characteristic wave in the wake of the shock, and alter the shock strength.

In the case of the intersection of a plus characteristic line with the wall, as in figure 2.2 , a minus characteristic will be created. Using equation 2.9 with $u=u_w$, we can

determine F_- . Then using equation 2.10, we can determine a, the speed of sound at the intersection point.

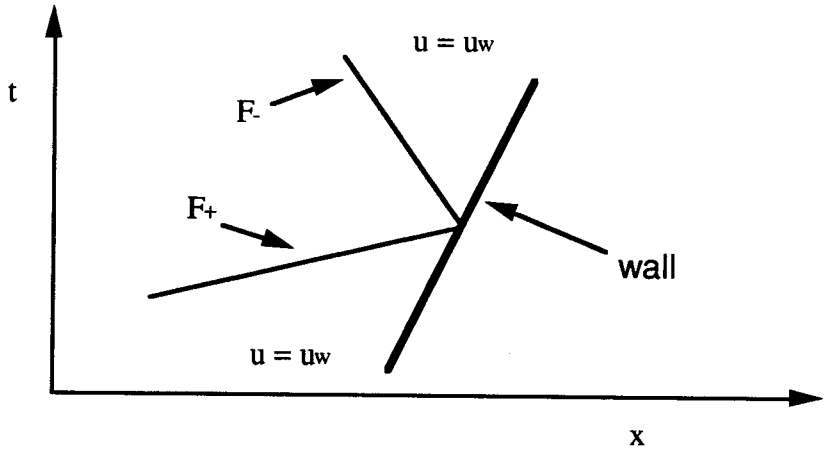

Figure 2.2 Intersection of a characteristic line and a wall.

For the case of an interaction of a plus characteristic with the interface between two different gas conditions, a transmitted plus characteristic and a reflected minus characteristic will be created, as in figure 2.3 . The incident conditions on both sides of the interface are known. An iterative approach is used to determine the exact values of $(F_-)_r$ and $(F_+)_t$ so that the pressure and the velocity, on the two sides of the interface, are equal after the interaction.

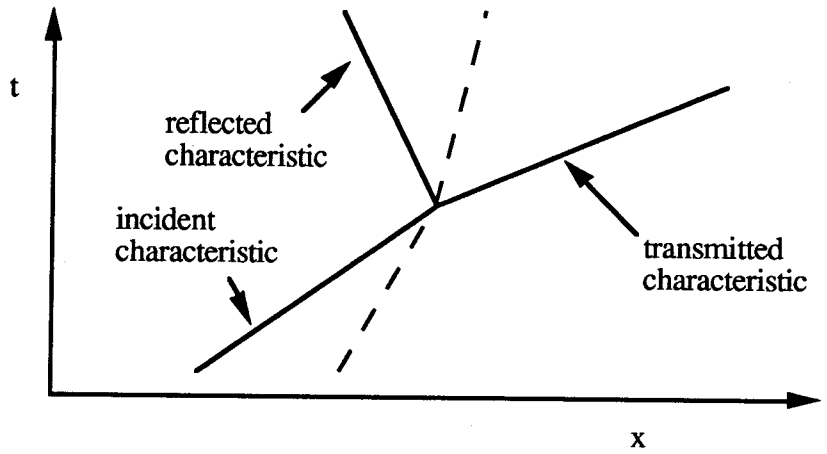

Figure 2.3 Intersection of a characteristic line and an interface.

Finally, for the case of a plus characteristic and a shock, we expect a minus characteristic to be reflected, as shown in figure 2.4 . An iterative approach is also used

here to determine the new shock velocity and strength of the minus characteristic $(F_-)_r$. This is done by getting the velocity and pressure to be the same on both sides of the streamline shown in figure 2.4 . All the other thermodynamic variables are not constant across that streamline, but the entropy jump across the streamline is considered to be small and the flow field behind the shock is assumed isentropic. This assumption is not true in the case of large variations in the shock speed and can introduce some error in the computation.

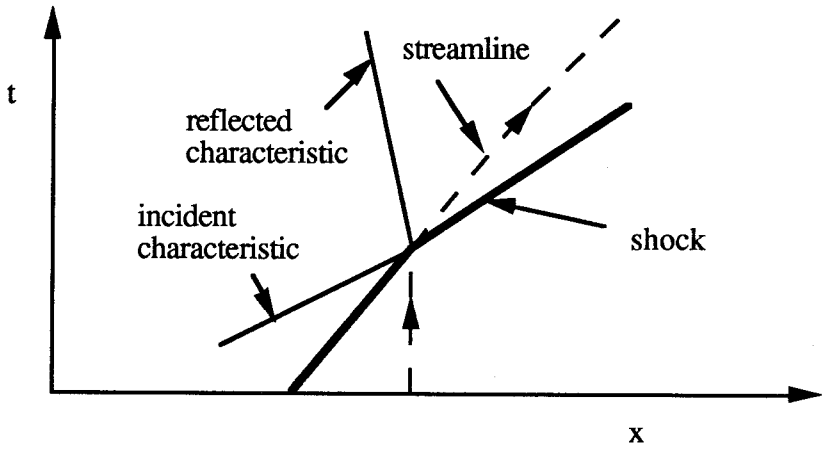

Figure 2.4 Intersection of a characteristic line and a shock.

In the case of an incident minus characteristic for the three types of intersection presented, the reader can make mirror images of figures 2.2 and 2.3. In the case of figure 2.4, there is no reflected wave, but instead, only a transmitted minus characteristic in the wake of the shock.

2.3.2 Real Gas

The equations for the real gas case are the same continuity equation (eq. 2.1) and momentum equation (eq. 2.2) as in the case of perfect gas. However, this kind of flow generally involves very strong shocks, and because the strength of the shock varies with time, it implies that behind the shock the flow can no longer be considered isentropic. The method of characteristics for this case is presented in Becker (1965) and uses the equilibrium speed of sound as defined in equation 2.5. It can be shown that this type of

flow is isentropic, but only along streamlines (see Becker 1965 or Anderson 1989) . It is then possible to define three different characteristic lines.

$$\frac{dx}{dt} = u + a\,, \qquad \frac{dx}{dt} = u - a\,, \qquad \frac{dx}{dt} = u\,. \tag{2.11}$$

To each of these characteristic lines, the corresponding compatibility equation is

$$dp + \rho a du = 0\,, \tag{2.12}$$

$$dp - \rho a du = 0\,, \tag{2.13}$$

$$ds = 0\,. \tag{2.14}$$

The solution of this set of equations cannot be formulated in closed form like in the case of the perfect gas, but an approximate method can be used. If points A and B of figure 2.5, representing an x-t diagram, are known, we can rewrite equation 2.12 and 2.13 in the form

$$p(P) - p(A) + \rho(A)a(A)[u(P) - u(A)] = 0\,, \tag{2.15}$$

$$p(P) - p(B) - \rho(B)a(B)[u(P) - u(B)] = 0\,. \tag{2.16}$$

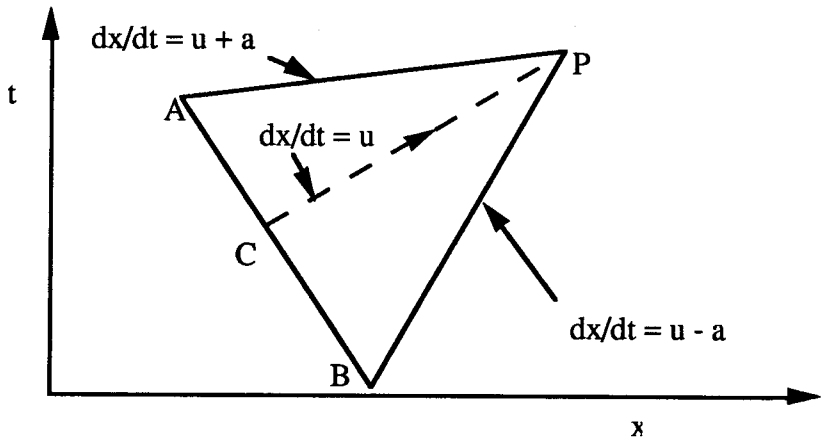

Figure 2.5 Illustration of the characteristic lines for real gas.

These two equations allow us to determine the unknowns p(P) and u(P). From there, it is possible to determine the point C between A and B. A linear interpolation between the two points gives us s(C) and, by equation 2.14, s(P). Knowing s(P), u(P),

and p(P), all other thermodynamic variables can be evaluated. The straight lines AP and BP are in reality the local tangents to the characteristics, so this approximate method gives the correct results only for a sufficiently fine mesh.

If between A and P, or B and P, the variation in the product ρa is significant, then an iterative approach may be used. Instead of working with equations 2.11 to 2.14, the values of the previous approximation can be used to determine, with better precision, the location and thermodynamic variables at the point P:

$$\frac{dx}{dt} = \frac{u(A) + u(P) + a(A) + a(P)}{2}, \tag{2.17}$$

$$\frac{dx}{dt} = \frac{u(B) + u(P) - a(B) - a(P)}{2}, \tag{2.18}$$

$$\frac{dx}{dt} = \frac{u(C) + u(P)}{2}, \tag{2.19}$$

$$\rho a = \left(\frac{\rho(A) + \rho(P)}{2}\right)\left(\frac{a(A) + a(P)}{2}\right), \tag{2.20}$$

$$\rho a = \left(\frac{\rho(B) + \rho(P)}{2}\right)\left(\frac{a(B) + a(P)}{2}\right). \tag{2.21}$$

In the subroutines of the program, there is no iteration over the position of the point P; a loop is occasionally used only for equations 2.20 and 2.21, when the variation of the value of ρa is significant.

As in section 2.2.1, there are the same three other types of intersection that must be considered. They occur when a plus or minus characteristic line intersects one of the walls, the interface, or the shock.

In the case of the intersection of a plus characteristic line with the wall (figure 2.2), $u(P) = u_W$ is presumed known, and by using 2.15, we can determine p(P). We can also use the fact that the wall trajectory is a streamline along which $ds = 0$. Then, from the initial condition, all the thermodynamic variables at the intersection of the wall and the plus characteristic may be determined.

For the case of an interaction of a plus characteristic and the interface between two different gases, a transmitted plus characteristic and a reflected minus characteristic are created, as in the perfect gas case shown in figure 2.3 . The initial conditions on both sides of the interface are known. Using equations 2.15 and 2.16, it is possible to determine the velocity and the pressure after the interaction, knowing that they must be the same on both sides of the interface. That interface is also a streamline, so $\Delta s = 0$, which allows us to evaluate iteratively all thermodynamic variables on each side of the interface. In the case where one side of the interface is a perfect gas, a combination of the method just explained and the one described in section 2.1 is used iteratively.

For the case of a plus characteristic and a shock, once again, the solution is similar to the case described for a perfect gas. The same iterative approach is used to match the velocities and pressures of the flows going through the reflected minus characteristic and the shock, respectively. The shock calculation gives the entropy of the flow at the intersection point and is used later as the entropy along the following streamline.

As before, these interactions can easily be converted to the case of an incident minus characteristic.

2.4 Steady Expansion

Quite often in shock tunnel technology, one encounters area changes. These changes usually occur in the driver section near the main diaphragm or at the end wall of the driven section where a nozzle can be installed. These two cases are presented separately, because the first case does not imply that the flow at the area change is sonic, while the second case usually does.

2.4.1 Contraction in the Driver Section

The driver gas is considered perfect. The equations governing this part of the flow are the quasi one-dimensional continuity equation

$$\rho_2 u_2 A_2 = \rho_3 u_3 A_3 \,, \qquad (2.22)$$

and the simplified energy equation,

$$\frac{u_2^2}{2} + h_2 = \frac{u_3^2}{2} + h_3 \, . \tag{2.23}$$

The indices refer to figure 2.6 .

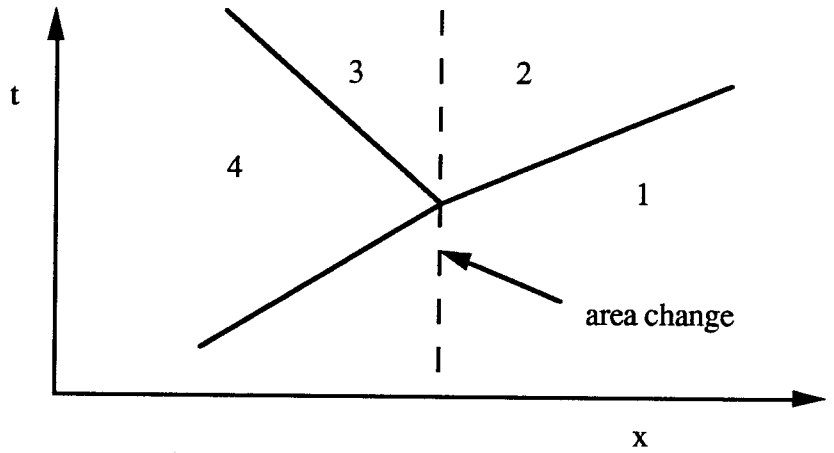

Figure 2.6 Characteristic lines with an area change.

Using the fact that for a perfect gas, $h = a^2/(\gamma - 1)$, and

$$\frac{\rho_3}{\rho_2} = \left(\frac{a_3}{a_2}\right)^{\frac{2}{\gamma - 1}} , \tag{2.24}$$

the problem is reduced to four unknowns, u_2, u_3, a_2 and a_3. The two additional equations required, other than 2.22 and 2.23, come from the non-steady flow between regions 1 and 2 and between regions 4 and 1. They give

$$u_1 - \frac{2}{\gamma - 1} a_1 = u_2 - \frac{2}{\gamma - 1} a_2 , \tag{2.25}$$

$$u_4 + \frac{2}{\gamma - 1} a_4 = u_3 + \frac{2}{\gamma - 1} a_3 , \tag{2.26}$$

where the conditions in regions 1 and 4 are known.

These equations can be reduced to a system of two equations, where the unknowns are u_2 and u_3 or, as in the program, a_2 and a_3. An iterative method is then used to derive

the solution where the velocity of the flow at the exit of the contraction must be subsonic or sonic ($u_2 \leq a_2$). Equations 2.25 and 2.26 then give the velocities.

Figure 2.6 shows the case where a plus characteristic reaches the contraction, but a minus characteristic coming from region 1 would be solved exactly the same way.

2.4.2 End-Wall Nozzle of Driven Section

The gas in the driven section of the tunnel can be a perfect gas or a real gas. These two possibilities are studied separately. This case is different from the contraction case because here the throat of the nozzle is always considered sonic, implying that the pressure on the downstream side of the nozzle is sufficiently low to keep it sonic. For the case of a perfect gas, we have the basic quasi one-dimensional equations from Anderson (1982) and, using indices from figure 2.7, we can derive

$$u_2 = a_2 \frac{A^*}{A_2}\left[\left(\frac{2}{\gamma - 1}\right)\left(1 + \frac{\gamma - 1}{2}\left\{\frac{u_2}{a_2}\right\}^2\right)\right]^{\gamma + 1 / 2(\gamma - 1)} . \qquad (2.27)$$

Also, regions 1 and 2 are connected by a constant F_+ which is translated by the equation

$$u_1 + \frac{2}{\gamma - 1}a_1 = u_2 + \frac{2}{\gamma - 1}a_2 , \qquad (2.28)$$

where u_1 and a_1 are known. An iterative approach is used to solve for u_2 and a_2.

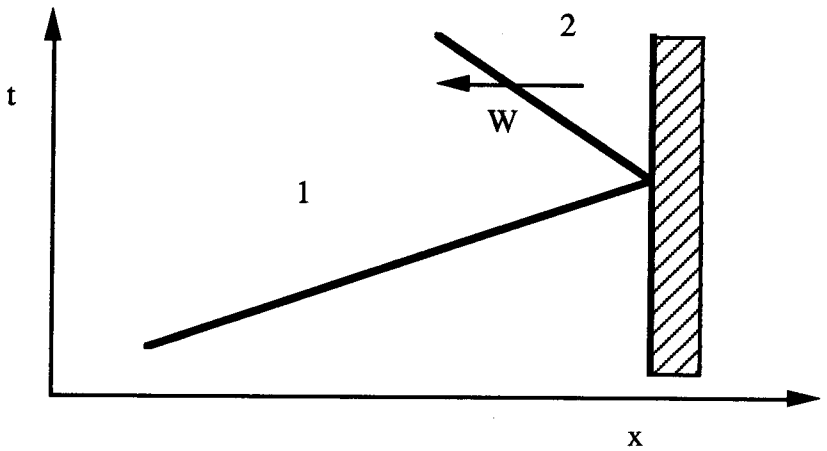

Figure 2.7 Characteristic line reaching end-wall with a nozzle throat. The nozzle itself is not represented in this x-t diagram.

In the case of the reflected shock, as shown in figure 2.7 , equation 2.28 is replaced by

$$\frac{p_2}{p_1} = 1 + \frac{2\gamma}{\gamma + 1}\left[\frac{(u_1 + W)^2}{a_1^2} - 1\right], \tag{2.29}$$

$$\left(\frac{a_2}{a_1}\right)^2 = \frac{T_2}{T_1} = \frac{p_2}{p_1}\left(\frac{\frac{\gamma + 1}{\gamma - 1} + \frac{p_2}{p_1}}{1 + \frac{\gamma + 1}{\gamma - 1}\frac{p_2}{p_1}}\right), \tag{2.30}$$

where W is the velocity of the reflected shock and the conditions in region 1 are known.

A first approximation is made for W. By using 2.29 and 2.30, a_2 can be determined. Equation 2.31 finally gives u_2.

$$u_2 = u_1 - \frac{a_1}{\gamma}\left(\frac{p_2}{p_1} - 1\right)\left(\frac{\frac{2\gamma}{\gamma + 1}}{\frac{p_2}{p_1} + \frac{\gamma - 1}{\gamma + 1}}\right)^{1/2} . \tag{2.31}$$

Now, if the flow velocity (u) and the speed of sound (a) in region 2 can also satisfy 2.27, the choice of W was correct. Alternatively, we need to iterate over the shock velocity W.

The approach is not as simple for the real gas. We assume that the flow in the nozzle is isentropic, in chemical equilibrium (as it usually is near the throat), and that the total enthalpy is conserved. The connection between regions 1 and 2 shown in equation 2.28 for the perfect gas case is replaced here by the approximation (as equation 2.15)

$$p_1 + \rho_1 a_1 u_1 = p_2 + \rho_1 a_1 u_2 . \tag{2.32}$$

The iteration starts with a guess on u_2. A linear interpolation gives the entropy, and p_2 can be determined using 2.32. From there, the necessary pressure for sonic flow at the throat can be evaluated. Then all the thermodynamic conditions at the throat may be determined. The continuity equation (eq. 2.33) is used between region 2 and the throat to get a better approximation of u_2. Usually, two or three iterations are sufficient.

$$\rho_2 u_2 A_2 = \rho^* u^* A^* . \tag{2.33}$$

In the case of the reflected shock, the unsteady equation (eq. 2.32) does not apply and is replaced by a more complex shock relation. Knowing the initial conditions in region 1 of figure 2.7 and iterating on the shock velocity, the conditions in region 2 can be found to satisfy equation 2.33.

2.5 Special Cases

One of the objectives of this work is to simulate a free piston shock tunnel. Therefore the velocity of the piston at the end of the driver section had to be reproduced correctly. The way this was accomplished is presented in part one of this section. Also a special case, always present in a shock tunnel, is the interaction between the reflected shock and the interface. This special case is presented in part two.

2.5.1 Driver Gas End-Wall Velocity

In the program, the exact position of the intersection between the moving driver section end-wall (the piston in the case of a free-piston shock tunnel) and a minus characteristic heading toward it is determined by solving

$$x = - \frac{A_o p_{dif} t^2}{2m} + v_o t + b_1 , \tag{2.34}$$

$$x = (u - a)t + b_2 . \tag{2.35}$$

Equation 2.34 represents the driver section end-wall (piston) position as a function of time. A_0 is the end-wall area, p_{dif} is the pressure difference between the front and the back of the end-wall kept from the previous interaction end-wall-minus characteristic, m is the mass of the piston, v_0 is the velocity of the piston also kept from the previous interaction with a minus characteristic, and b_1 is the virtual position of the piston at $t = 0$. Equation 2.35 gives the position of the minus characteristic coming to the piston.

The velocity of the piston is then evaluated using equation 2.36

$$v = -\frac{A_o p_{dif} t}{m} + v_o \,. \tag{2.36}$$

The procedure is then exactly as explained in section 2.2.1 for the case of an intersection between a characteristic line and an end-wall. $u_w = v$ is used to determine the strength of the plus characteristic coming out of the interaction.

If a non-moving driver section end-wall is needed, as in the case of a combustion shock tube, the input file sets the end-wall velocity to zero and maintains it for the entire computation.

2.5.2 Shock Interface Relation

When the reflected shock reaches the interface, as shown in figure 2.8, a transmitted shock goes through and a compression wave or an expansion wave is reflected. This reflected wave disappears only in the case of a perfectly tailored condition.

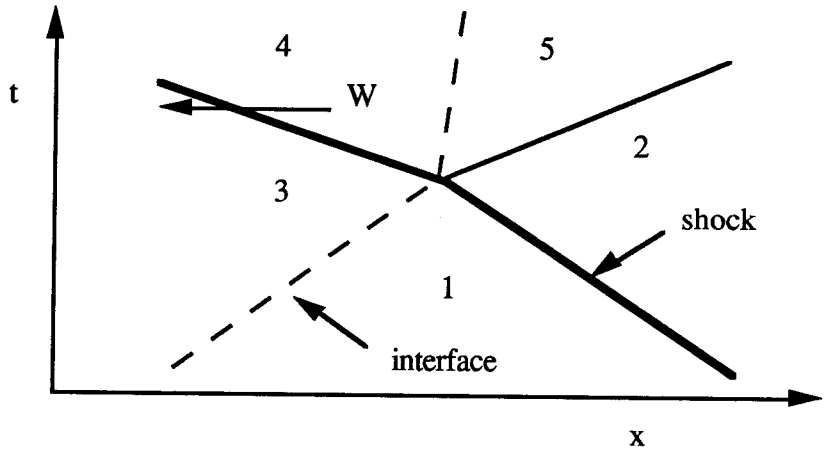

Figure 2.8 Shock interface interaction.

Regions 2 and 3 are known. To solve the problem, an iterative approach is used again. An initial estimation of W is made and, using equations 2.29 , 2.30 and 2.31 between regions 3 and 4, the conditions in region 4 are evaluated.

Physically we also need $p_4 = p_5$ so that, in the case of a perfect gas in region 2 and 5 and an isentropic process, we can determine a_5 by

$$\frac{a_5}{a_2} = \left(\frac{p_5}{p_2}\right)^{\gamma - 1 / 2\gamma} . \tag{2.37}$$

Then, u_5 can be determined by the non-steady relation between regions 2 and 5 :

$$u_2 - \frac{2}{\gamma - 1} a_2 = u_5 - \frac{2}{\gamma - 1} a_5 . \tag{2.38}$$

If $u_5 \neq u_4$, the iteration process is repeated with a different value for W.

If the gas in regions 2 and 5 is a real gas, equations 2.37 and 2.38 are replaced by the approximate relation

$$p_2 - \rho_2 a_2 u_2 = p_5 - \rho_2 a_2 u_5 . \tag{2.39}$$

2.6 Sample Calculations

The numerical calculations presented reproduce the conditions of actual tests done in T5 and in the combustion driven shock tunnel. In all cases, the simulation starts at diaphragm rupture and ends when the reflected shock arrives at the area change between the driver and the driven section.

For the T5 simulations, the velocity of the piston at diaphragm rupture is determined using the analysis by Hornung (1988). In that analysis, the equation of motion of the piston during the driver gas compression is found to be represented by

$$- m \frac{d^2x}{dt^2} = A_o \left\{ p_{air} \left(1 - \frac{\gamma_{air} - 1}{2} \frac{v}{a_{air}} \right)^{\frac{2\gamma_{air}}{\gamma_{air} - 1}} - p_{driver} \left(\frac{L}{x} \right)^{\gamma_4} \right\} , \tag{2.40}$$

where, again, m is the mass of the piston, A_o is the area of the driver section, p_{air} is the initial air pressure pushing the piston, p_{driver} is the driver gas pressure before piston

launch, and, finally, L is the total length of the driver section. The nonlinear equation is solved using the Runge-Kutta-Nystrom method.

2.6.1 The Free Piston Shock Tunnel T5

The free piston shock tunnel T5 has a 30 m long driver section with an inside diameter of 30 cm. At diaphragm rupture this length is reduced by a factor close to 53 in both simulations due to the piston motion compressing the driver gas in front of it. The driven section is 9 cm in diameter, 12 m long, and the end-wall is terminated by a nozzle with a throat diameter of 3 cm. The area change in the driver section is located 25 cm upstream of the main diaphragm and the mass of the piston is 120 kg. The reader, who is not familiar with free piston shock tunnel, can find a more complete description of T5 in section 4.2. Table 2.1 gives the conditions of the system at diaphragm rupture for the two simulations.

	case no. 1	case no. 2
Driver Gas	85% He - 15% Ar	95% He - 5% Ar
Driver Gas Pressure (MPa)	88.0	108.0
Driver Gas Temperature (K)	4150	4150
Driver Gas Compression Ratio (λ)	53.5	53.3
Pressure Behind the Piston (MPa)	7.72	11.45
Piston Position (from area change) (m)	- 0.54	- 0.54
Piston Velocity (m/s)	155	185
Driven Gas	air	air
Driven Gas Pressure (kPa)	85.0	80.0
Driven Gas Temperature (K)	293	293

Table 2.1 Conditions of the system at diaphragm rupture for the T5 flow simulations.

Figure 2.9 shows the x-t diagram for case no. 1. The driver section is on the left side, and the dotted line at x = 0 represents the area change between the driver and driven sections. The piston motion toward the area change can be seen in the driver section. The incident and reflected shocks are represented by interrupted lines and can be seen on

the right side of the diagram. The interface between the driver and driven gases is also shown as a dotted line. All the other full lines are characteristic lines computed by the program. Some of the weaker characteristic lines have to be combined during the simulation to reduce the potentially very large number of characteristic lines generated by the program. The computation was stopped because the reflected shock had reached the area change, an interaction that has not been incorporated into the program.

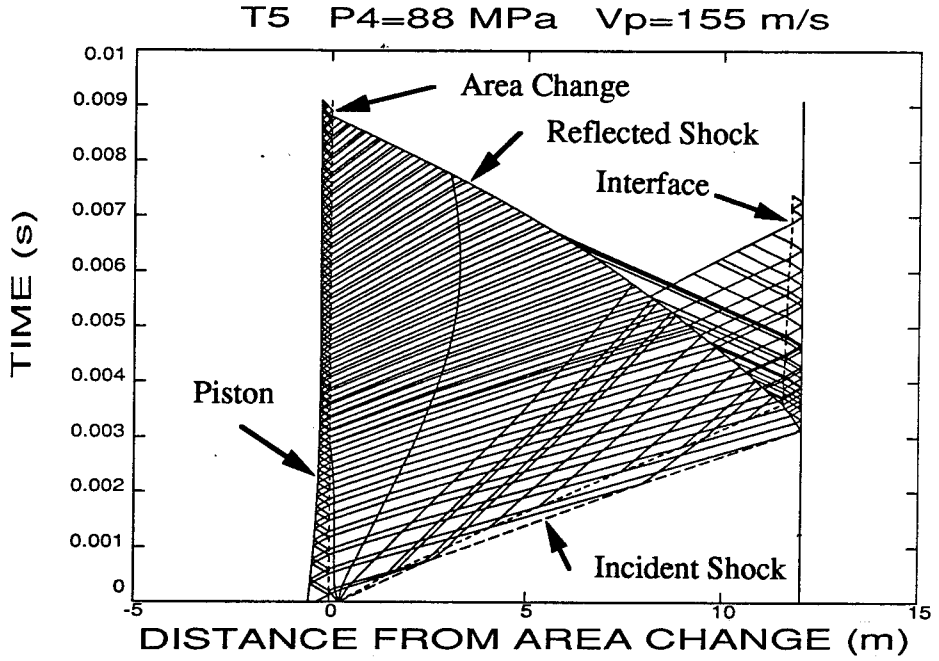

Figure 2.9 The x-t diagram from the numerical simulation of the free piston shock tunnel T5 case no. 1.

Figure 2.10 shows a comparison of the measured and calculated pressure in the driver section of T5 near the area change as a function of time, t = 0 being the moment of main diaphragm rupture. The experimental measurement shows shock waves on the compression side and a spike at about t = 3 ms due to electrical noise. The numerical solution is calculated in two parts; first, the pressure rise up to diaphragm rupture using equation 6.40 and then, the part following the rupture of the main diaphragm using the method of characteristics simulation.

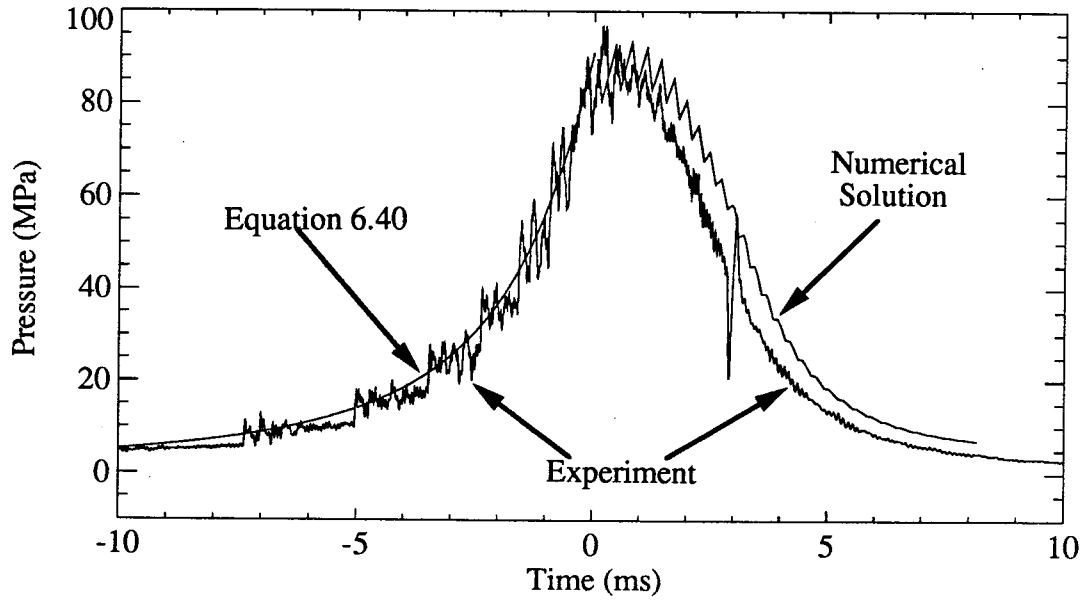

Figure 2.10 Numerical and experimental driver section pressure for the free piston shock tunnel T5 case no. 1 with piston velocity of 155 m/s at diaphragm rupture.

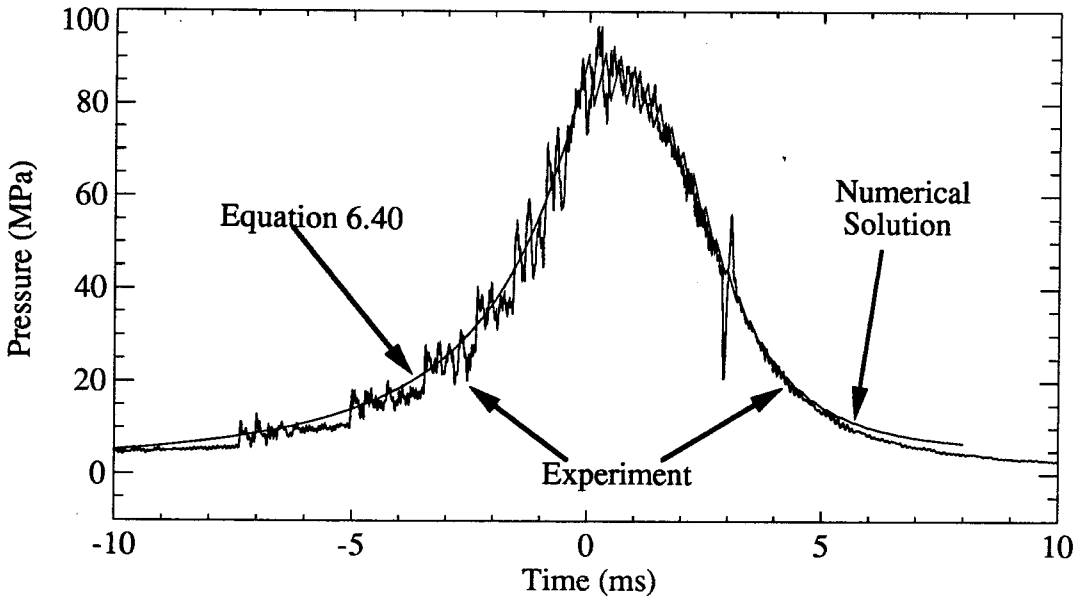

Figure 2.11 Numerical and experimental driver section pressure for the shock tunnel T5 case no. 1 with piston velocity of 132 m/s at diaphragm rupture.

The waviness of the solution is intrinsic to the characteristics method and is not a sign of any convergence problem. It is even interesting to notice that just after the diaphragm rupture the pressure measurement shows the same waviness with about the same frequency. A strong wave reverberates between the piston and the area change at the entrance of the driven section. It can easily be seen that the numerical simulation underestimates the pressure drop in the driver section.

Figure 2.11 shows almost the same simulation but this time the piston velocity at diaphragm rupture is reduced by about 15%, from 155 m/s to 132 m/s. The agreement between the two curves is now very good and seems to indicate that the piston is probably slowed down during the compression phase of its trajectory by some friction with the tube.

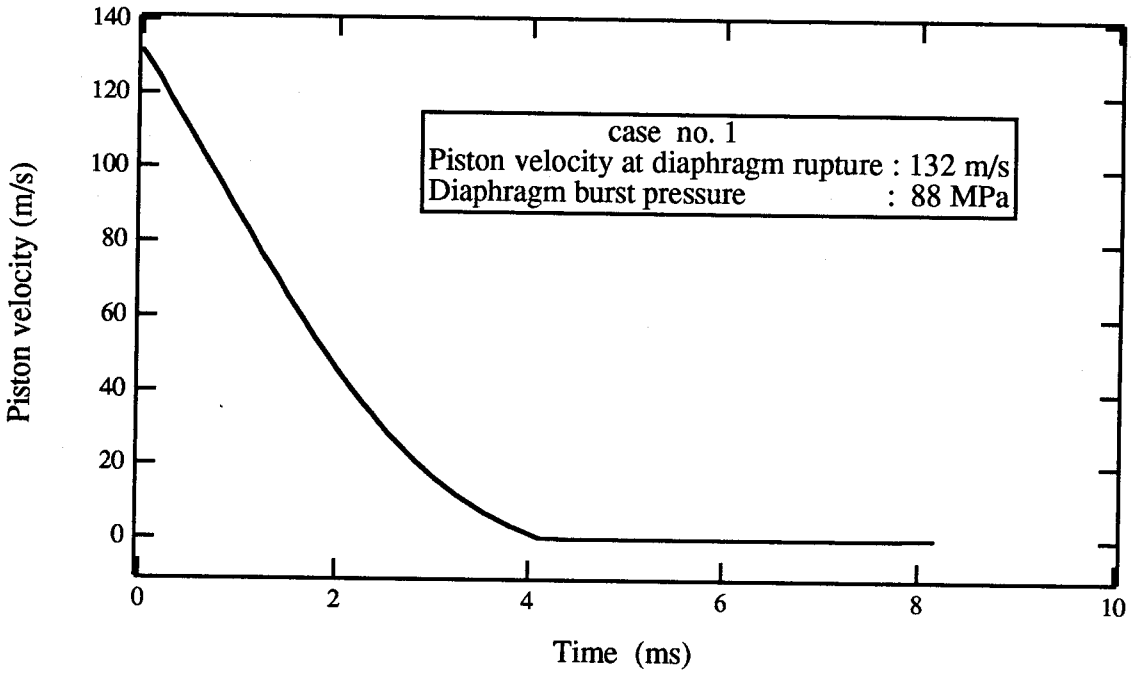

Figure 2.12 Computed piston velocity after diaphragm rupture for the free piston shock tunnel case no. 1.

Figure 2.12 and 2.13 show, respectively, the piston velocity and its position with respect to the end of the driven section for the corrected piston velocity. According to the simulation, the pressure in front of the piston is sufficient to stop it before it reaches the end, a condition that is considered safe in such a facility. The fact that the piston is still at 25 cm from the area change at the end of the simulation is not considered very dangerous

because the re-acceleration of the piston is very limited in such a short distance. Notice that the velocity of the piston in figure 2.12 is never negative, due to a braking device on the piston preventing backward motion. The numerical simulation incorporates this feature.

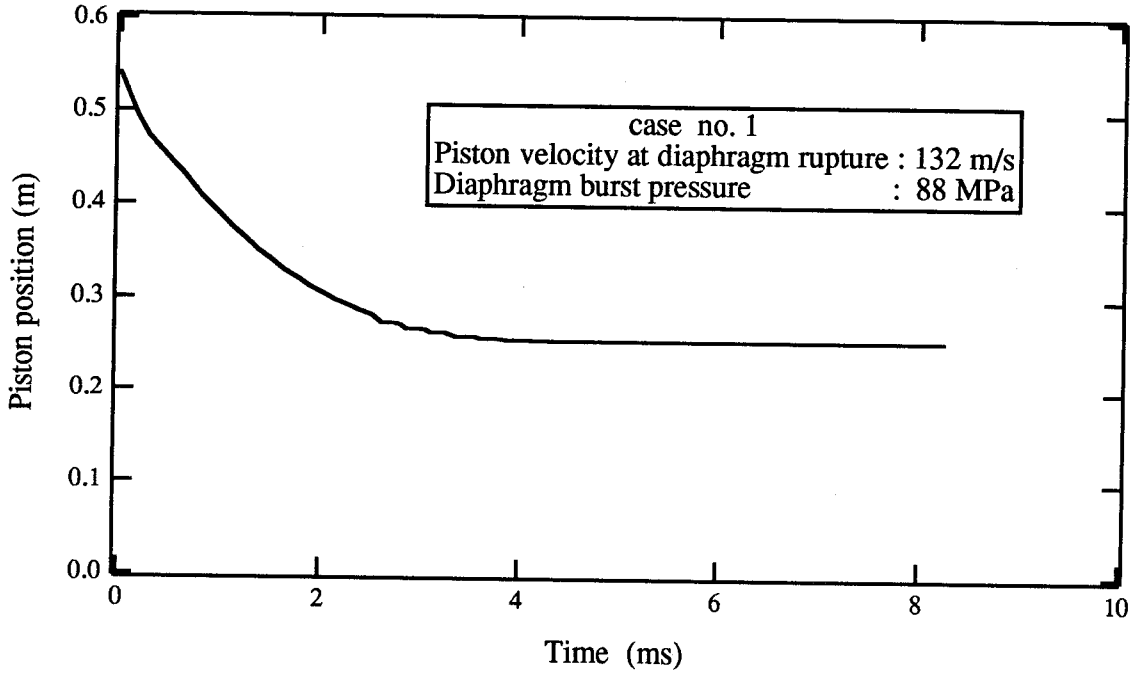

Figure 2.13 Computed piston position after diaphragm rupture relative to the area change at the end of the driver section of the free piston shock tunnel T5 case no. 1.

Figure 2.14 shows both experimental and numerical incident shock velocity in the driven section of the shock tunnel. The experimental results are determined by the shock arrival time at five different pressure transducer points along the tube. The numerical solution seems to agree well for the first part of the section. Then, the experimental result shows a net reduction in the shock speed of about 20% before reaching the end, a reduction not seen in the simulation. This 20% reduction in the shock velocity combined with a proportional reduction in the reflected shock speed explains the very large discrepancy between the experimental and the calculated nozzle reservoir pressure. According to the simulation, the pressure should reach 130 MPa but really only reaches 62.5 MPa. This factor of two in the nozzle reservoir pressure can be accounted for entirely by the 20% reduction in speed of the incident shock.

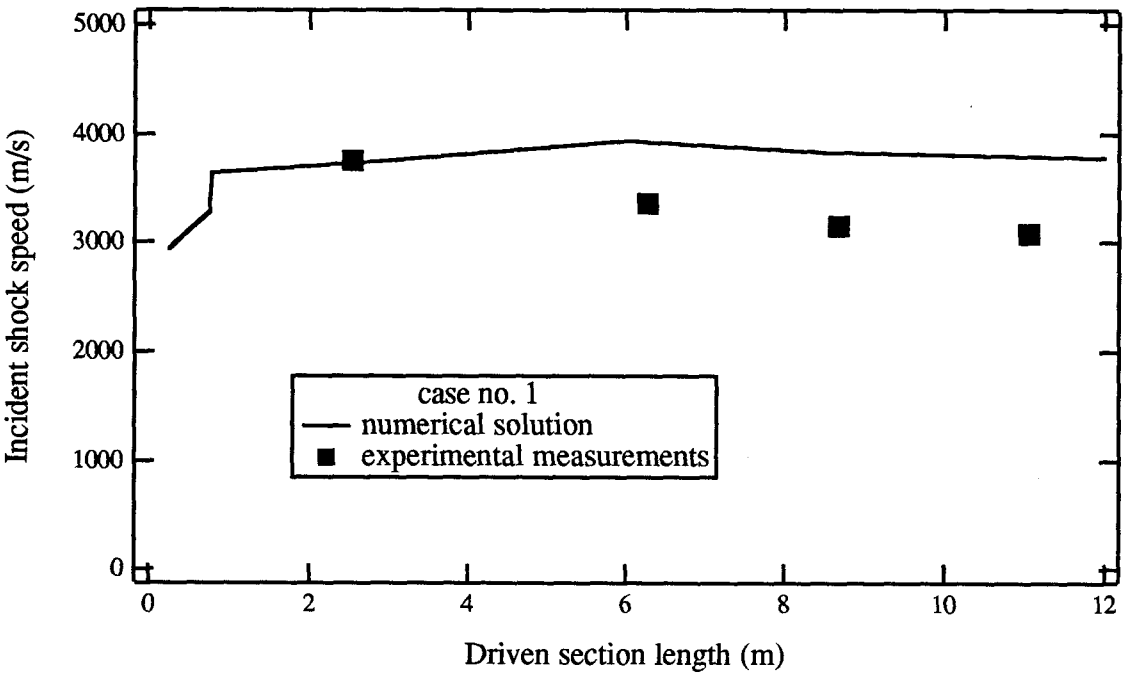

Figure 2.14 Experimental values of the incident shock speed compared to the numerical results for the T5 simulation case no. 1.

Previous speculations blamed this significant reduction in the shock speed on possible strong expansion waves coming from the rapidly dropping pressure of the driver section. The present numerical simulation for this and many other cases contradicts this explanation. Phenomenon that could cause such a drop in the shock velocity must be related to some viscous effects. It has been known for a long time (see Roshko, 1960 and Mirels, 1963) that the shock speed is reduced by the growing boundary layer on the wall of the shock tube. For a very strong shock, like in T5, this boundary layer can only explain less than 10% of the loses in speed. The other 10% or more must come from other viscous effects like flow separation at the area change between the driver and driven section.

The x-t diagram for case no. 2 is shown in figure 2.15. It is similar to the x-t diagram presented in figure 2.9 for the first case looked at. The incident and reflected shocks are represented by interrupted lines and can be seen on the right side of the diagram. The interface between the driver and driven gases is also shown as a dotted line. All the other full lines are characteristic lines computed by the program. The computation was

stopped because the reflected shock had reached the area change, an interaction that has not been incorporated into the program.

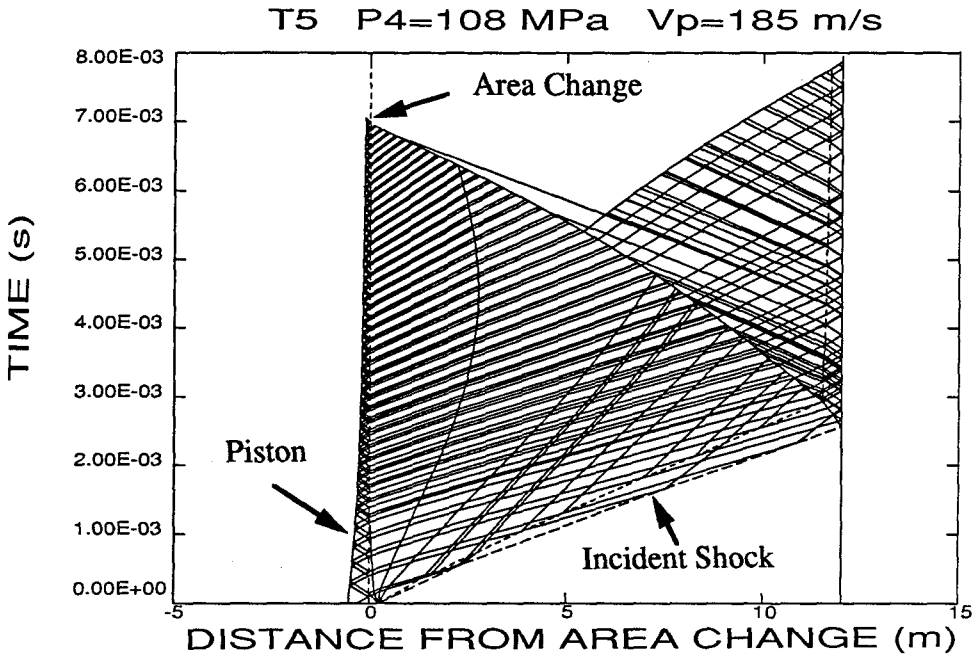

Figure 2.15 The x-t diagram from the numerical simulation of the free piston shock tunnel T5 case no. 2.

The pressure in the driver section of T5 is shown in figure 2.16. Even with a higher piston velocity at diaphragm rupture compared to the first case, the pressure here drops faster, because the burst pressure is higher, making the flow rate through the driver section proportionally higher, and thus reducing the pressure in the driver section at a faster rate. The higher burst pressure also increases the deceleration of the piston, making it less efficient at sustaining the pressure in the driver section.

Once again the piston velocity seems to be over estimated in this case. To get a good agreement with the experiment, as in the first case, the piston velocity needs to be reduced by 14% at diaphragm rupture, to 160 m/s. The result is shown in figure 2.17. Other simulations not presented here for burst pressure as low as 57.5 MPa also indicate an overestimate of the piston velocity by about 15%, most likely caused by friction losses in the piston motion.

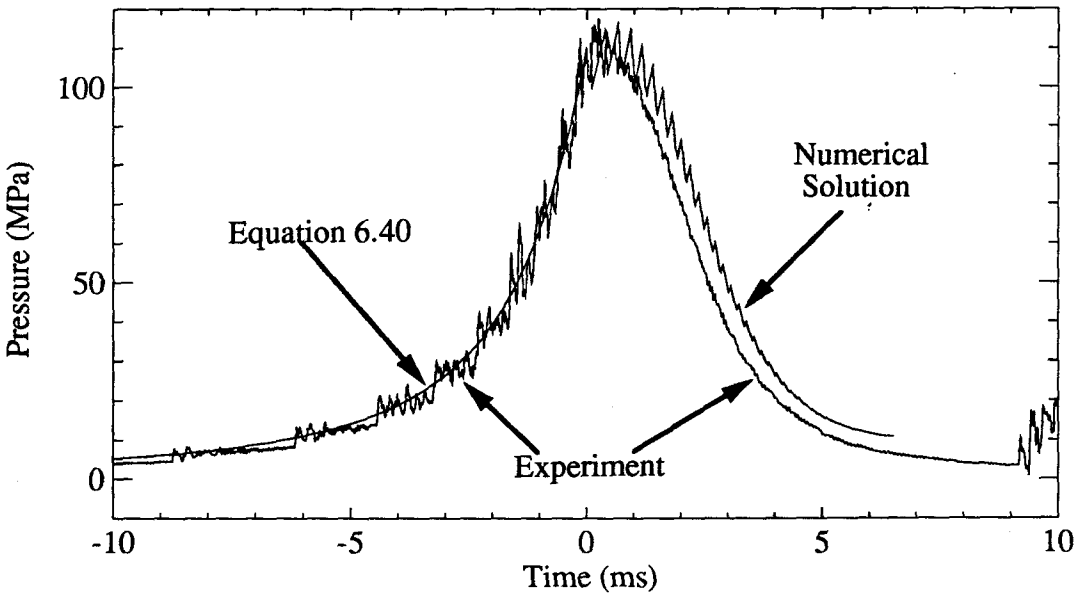

Figure 2.16 Numerical and experimental driver section pressure for the free piston shock tunnel T5 case no. 2 with piston velocity of 185 m/s at diaphragm rupture.

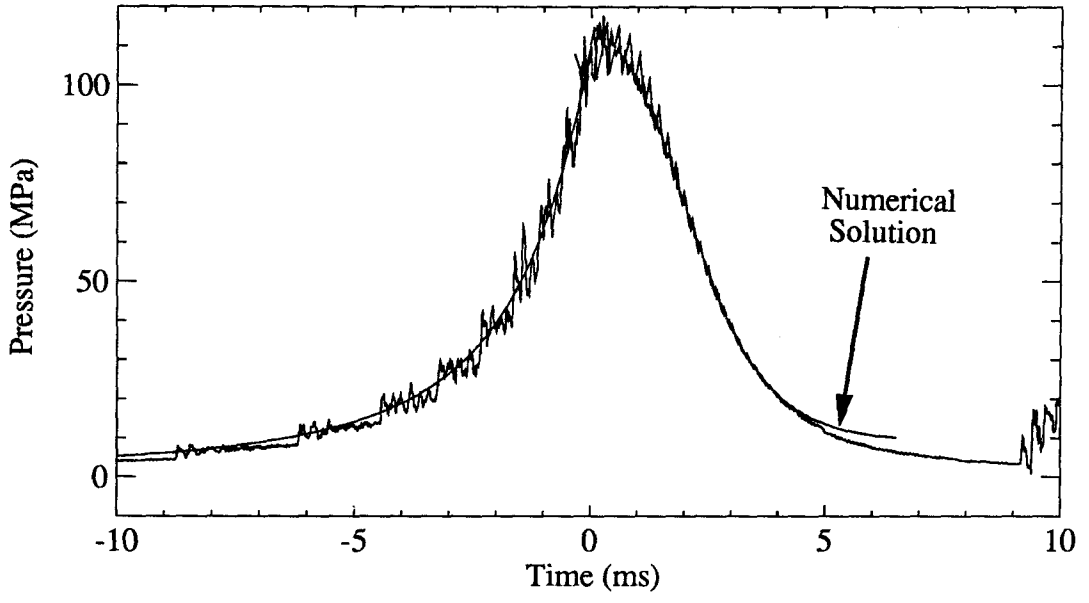

Figure 2.17 Numerical and experimental driver section pressure for the free piston shock tunnel T5 case no. 2 with piston velocity of 160 m/s at diaphragm rupture.

Figures 2.18 and 2.19 show the piston velocity and the piston position, respectively, for this second case. One major difference, compared with the previous case, is that the piston never stops and is heading toward the area change with a velocity close to 25 m/s at the end of the simulation. The facility would probably be damaged if the piston were to hit the end at that velocity.

By extrapolating to the time of impact on figure 2.19, the piston would hit the end nearly 10 ms after diaphragm rupture. Going back to figure 2.17, the experimental reflected shock comes back into the driver section after only 9 ms. Therefore, even if the piston is going too fast, it will eventually be stopped very close to the end by the pressure build-up created by the returning reflected shock. This over-driving of the piston can only be done for the higher range of enthalpies where the incident and reflected shocks are fast enough to catch the piston before impact. The minimum enthalpy at which this approach can be used is about 16 MJ/kg.

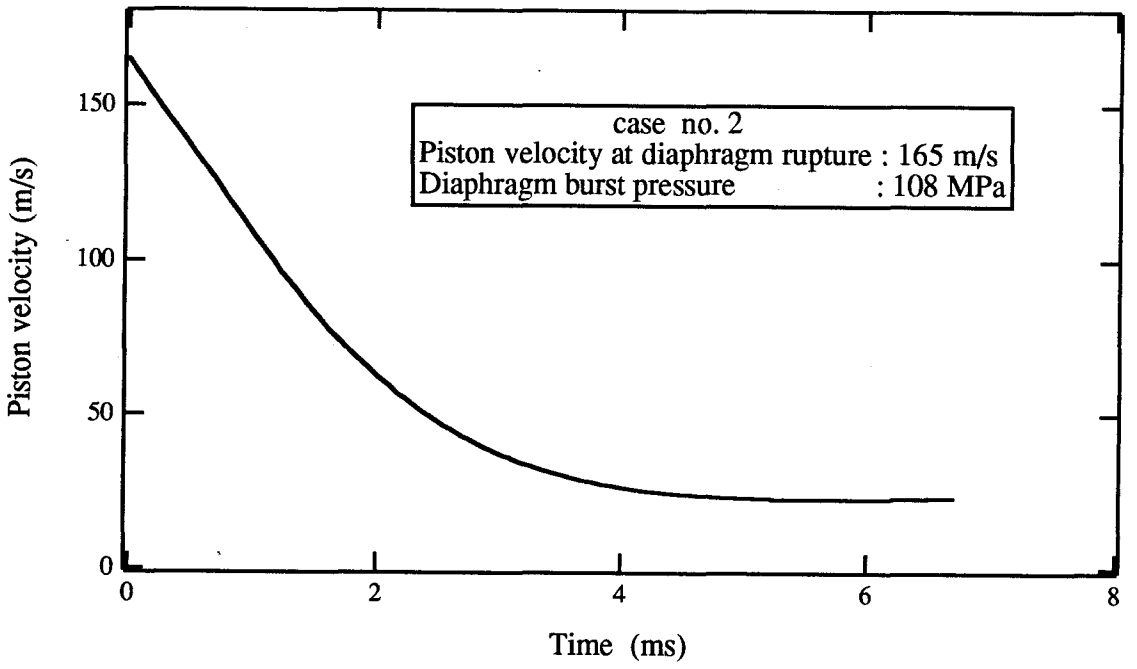

Figure 2.18 Computed piston velocity after diaphragm rupture for the free piston shock tunnel T5 case no. 2.

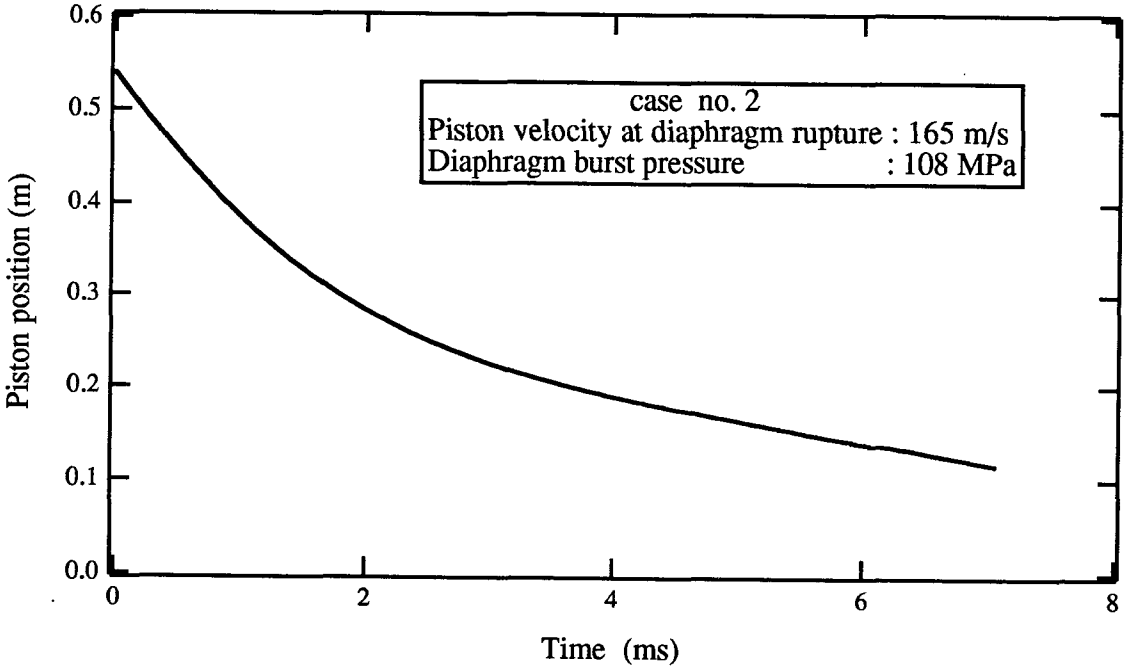

Figure 2.19 Computed piston position after diaphragm rupture relative to the area change at the end of the driver section of the shock tunnel T5 case no. 2.

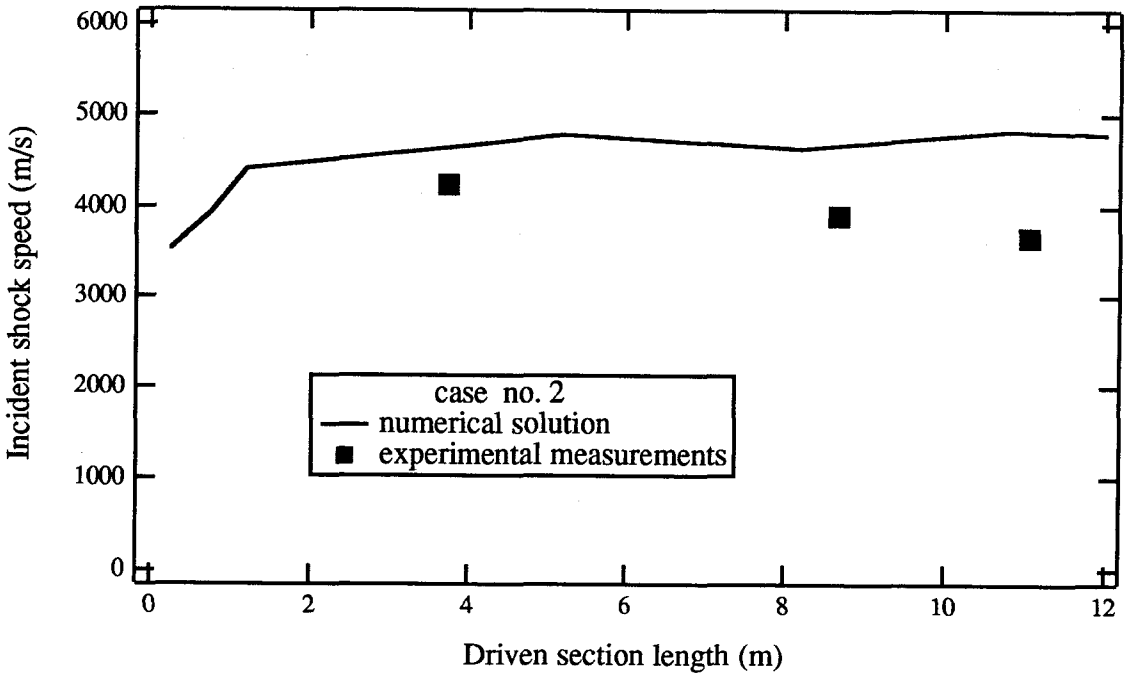

Figure 2.20 Experimental values of the incident shock speed compared to the numerical results for the T5 simulation case no. 2.

The experimental and numerical shock velocities for this case are presented in figure 2.20. Once again the shock speed is overestimated by about 20%, making the estimated nozzle reservoir pressure twice as large as the actual one.

2.6.2 The Combustion Driven Shock Tunnel

The combustion driven shock tunnel has a driver section 1.47 m long, 5 cm in diameter, and a driven section 1.95 m long, 2.5 cm in diameter. The nozzle at the end of the driven section has a diameter of 5 mm. At diaphragm rupture, the driver gas, which is a mixture of mainly helium and water, is at about 2000 K and at a pressure of 5.53 MPa. The hydrogen in the driven section is at 293 K with an initial pressure of 379 kPa. These data are presented here only to give the reader a feeling for the facility, a detailed description of the system is presented in chapter 3.

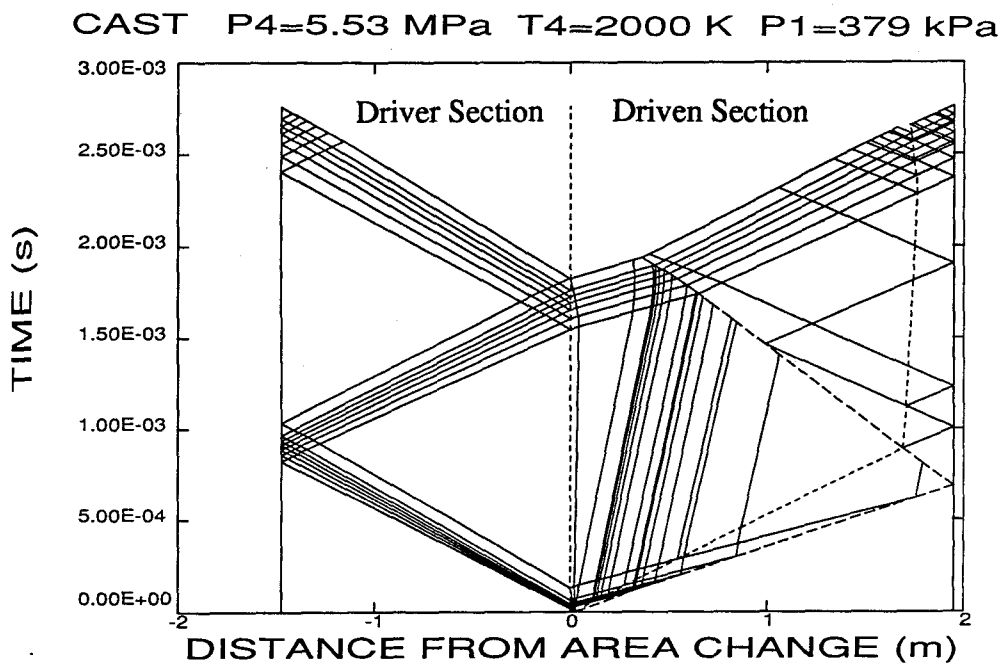

Figure 2.21 The x-t diagram from the numerical simulation of the combustion driven shock tunnel.

The x-t diagram of the simulation is presented in figure 2.21. The driver section is on the left side, and the dotted line at x = 0 represents the area change between the driver and driven sections. The incident and reflected shocks are represented by interrupted lines

and can be seen on the right side of the diagram. The interface between the driver and driven gases is also shown as a dotted line. All the other full lines are characteristic lines computed by the program.

In this example, the "steady state" condition of the nozzle reservoir at the end of the driven section starts about 1 ms after main diaphragm rupture, just after reflection off the end-wall of the wave coming from the interaction of the reflected shock and the interface. The end of the "steady state" condition occurs when the expansion fan coming from the driver section reaches the nozzle reservoir, about 2.4 ms. A test time of about 1.4 ms is predicted by the numerical simulation. Flow through the driven section end-wall was computed in this simulation; it is shown by the interface slowly closing in the end-wall during the test time.

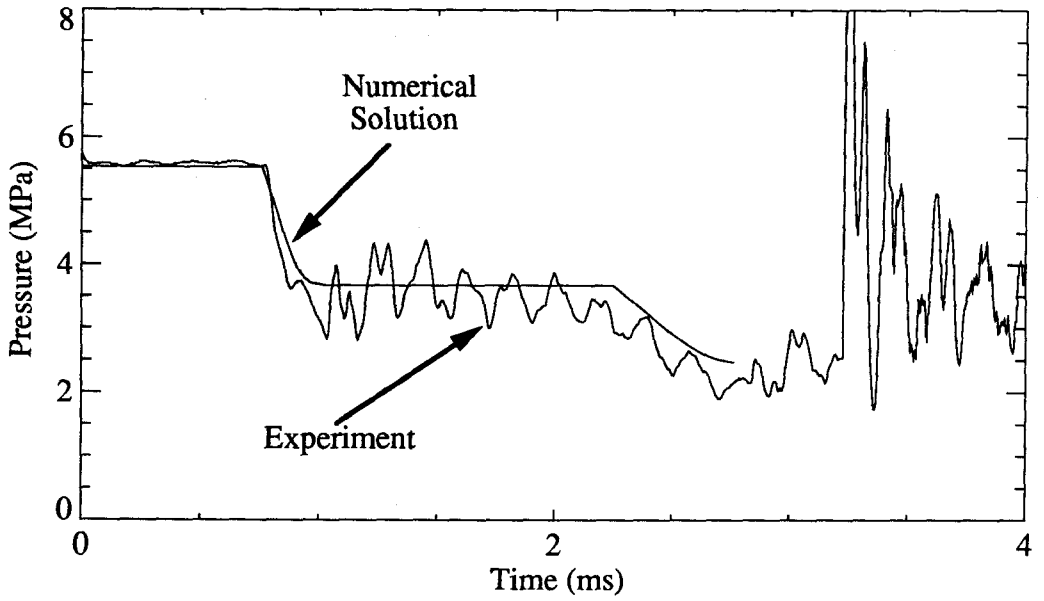

Figure 2.22 Comparison of measured and calculated pressure at the end of the driver section of the combustion driven shock tunnel.

Figure 2.22 shows the numerical and experimental driver section end-wall pressure. The two curves agree very well except for the waviness of the experimental measurement after the arrival of the first expansion fan. These waves are believed to be

created by a pipe resonance, the transducer being connected to the end wall of the driver section by a small orifice (the "pipe") almost 5 cm long.

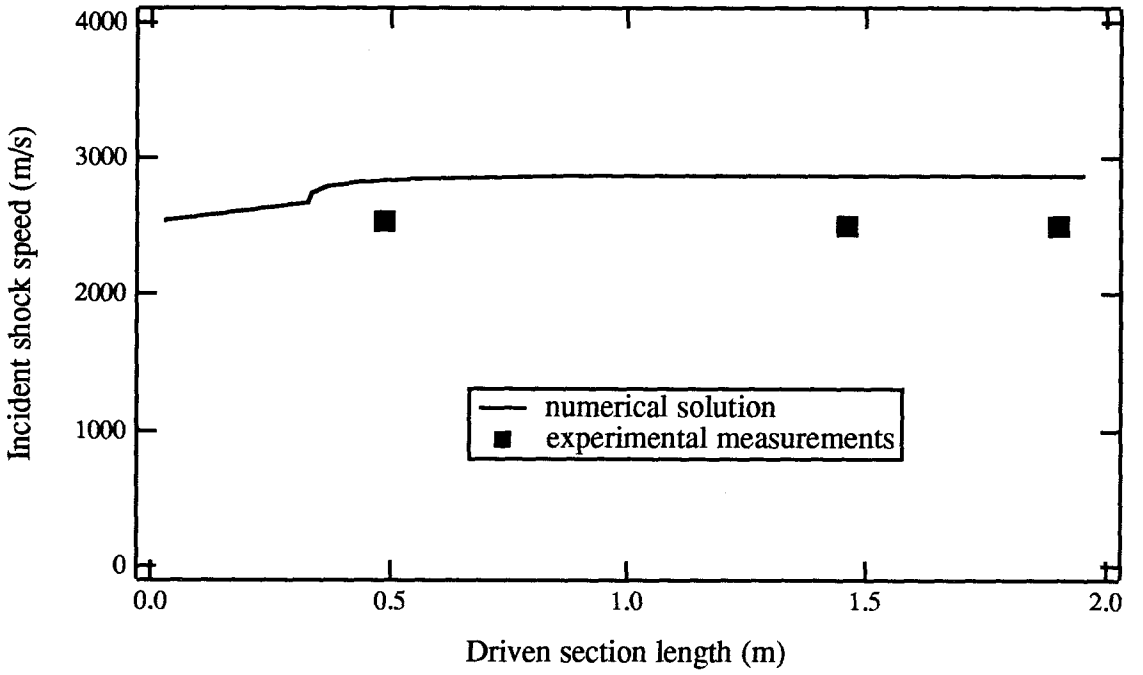

Figure 2.23 Experimental values of the incident shock speed compared to the numerical simulation for the combustion driven shock tunnel.

The incident shock speed is shown in figure 2.23. The viscous losses here are less important than in the case of T5; only 10% of the shock speed is lost in this case. One of the main reasons for this better result is that the ratio Length/Diameter for the driven section of T5 is almost 130 compared to an L/D for the combustion driven shock tunnel of 77, making the viscous boundary layer effect much less severe in the case presented here.

Finally, figure 2.24 shows the pressure at the end of the driven section for the numerical simulation and the experiment. The overestimate from the numerical simulation is, once again, due to a 10% higher shock speed compared with the experiment. The two traces give the same arrival time of the expansion fan. The 0.8 ms it takes in the experiment for the pressure to reach its "steady state" condition is believed to be caused by a space of about 5 cm between the mylar diaphragm closing the driven section and the actual nozzle

position at the end of the driven section. This part of the section is under vacuum before the test and must be filled once the incident shock breaks the mylar diaphragm.

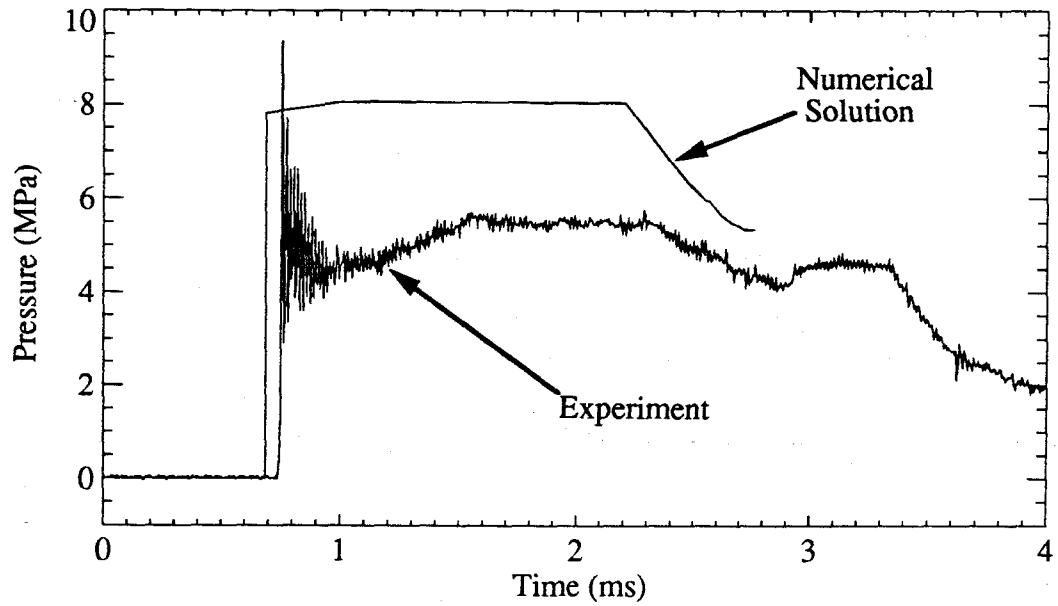

Figure 2.24 Comparison of measured and calculated pressure at the end of the driven section of the combustion driven shock tunnel.

2.7 Conclusion

The numerical code helped explain the piston motion of the free piston shock tunnel T5 and gave an estimate of the friction losses in that part of the system. The code has also indicated that the drop in the shock speed is not due to the rate of pressure drop in the driver section of T5 but to very significant viscous effects in the driven section. Efforts to incorporate these viscous losses due to the boundary layer in the simulation were not very successful and are not presented here.

The numerical code was also a very useful tool in the design of the combustion driven shock tunnel. With some restriction regarding the space available, an optimization of the test time was made with the code by changing the relative length and diameter of the sections. Estimations of the maximum temperature achievable were also performed using

conservative values of the simulations. With a significant contribution from the code, the combustion driven shock tunnel presented in the next chapter turned out to be as good as expected.

Chapter 3
Combustion Driven Shock Tunnel

3.1 Introduction

In chapter 1, the arguments leading to the decision to build a combustion driven shock tunnel to supply hot hydrogen for the combustion experiments in T5 were presented. Once this decision was made, a few major problems still needed to be solved. One problem was the need to synchronize the combustion driven shock tunnel with T5. Both tunnels have a test time of approximately 1 ms. In order to use the full test time of T5, the timing of the combustion driven shock tunnel must be precise to about 0.1 to 0.2 ms. The signal to break the main diaphragm also needed to precede the actual test time by no more than 4 ms, because the only reliable signal coming from T5 before the test is from the pressure transducers in the driven section detecting the incident shock which is generated less than 4 ms before the flow in T5 is established.

The simplest way of synchronizing the two tubes is to ignite the driver gas at a precise time interval before the T5 flow. By making sure that the diaphragm is not strong enough to resist complete combustion, synchronization can be achieved. This approach, however, could not be used for two reasons: 1) the flame speed is too slow to complete the combustion in the 4 ms available, and most important, 2) past experience with combustion driven shock tunnels shows that repeatability of the combustion time is not very good, making it impossible to be precise to 0.2 ms. To solve this synchronization problem, a strong diaphragm able to resist the pressure of the full combustion and a different device to break the diaphragm at the chosen time were used. Thus the combustion could be triggered some time before the test with an uncertainty of about 5 ms, something that is easy to do during the compression phase of the driver gas in T5. A chart of the sequence of events for

T5 and the combustion driven shock tunnel is presented in figure 3.1. The settling time for T5 is mostly the time it takes to start the nozzle. In the case of the combustion driven shock tunnel, the settling time is related to the time the system takes to reach constant reservoir pressure at the end of the driven section after incident shock reflection.

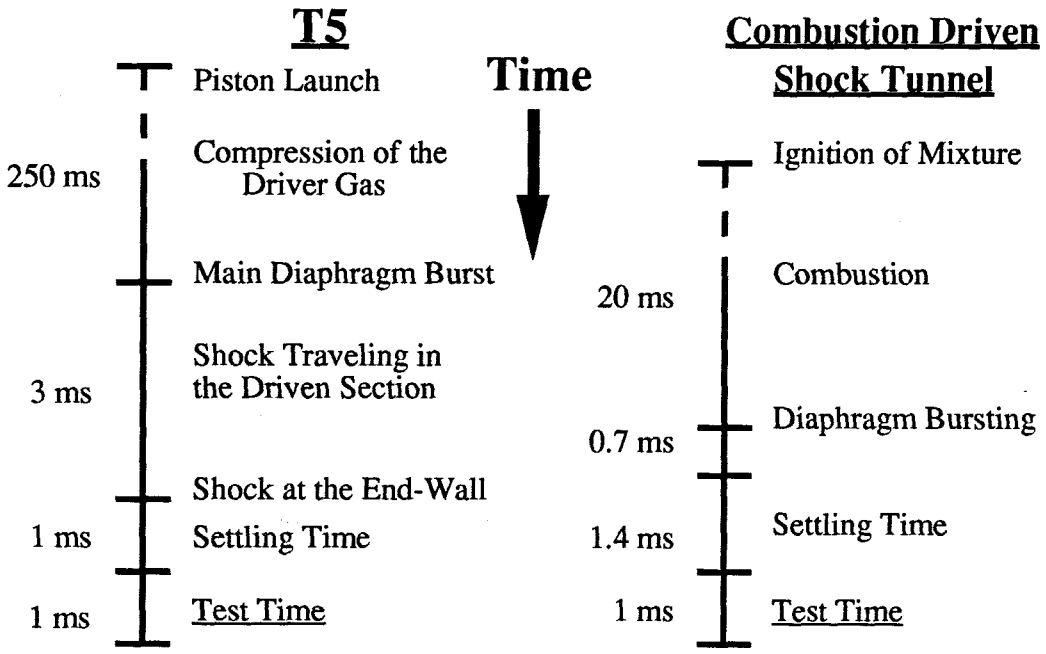

Figure 3.1 Chart of the sequence of events for T5 and the combustion driven shock tunnel.

One possibility to satisfy the timing requirements is to use a double diaphragm technique. In this method, the small space between two diaphragms is filled to an intermediate pressure. A fast acting valve releases the gas in the space to cause rupture of the upstream diaphragm and consequently of the second one at a predetermined time. Four years ago, this approach seemed risky because the best fast acting valves had an opening time of around 4 to 6 ms. However, this problem can be effectively solved by the use of a much higher voltage than recommended on the solenoid valve for only a few milliseconds, and by a very tight tolerance on the strength of the diaphragms.

It is also possible to make a combustible mixture of gas which could easily burn in the 4 ms available in the space between the two diaphragms. The sequential breaking of the diaphragms would then be started by the downstream diaphragm. Neither system using this double diaphragm approach was chosen because both imply a rather complex junction between the driver and driven section.

The chosen system requires only a single diaphragm. It uses a new technique for breaking the diaphragm at a precisely determined time. The system uses a probe mounted inside the driver section in contact with the diaphragm, but electrically insulated from the rest of the tube. The probe is then used to deliver a large electrical current to the diaphragm, effectively melting it at the point of contact. This local weakening of the diaphragm is rapidly followed by its complete failure. Tests showed repeatability to within 50 μs, making the system almost ten times better than the original requirement.

A detailed description of the diaphragm bursting system is presented in section 3.5, but first, section 3.2 presents a review of the work done in the area of combustion driven shock tunnels. It is followed in section 3.3 by a description of the driver part of the present system. Section 3.4 discusses some unique aspects of the driven section of the facility. The system overall efficiency is presented in section 3.6, and finally, section 3.7 presents a short conclusion.

3.2 Research Review

The combustion driven shock tunnels have been a very successful tool for research in high enthalpy flows, being able to bring air, as a driven gas, to about 6500 K. General Electric Research Laboratory built a very large facility (see Nagamatsu et al., 1961) with a driven section of more than 31 m and an inside diameter of 10 cm, but the system is not in use anymore. Boeing has also had their facility for some time (see Boeing, 1990). This is a smaller system, but in all, a very good machine.

In recent years, NASA-Ames converted a facility originally built to provide a conterflow to a ballistic range into a large combustion driven shock tunnel. The driver section is 43 cm in diameter, 21 m long and is made from two 16 inch naval cannons, and therefore its name: NASA-Ames Research Center 16-Inch Shock Tunnel. Recent results from the new facility have been presented by Loomis et al. (1992).

Other much smaller facilities are also being used in universities and research centers as a means to get high enthalpy gas for educational purposes or for diagnostics development. But, what makes the present facility unique, is that it is not primarily used to get high enthalpy flows, but rather to increase significantly the enthalpy of hydrogen as the driven gas.

3.3 Driver Section

The driver section of the combustion driven shock tunnel has an inside diameter of 5 cm for a length of 1.5 m. To insure its strength and to minimize corrosion, the tube is made of stainless steel with a wall thickness of 1.9 cm. Figure 3.2 shows the end-wall of the tube (1), which is used as the filling point for the section. Because of the need to mix the gases well, the filling line enters the section off center at an angle of about 30 degrees to the axis of the tube. This angle creates a swirling motion as the gas enters the driver section. The end wall is also used as a pressure measurement point. A second pressure transducer is mounted on the side wall of the tube 5 cm upstream of the main diaphragm.

With the stress concentrations caused by the holes and the sudden loading during combustion, the tube can withstand pressures up to 35 MPa. Thus, the filling line was designed to resist pressures up to 40 MPa because of the slight possibility of premature combustion of the mixture during the filling process. To make sure that the system would be as safe as possible, a maximum pressure after combustion of 25 MPa has been set. The tube has already been operated successfully at up to 20 MPa.

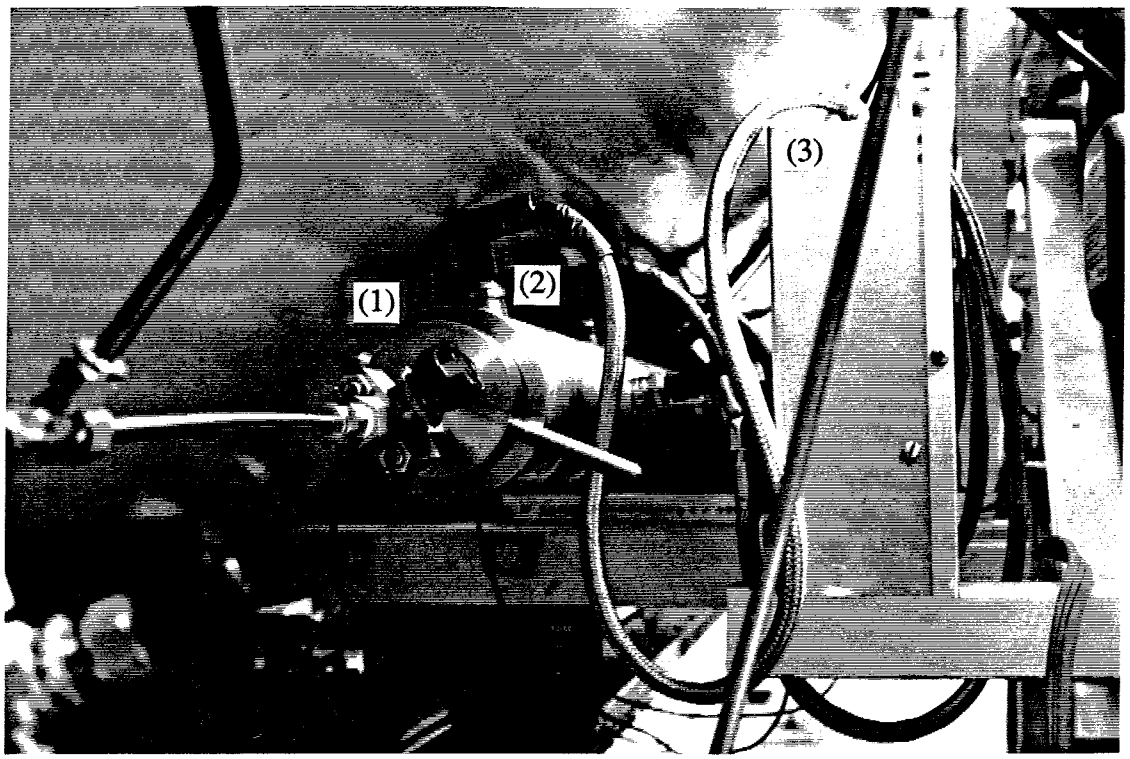

Figure 3.2 Driver section end-wall with filling line and automotive-type spark plugs.

The mixture is ignited by twelve regular automotive-type spark plugs uniformly distributed along the length of the tube. Figure 3.2 shows clearly one of the spark plugs (2) and its electrical system (3). This configuration minimizes the possibility of a detonation wave and also reduces the overall time of combustion, which lessens the heat lost to the wall of the tube before the test. The spark plugs are arranged in a two-row configuration with an angle of 90 degree between the two rows.

Each spark plug has its own automotive-type 20 kV capacitor and its own electrical circuit. To fire the system, the trigger signal is simultaneously sent to the twelve independent circuits. To get better sparks for filling pressures over 2 MPa, the gaps between the electrodes of the spark plugs were reduced from 2 mm to 1 mm.

Gas mixtures commonly used are 14% hydrogen, 7% oxygen and 79% helium, and 16% - 8% - 76%, respectively, by volume. Figure 3.3 shows the pressure recorded by the transducer at the end-wall which is 11 cm away from the closest spark plug for a 14%

hydrogen case with filling pressure of 1 MPa. The maximum pressure occurs about 18 ms after firing.

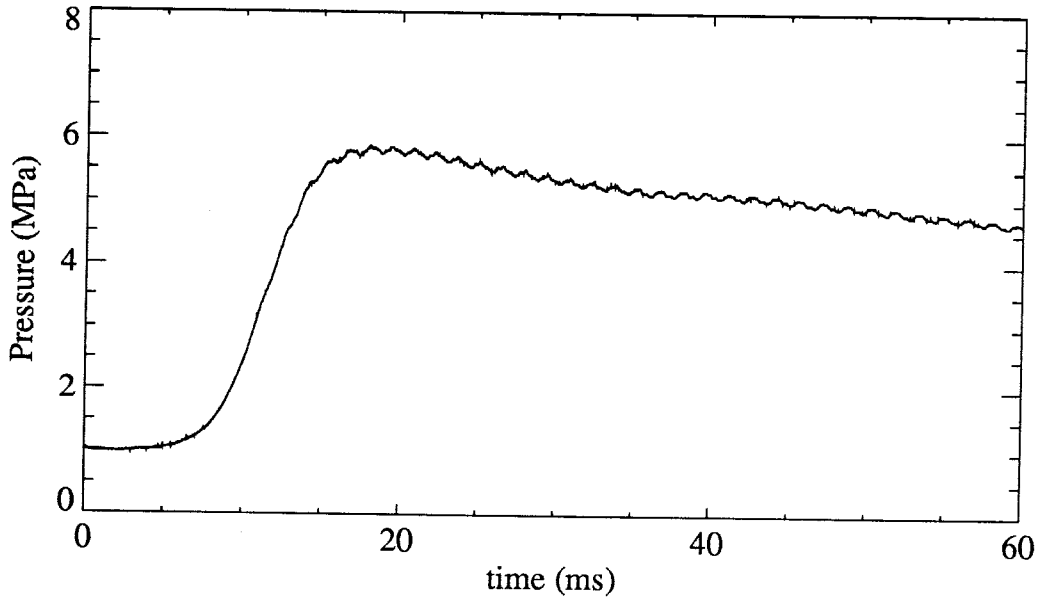

Figure 3.3 Combustion of a 14% H_2- 7% O_2- 79% He mixture at 1 MPa versus time. Pressure transducer 11 cm away from closest spark plug.

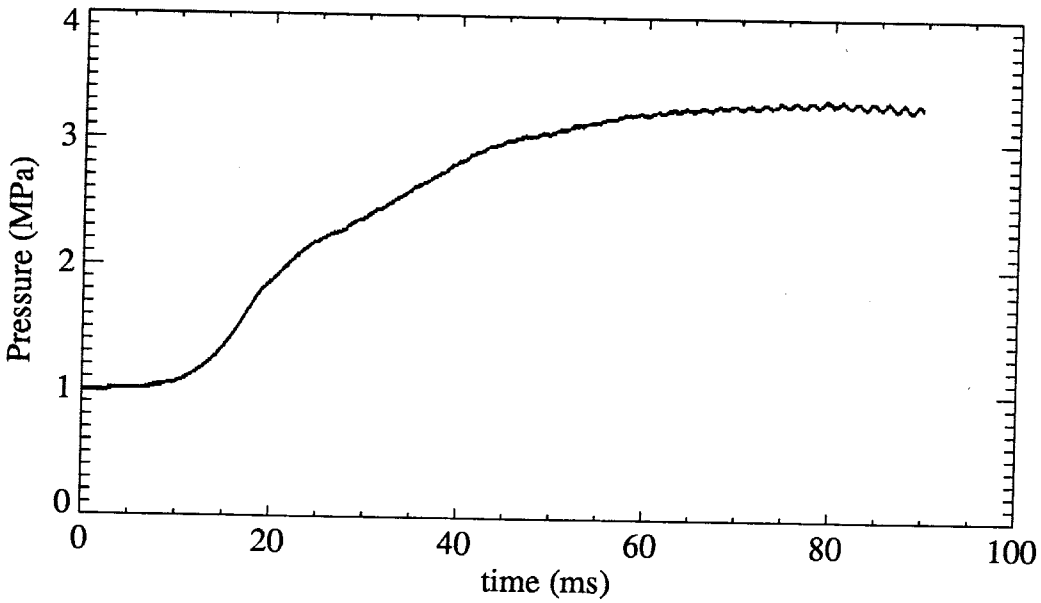

Figure 3.4 Combustion of a 12% H_2- 6% O_2- 82% He mixture at 1 MPa versus time.

Lower concentrations of hydrogen were tried, but the slow combustion and low speed of sound of the resulting driver gas made such a concentration unsuitable for the "hot" hydrogen injection experiments. To show this, the pressure trace for a 12% hydrogen combustion test is presented in Figure 3.4. In this case, the maximum pressure is reached after about 80 ms.

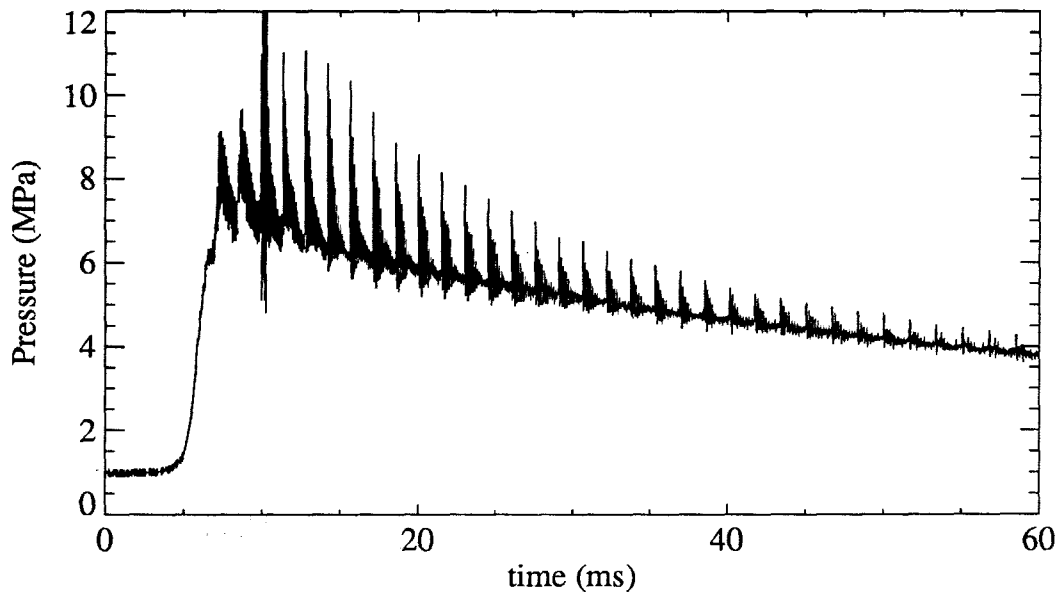

Figure 3.5 Combustion of a 18% H_2 - 9% O_2 - 73% He mixture at 1 MPa versus time.

Higher concentrations of fuel were also tested, but as predicted by chemical equilibrium calculations, a higher speed of sound than the one with 16% hydrogen was not obtained. The major problems encountered with the higher concentration of fuel were that strong waves occurred in the tube after combustion and the high temperature reached in the tube caused damage to the diaphragm rupture device. Figure 3.5 shows a pressure trace for a 18% hydrogen case. The strong waves are believed to be generated by small perturbations capable of mixing and burning the remaining fuel. Thus, only the lower hydrogen concentrations of 14% and 16% were used on a regular basis.

Having two pressure transducers in this section insures a reliable pressure measurement and also allows one to determine the speed of sound of the mixture. This is done by tracking the first expansion wave as it moves down the driver section after the

diaphragm rupture. By extrapolation, it is also possible to determine the time of the main diaphragm rupture.

Combustion tests, in which the main diaphragm is not broken, are regularly done to test the system. In these cases, there was no expansion wave in the driver and the previous method to measure the speed of sound could not be used. An alternative method was then used. It was noticed that a regular wave pattern always developed inside the tube after combustion. The speed of sound of the mixture can be determined easily by measuring the frequency of the waves and by assuming that the wave is a standing wave along the axis of the tube. Figure 3.6 shows a closer look at the pressure trace of figure 3.3 where the wave pattern can be seen clearly. Cases where both methods could be used show agreement within 2%. Tests using nitrogen instead of helium were also done to make sure that the frequency, close to 700 Hz, representing a speed of about 2000 m/s, was not caused by a natural frequency of the tube itself or by a wrong assumption for the standing wave. The wave is probably produced by some nonuniformity in the combustion process.

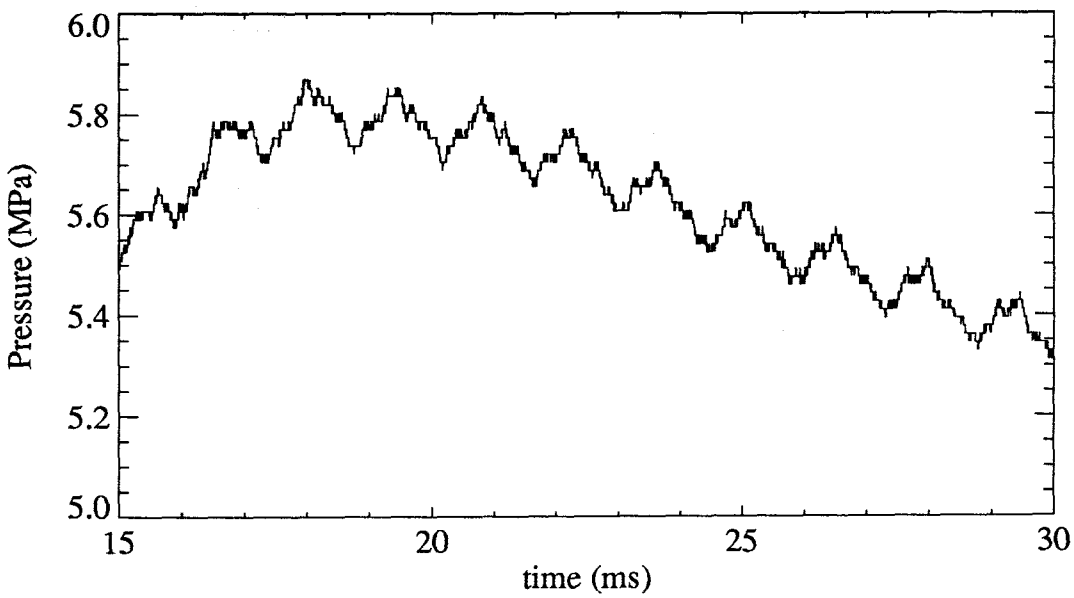

Figure 3.6 End of combustion pressure trace of a 14% H_2- 7% O_2- 79% He mixture filled at 1 MPa versus time.

Figure 3.7 shows the efficiency of the combustion for different hydrogen concentrations. Also presented in this figure are values from the chemical equilibrium code STANJAN (1987) and experimental results from Nagamatsu et al. (1961). The filling pressure in all cases is 1 MPa and, in this work, the mixture is left in the tube to settle for 30 minutes before combustion. The better combustion efficiency from Nagamatsu et al. is believed to originate from the relatively smaller heat transfer problem to the wall during combustion, because their inside diameter is three times bigger. A better efficiency in the experiment of Nagamatsu may also be due to a more complex filling system resulting in a better mixing of the gases.

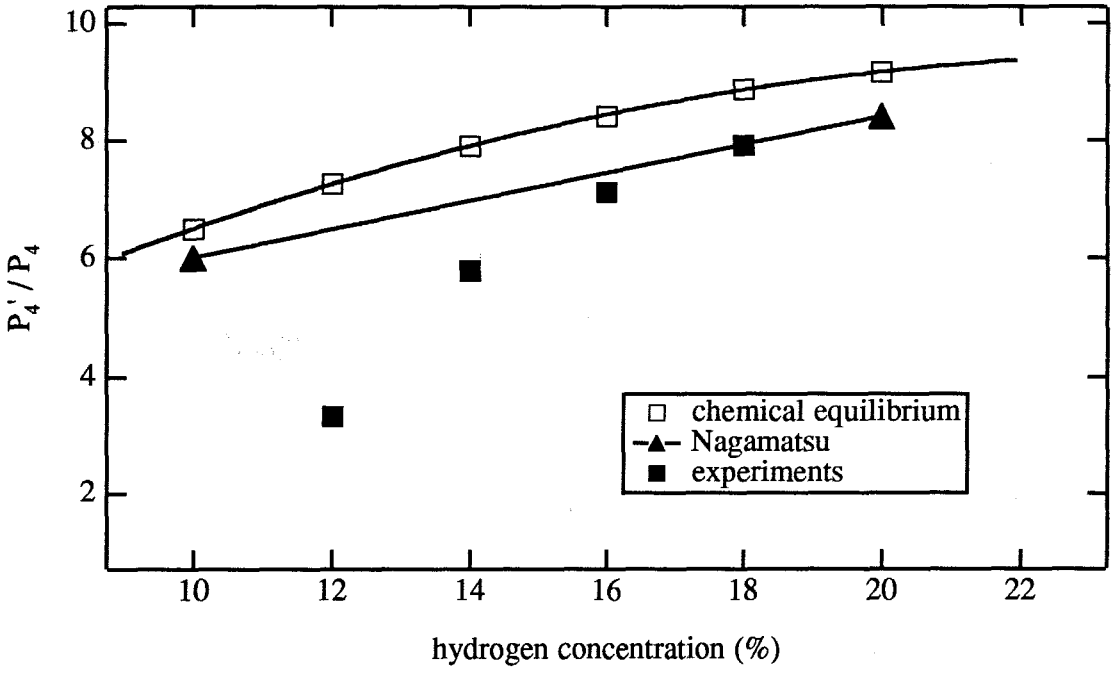

Figure 3.7 Efficiency of combustion compared to theoretical predictions and other experimental results versus hydrogen concentration. The filling pressure is 1 MPa in all cases.

Plots of the combustion efficiency for many experiments with 16% hydrogen, 8% oxygen, and 76% helium versus the time for which the mixture was left alone to settle after the filling are presented in figure 3.8. These plots seem to suggest that the settling time should always be over 30 minutes to reduce the possibility of a reduced combustion efficiency. The same behavior of the tube was found for the 14% hydrogen case.

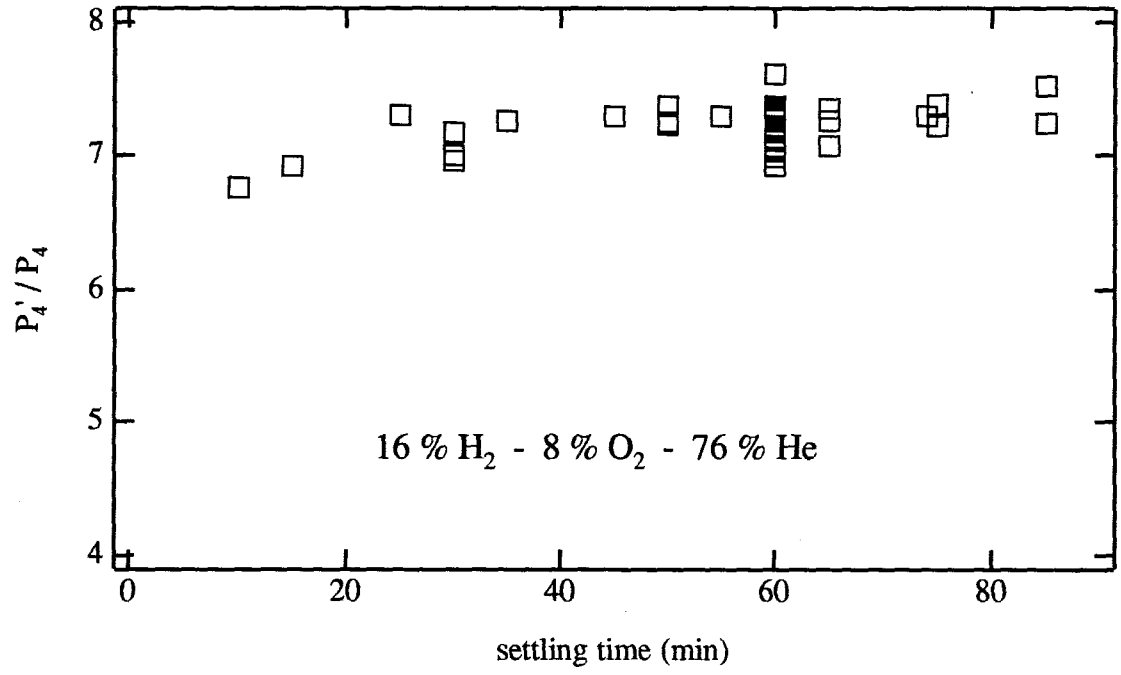

Figure 3.8 Combustion pressure ratio versus the time the mixture is left alone to settle after the filling for the 16% hydrogen case.

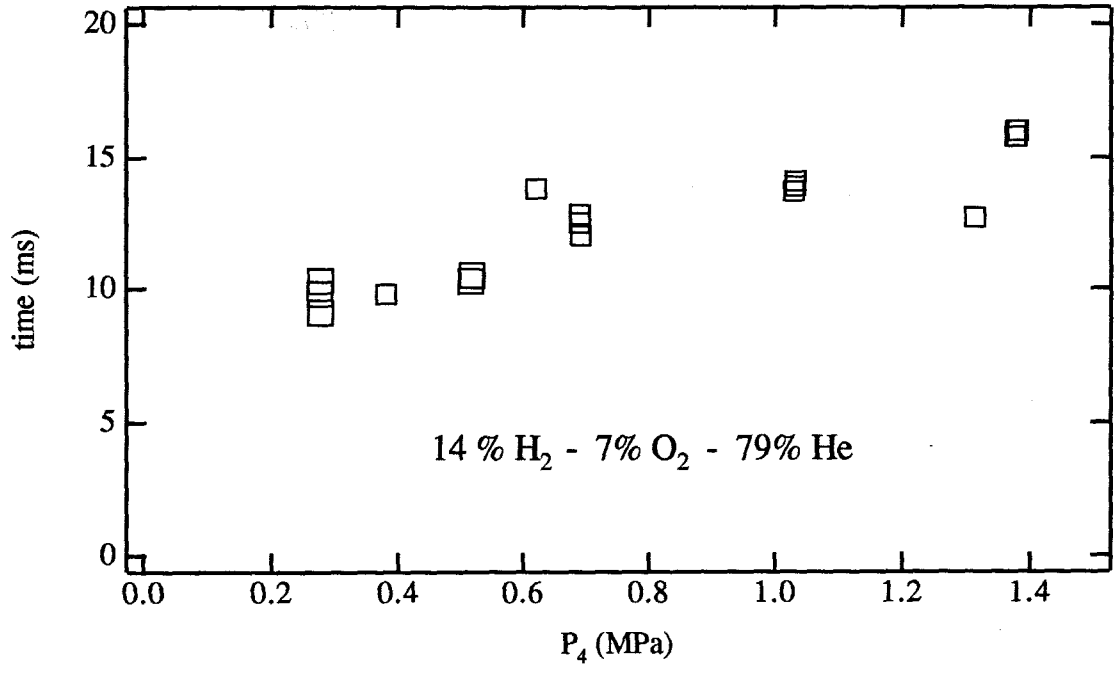

Figure 3.9 Time to reach maximum pressure versus the filling pressure for the 14% hydrogen case.

Chemical equilibrium calculation predicts a combustion pressure ratio of 7.9 for the 16% hydrogen mixture. From the slope of the pressure drop after the end of the combustion, the heat loss can be computed accurately. Without that heat loss, the pressure ratio would reach 7.5, making the combustion efficiency close to 95%.

The time it takes to reach the maximum pressure from the firing of the spark plugs is presented in Figure 3.9 as a function of the filling pressure for 14% hydrogen. A linear increase of combustion time with pressure can be seen, which agrees with Nagamatsu's results. All these experiments were done with a 1 mm gap for the spark plugs, a gap that is different from the one used for the combustion test presented in Figure 3.3. The difference is not in the real combustion time but rather in the time the spark plugs take to discharge.

3.4 Driven Section

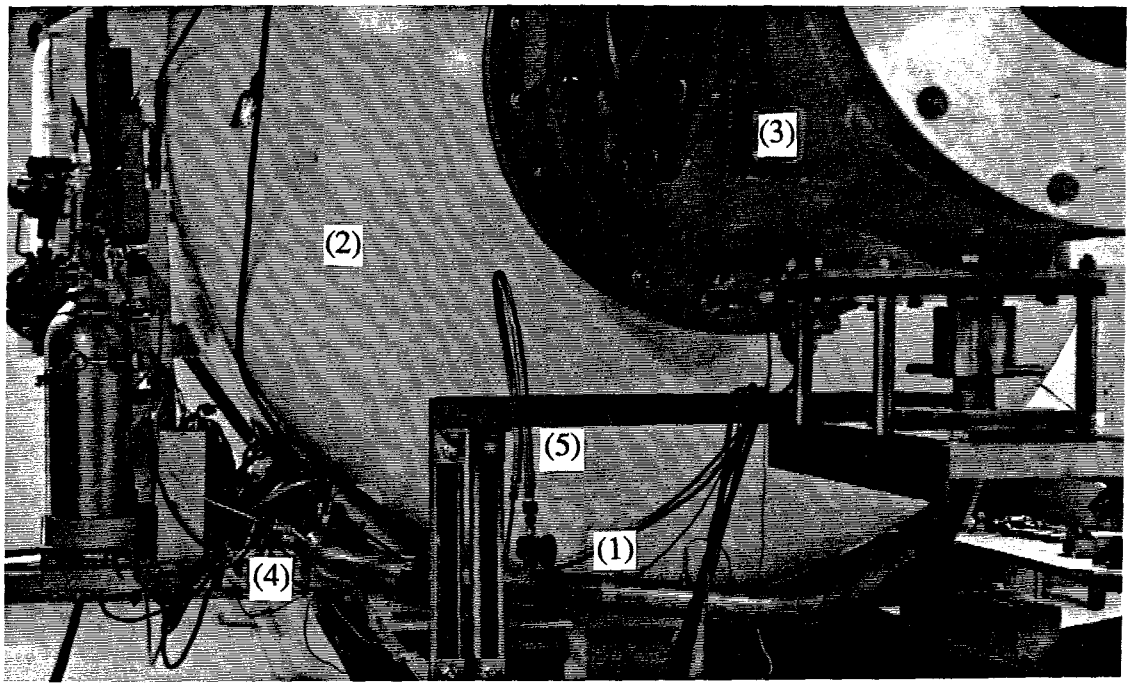

Figure 3.10 Part of the driven section connecting the driver section to the test section of T5.

The driven section of the shock tunnel is a tube 1.92 m long with an inside diameter of 2.5 cm. It is made of stainless steel and its walls are 1.25 cm thick. In the configuration to be used with T5, the driven section is made of two parts. The first part connects the driver section of the tube to the test section of T5; the second part, inside the test section of T5, brings the driven section of the combustion shock tunnel to the test model. Figure 3.10 shows the first part of the driven section (1) alongside the dump-tank (2) and test section of T5 (3). The figure also shows the driver section (4) with part of its electrical system and the driven section filling line (5).

One of the interesting characteristics of this section is that it has to make two bends before reaching the test model. The driver section of the system is mounted on the side of the movable dump tank support frame of T5 so as not to interfere with the 3 meters traveling clearance of the dump tank-test section assembly of T5. For the driven section to reach the injection point, it first makes a 45 degree turn on an horizontal plane to be able to reach the vertical symmetry plane of T5. Then a 90 degree turn upward brings it across the test section lower wall and to the model itself. The largest radius of curvature physically possible for both turns was used in order to minimize the effect of the tube curvature on the flow. Both turns have a radius of curvature of 28 cm, equivalent to 11 times the inside diameter of the tube. No effects of these bends on the performance of the system have been detected.

To be able to fill the tube to the right pressure before the test, a secondary diaphragm, usually made of mylar, is used at the end of the driven section. The diaphragm can be replaced by decoupling the two segments of the driven section and removing the section inside the test section of T5. Due to design constraints, the diaphragm is not at the extreme end of the section but rather at 5 cm from the end, leaving the remaining space under vacuum before the test.

The filling line is attached radially to the tube about half way downstream (see Figure 3.10). No particular attention was paid to the filling characteristics here because no mixing is involved in this section. This filling line is rated at 40 MPa, which is the same as for the driver section. One segment of the line is made of a flexible hose to allow for the

relative movement of the driver and driven sections necessary for main diaphragm replacement.

Two pressure transducers are mounted on the driven section. The first is 0.86 m downstream of the main diaphragm and the second is 1.055 m further downstream, only 5 mm from the end-wall. That last pressure measurement is used as the nozzle reservoir condition of the system.

Three methods have been used to determine the shock speed during a test and they agree within 5%. The first method uses the two pressure transducers in the shock tube as a timing device, from which the shock speed is easily computed. The only problem with this method is that the pressure signal coming from the first station does not always show a sudden rise, making it difficult to determine the shock speed precisely. The second method uses the two transducers in the driver section to determine the exact time of the diaphragm rupture. This information coupled with the arrival time of the shock at the end of the driven section gives a second way of finding the shock speed. Surprisingly, this method does not give a slower shock speed compared to the first method, which suggests that the shock speed is not significantly reduced by viscous effects along the way. The pressure jump at the end of the driven section has also been used to determine the shock speed. It always agrees well with the two other methods.

For all the tests, it is very important to be able to determine precisely the conditions at the end of the driven section of the tube. To do so, the shock wave relations are used to determine the conditions right after the shock reflection at the end-wall. The measured pressure at the end-wall is usually lower than the one predicted by shock wave relations. Assuming an isentropic process between the expected and the measured pressure, the conditions at the end-wall can be determined.

Examples of pressure traces from the two pressure transducers in the driven section are presented in Figures 3.11 and 3.12 for one experiment. The driven section was filled with hydrogen at 400 kPa and the driver section was filled with a 14% hydrogen mixture at 1 MPa. The time origin ($t = 0$) on these two plots is the estimated time of the diaphragm rupture.

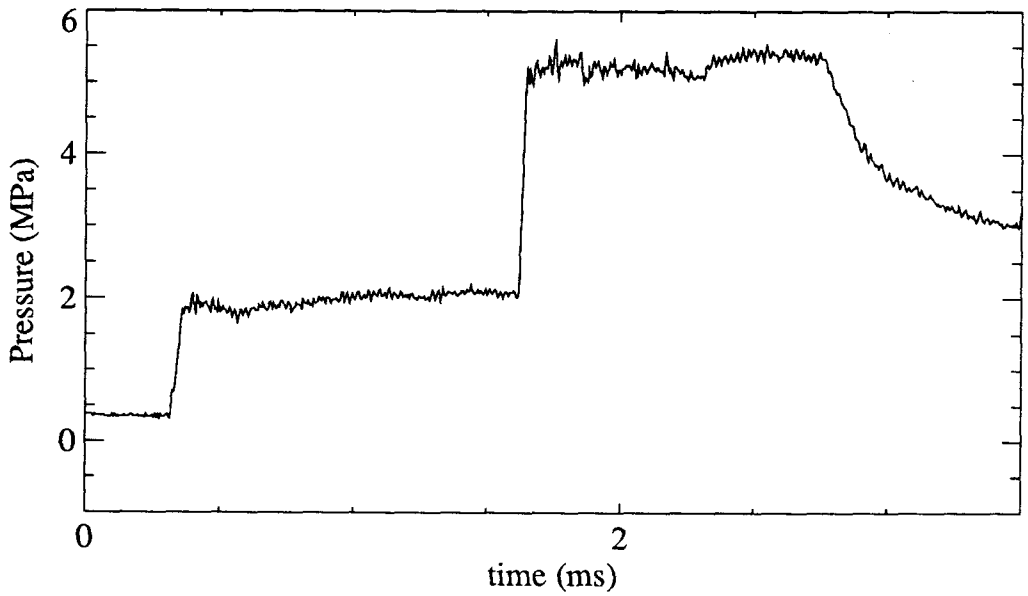

Figure 3.11 Pressure trace from transducer 0.86 m downstream of main diaphragm. Rupture of diaphragm occurred at t = 0 ms. The first rise is the incident shock, the second is the reflected shock.

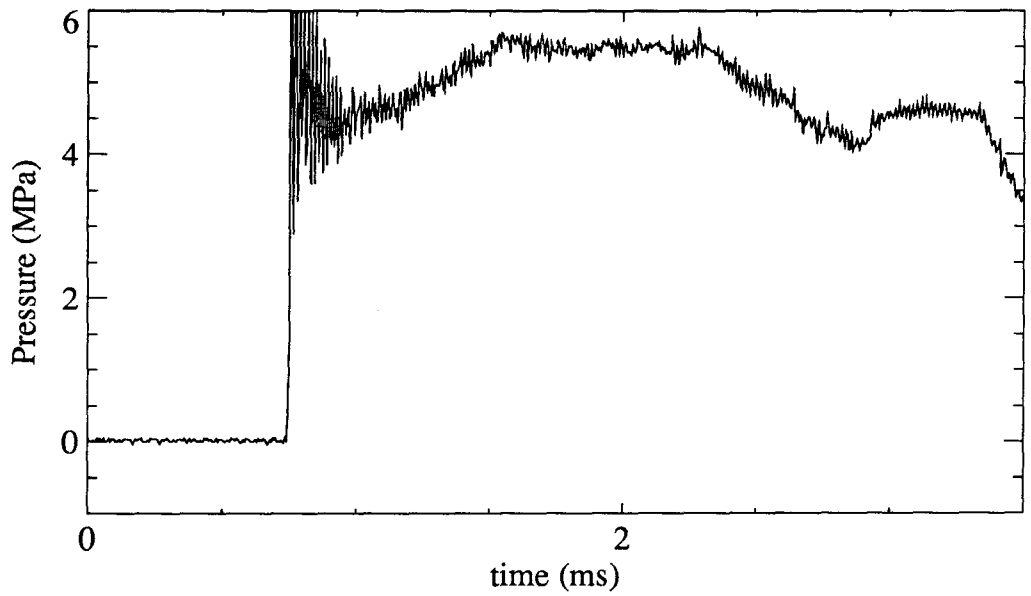

Figure 3.12 Pressure trace from transducer 1.915 m downstream of main diaphragm, 5 mm from end-wall. Rupture of diaphragm occurred at t = 0 ms.

The duration of steady pressure conditions in this experiment, as shown in Figure 3.12, was 0.8 ms, between t = 1.5 ms and t = 2.3 ms. The sudden decrease in pressure at 2.25 ms in figure 3.11 is due to the expansion wave coming from the driver section, and it reaches the end-wall at 2.3 ms in figure 3.12. Contamination of the flow by the driver gas is believed to occur at a much later time because only a small fraction of the driven gas available has been used to that point.

3.5 Diaphragm and Diaphragm Bursting System

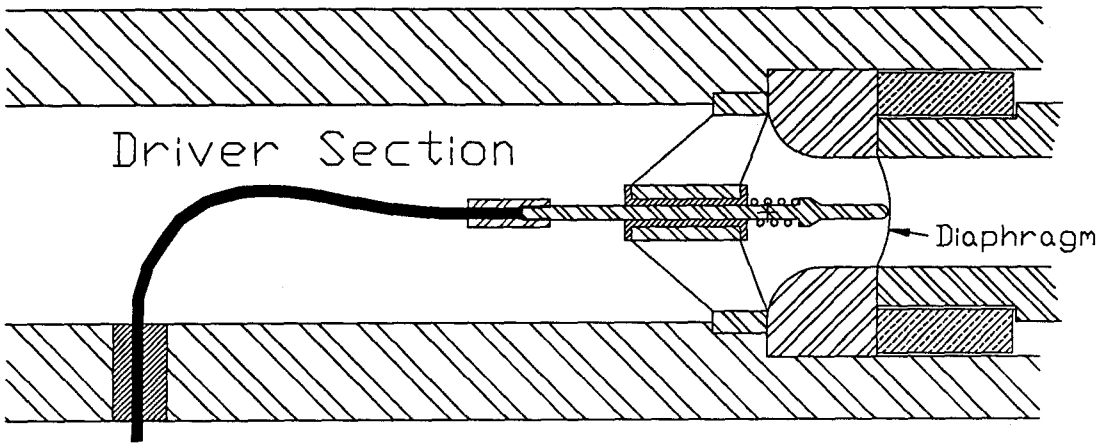

Figure 3.13 View of the diaphragm bursting system inside the driver section.

In the introduction section of this chapter, it was stated that the diaphragm bursting system must be able to break the diaphragm within 4 ms and with an accuracy of at least 0.2 ms. To be able to do so, a capacitor of 5000 μf is discharged from 250 V into the diaphragm using a probe design shown in Figure 3.13. The total resistance in the line is about 0.05 Ω, with the contact resistance between the probe and the diaphragm being the critical point. The tube itself is perfectly grounded, making it the effective ground of the system. A delay always close to 0.12 ms has been measured between the time the signal is sent to the actual breaking of the diaphragm. This delay varies slightly depending on the diaphragm used and the pressure inside the driver, but is always repeatable within 50 μs

for similar tests. Thus, this simple method easily meets the requirements for the timing of the tube.

The diaphragms are made of stainless steel, which has several advantages over the previously used aluminum ones. They are stronger, thus thinner diaphragms can be used, and their conductivity is much lower, making them very easy to melt at the contact point with the probe. The cracks from this melted point also seem to propagate better with the stainless steel diaphragm. The disadvantage with these diaphragms is that diaphragm fragments detach and are sent down the tube. This is not as critical as it could be in other systems because the two bends in the driven section effectively stop the debris from reaching the nozzle at the end of the driven section during the test time.

Diaphragm thickness (m)	Burst Pressure (with combustion) (MPa)	Max. Pressure (for tests) (MPa)	Min. Pressure (for tests) (MPa)
0.0254	1.7	1.0	0.3
0.0381	2.5	2.0	1.0
0.0508	4.0	3.5	2.0
0.0762	6.0	5.5	3.5
0.1016	8.0	7.0	5.0
0.1270	10.0	9.0	6.5
0.2032	16.0	14.5	9.0
0.3048	24.0	22.0	14.0

Table 3.1 Diaphragm thicknesses available with their bursting pressure in combustion tests and the range of pressure where they can be used in real experiments.

Cold tests have shown that these diaphragms can withstand pressures of about 100 MPa per mm of thickness. When tested in combustion experiments, their burst pressure was reduced by about 20% due to the high temperature in the tube. The ability of the diaphragm bursting system to break the diaphragms in a repeatable way has been proven

with pressures after combustion as low as 25% of the maximum pressure for the smaller diaphragms. Table 3.1 shows the different diaphragm thicknesses used with the bursting pressure in combustion tests and the range of pressure in which they can be used in real experiments.

3.6 System Overall Efficiency

It is possible to predict the shock speed in the combustion-driven shock tunnel because the pressures and temperatures are known in the tube a few milliseconds before the diaphragm rupture. To make a prediction, a shock tube equation is used (equation 3.1). Notice the g factor in the denominator, which takes into account the area change between the driver and driven section. If both sections have the same diameter, the factor is equal to one, but in this shock tunnel, where A_4 / A_1 is equal to 4, it can be theoretically estimated that g is about 1.04.

$$\frac{P_4'}{P_1} = \frac{1 + \frac{2\gamma_1}{(\gamma_1 + 1)}\left(Ms^2 - 1\right)}{\left[g - \frac{(\gamma_4 - 1)}{(\gamma_1 + 1)}\frac{a_1}{a_4}\frac{\left(Ms^2 - 1\right)}{Ms}\right]^{\frac{2\gamma_4}{\gamma_4 - 1}}} \qquad (3.1)$$

Figure 3.14 shows the relation between Ms and P_4'/ P_1 given by equation 3.1 and the experimental results. γ_1 and γ_4 are the ratio of specific heats for the driven and driver gas, respectively. a_1 is the speed of sound in hydrogen at room temperature an a_4 is the estimated speed of sound of the driver gas after combustion. Shock speed between 10% and 15% lower than expected was measured. This difference is probably due to some viscous effects. It is at this point impossible to determine if the two bends in the driven section or the rather crude transition between the driver and driven section have any effect on the shock speed .

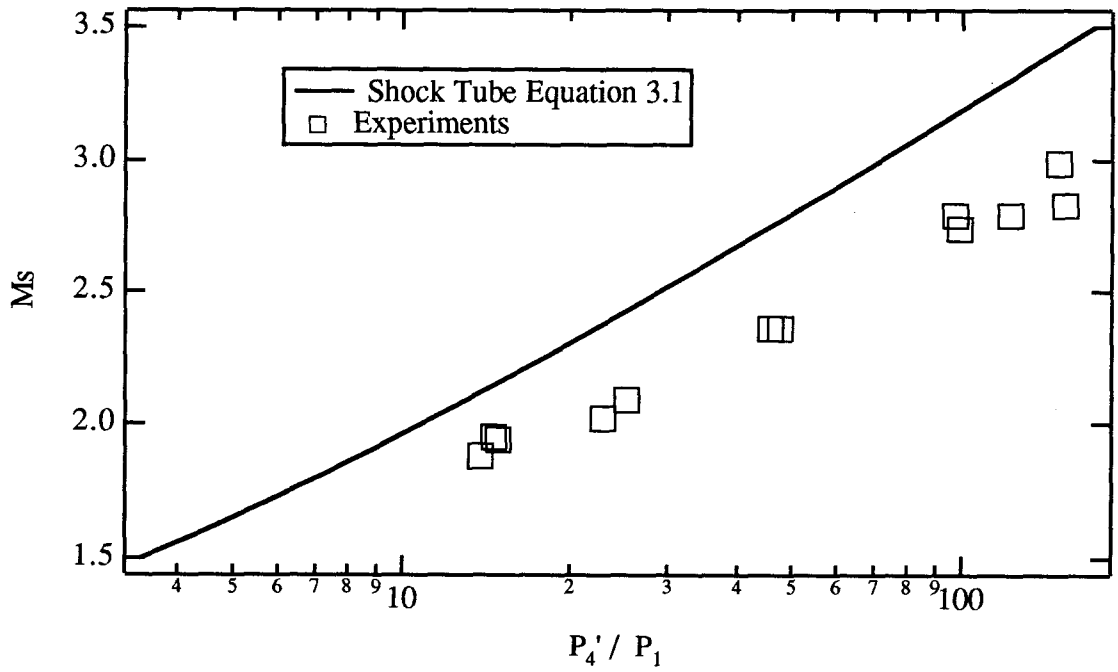

Figure 3.14 Relation between Ms and P_4'/P_1 given by equation 3.1 for g = 1.04 and the experimental results.

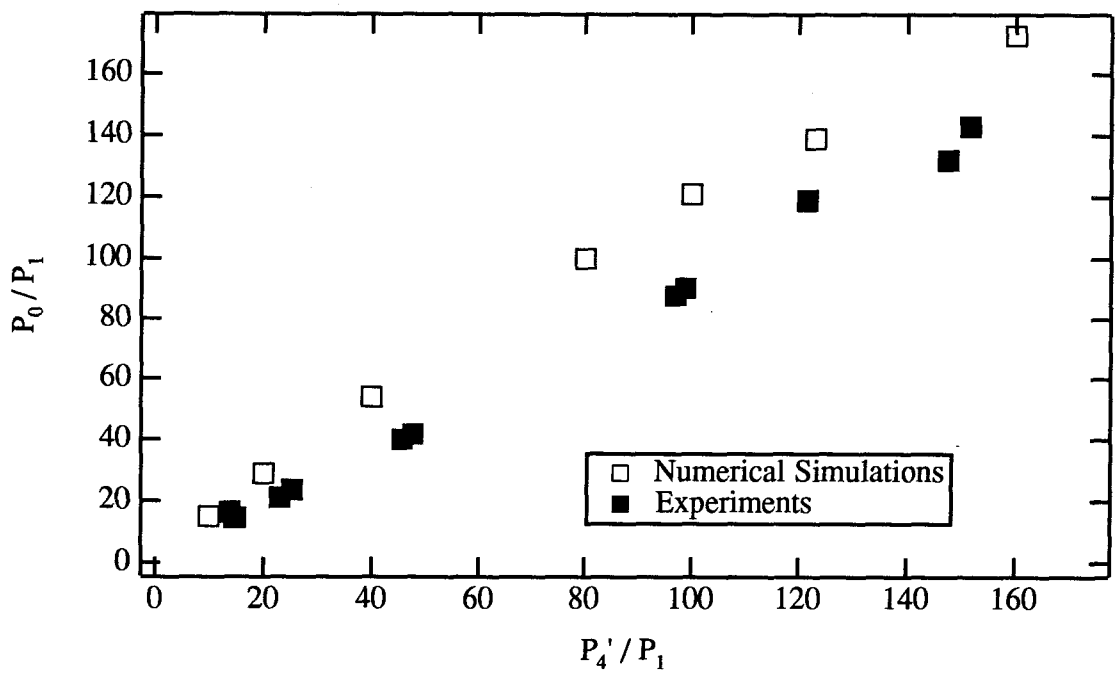

Figure 3.15 Pressure obtained at the end-wall of the driven section as a function of the pressure after combustion in the driver section.

To evaluate the overall efficiency of the combustion driven shock tunnel, it was compared to results from the numerical code presented in chapter 2. Figure 3.15 shows the pressure obtained at the end-wall of the driven section as a function of the pressure after combustion in the driver section; both pressures are normalized by the initial pressure in the driven section. According to the numerical simulations the pressure recovery ratio P_0 / P_4' should be around 1.25, but the experimental results show a recovery ratio of about 0.9, a comparative efficiency of only 72%. Again the viscous effect is believed to be the major factor in this lower pressure recovery. With a driver section maximum pressure of 25 MPa, this gives a maximum pressure at the end-wall of the driven section of about 22.5 MPa.

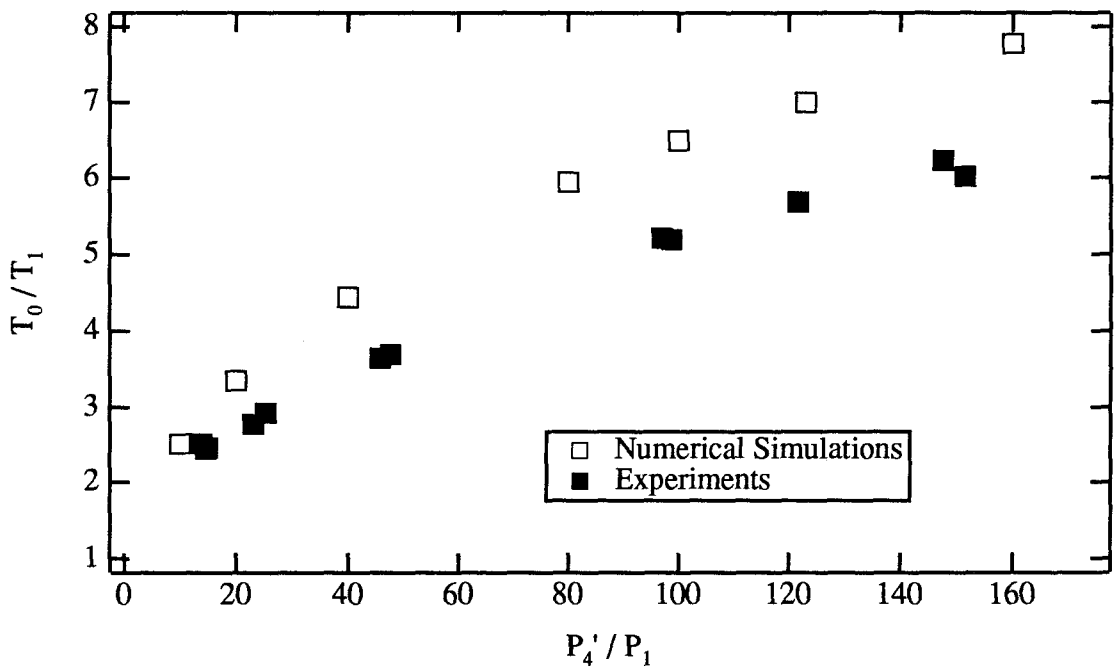

Figure 3.16 Temperature obtained at the end-wall of the driven section as a function of the pressure ratio between the driver and driven section.

Also very important in these tests is the temperature of the compressed gas during the test. Figure 3.16 shows the numerical simulation results and the experimental temperatures obtained as a function of the pressure ratio between the driver and driven section. The experimental temperatures were evaluated using the measured shock speed and an isentropic process between the conditions behind the reflected shock and the final conditions. Temperatures 20% below the values predicted by the numerical code have been

obtained. To compensate for this reduction, the pressure ratios P_4'/P_1 have to be taken up to 1.8 times larger than predicted. This difference has the effect of reducing the available test time by the same amount due to the fact that the filling pressure in the driven section must be lowered to get the right pressure ratio.

3.7 Conclusion

All the problems related to the combustion driven shock tunnel have been solved and as will be seen in the next two chapters, the system has been used successfully to heat hydrogen to 1500 K for combustion experiments in the free piston shock tunnel T5.

The lower overall efficiency of the actual system compared to the one predicted by the numerical code was expected and, as stated before, is most certainly due to some viscous effects. No particular part of the tunnel is believed to be responsible for this somewhat low efficiency. Thus, for the near future, no major modifications of the system are planned. The only area where it might be worth making some changes in the long term would be to redesign the filling lines of the driver section to make sure that the mixture is always well mixed.

Chapter 4
Instrumentation and Data Reduction

4.1 Introduction

This chapter presents the few missing parts needed before going into the results of the mixing and combustion experiments themselves. Although the free piston shock tunnel T5 was described for the numerical simulation in chapter 2, it seems appropriate here to go back and describe the general features of the system and explain how it works. This description is the subject of section 4.2. The other section in this chapter, section 4.3, describes the instrumentation of the system and the general data reduction techniques used in chapters 5 and 6.

4.2 The Free Piston Shock Tunnel T5

The free piston shock tunnel T5 has been built at GALCIT to experimentally study flows up to orbital speed. To achieve such high velocities in the test section of a shock tunnel, the driven gas enthalpy must be brought up to the 20 to 30 MJ/kg range. To accomplish this, a shock-wave in the driven section of the tunnel must have a speed of the order of 5 km/s. To drive such a fast shock, not only must the pressure ratio between the driver and the driven gas be very high but the speed of sound ratio between the two must be as large as possible. The purpose of the free piston driver is the generation of sufficiently high temperature and pressure in the driver section to achieve such shock velocities. Helium is usually used as a driver gas because it is a light gas and has no low-energy internal degrees of freedom and hence behaves like a perfect gas up to relatively high temperatures.

Figure 4.1 gives a general view of the facility with the driver section on the right side, the driven section on the left, and the large inertial mass in between the two. The facility has been named T5 because it is the fifth free piston shock tunnel built by or under the supervision of R. J. Stalker (see Stalker, 1989 and Morrison et al., 1989). The previous four smaller ones have been built in Australia.

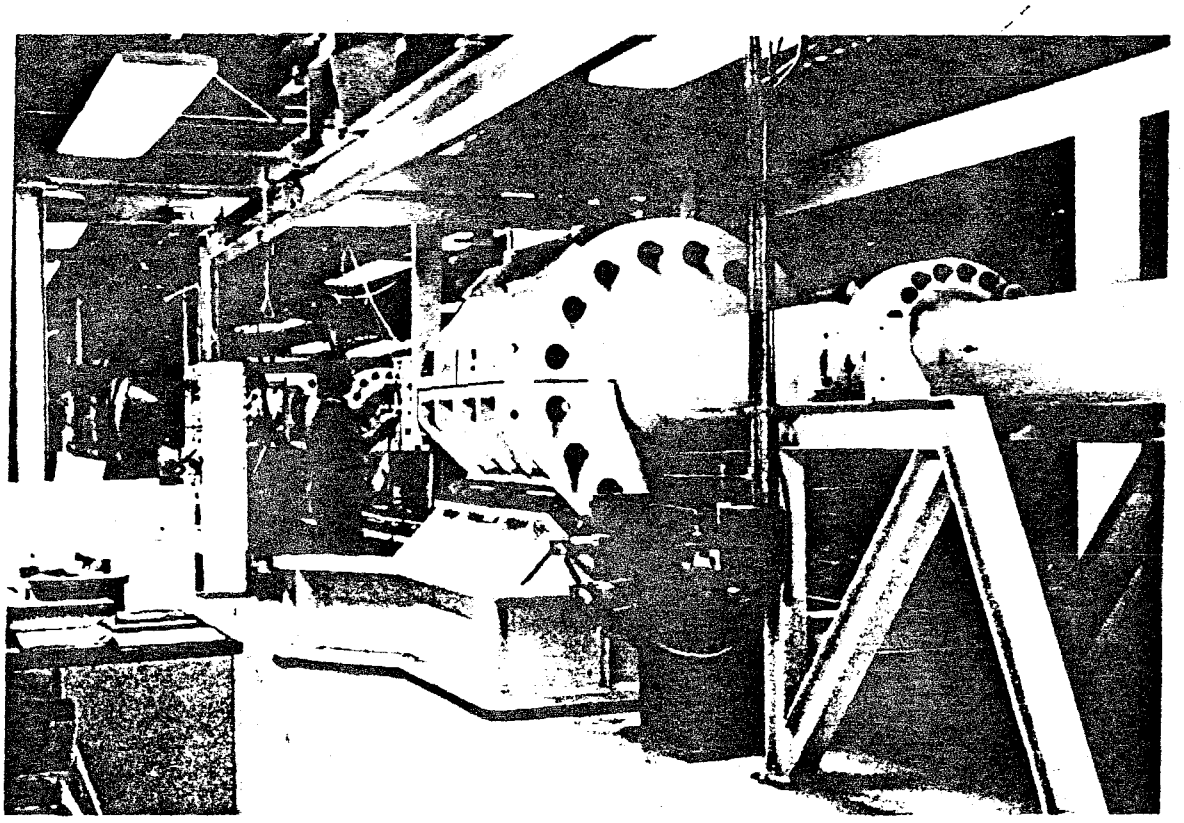

Figure 4.1 General view of the free piston shock tunnel T5.

The principal parameters of the system are

Maximum secondary reservoir pressure	15	MPa
Maximum diaphragm burst pressure	130	MPa
Piston mass	120	kg
Driver section diameter	0.3	m
Driver section length	30	m
Driven section diameter	0.09	m
Driven section length	12	m
Nozzle exit diameter	0.3	m

The arrangement of the different parts is shown in the drawing of figure 4.2. In this drawing the flow is from left to right, not the other way around as in figure 4.1.

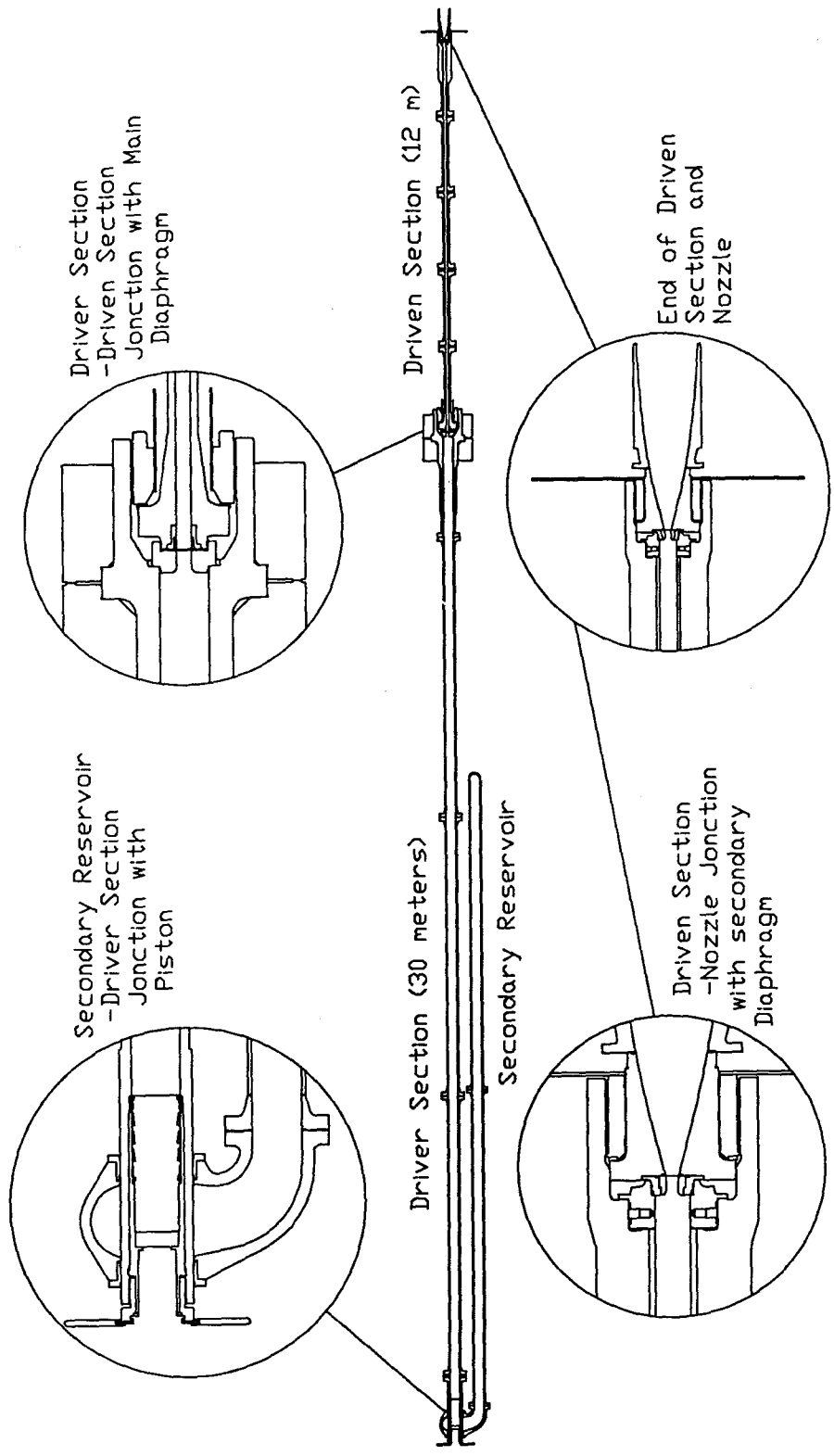

Figure 4.2 Arrangement of the different parts of the free piston shock tunnel T5 with details of the critical sections.

A typical test with the free piston shock tunnel T5 is as follows: Compressed air in the secondary reservoir at a pressure of 10 MPa drives the 120 kg piston along the driver section compressing the helium in front of it; the helium is originally at 120 kPa. The downstream end of the section is closed by the main diaphragm, which has a burst pressure of 100 MPa. The piston compresses the helium to 1/55 of its original volume before the diaphragm bursts. At that time the helium has reached a temperature of about 4000 K and a speed of sound of 3700 m/s. With only about 20 kPa of air in the driven section, a shock wave traveling at 4600 m/s is formed. Once the shock reaches the end, a reflected shock is formed to stop the flow. In that small region at the end of the driven section, the driven gas reaches a temperature of about 9000 K and a pressure of 70 MPa. From there, the gas is expanded with a contoured nozzle that has an area ratio of 100 into the test section.

As the piston accelerates along the driver section, this center of mass shift is compensated by a recoil of the driver and driven sections, as well as the nozzle at the end of the driven section. The test section and dump tank remain stationary, and the secondary air reservoir recoils in the opposite direction under the action of the thrust of the outflowing air. To accommodate the resulting relative motions, the nozzle-test section joint and the secondary reservoir-driver section joint are fitted with sliding axial seals. The recoil speed determines the level at which the system is stressed by a wave released by the rapid piston deceleration. This stress and other considerations make it desirable to reduce the recoil speed as much as possible. For this reason a 14 ton inertial mass (prominent in figure 4.1) is fixed to the high pressure end of the driver section, the origin of the stress wave. The recoil distances are typically 100 mm and 150 mm for the driver section and secondary reservoir, respectively.

The flow conditions in the test section are determined as follows. The initial shock speed in the driven section of the facility is evaluated using the arrival time of the shock wave at the different pressure transducers along the tube. The shock speed is then used along with the initial driven gas pressure and the measured reservoir pressure at the entrance of the nozzle as input to an equilibrium shock tube calculation (McIntosh, 1971).

The program evaluates the conditions behind the incident and reflected shocks using the shock velocity and the initial pressure, composition, and temperature in the section. These conditions after the reflected shock are then changed isentropically so that the total pressure matches the measured one. These reservoir conditions are then fed to a quasi one-dimensional nonequilibrium nozzle calculation NENZFG (Lordi et al., 1965) or a fully two-dimensional calculation SURF (Rein, 1989) to give the conditions at the exit of the nozzle.

4.3 Instrumentation

4.3.1 Data Acquisition System

The system is controlled from a Sun SPARCstation computer, with software facilities enabling "quick-look" examination of the data immediately after the shot. A second Sun SPARCstation computer is used for more extensive data reduction even during preparation for tests.

Currently, the modular data acquisition system consists of

- 40 A/D programmable digitizing channels
- 24 programmable amplifier channels
- 8 programmable trigger generator channels
- 1 digital counter
- 1 programmable digital delay generator, and
- 24 PCB piezotronics pressure transducer power supplies

The digitizing channels have a resolution of 12 bits and a maximum sampling rate of 1 MHz. The total through-put of the digitizing channels is limited to 16 MSamples/s. The amplifier channels have been used mainly in conjunction with the thermocouples, for which the output signal is very weak, but could be used for other applications. The digital delay generator is usually used to trigger the flow visualization laser.

4.3.2 Pressure and Heat Transfer Data Reduction

The flat plate model, tested in chapter 5, was installed with PCB piezotronics pressure transducers and MedTherm corporation thermocouples mounted flush on its surface. In that set of tests, there was also a PCB piezotronics pressure transducer used for pitot pressure measurement. In the case of the tests inside a duct, presented in chapter 6, only surface pressure measurements were taken with the PCB piezotronics pressure transducers. All the data presented in these two chapters were time averages over the period starting 0.5 ms after flow start and lasting 0.75 ms. In every case, the sampling rate was 200 kHz. The first 0.5 ms of the flow measurement were not used because of the starting process and it was stopped 0.75 ms later to make sure that the test slog was not yet contaminated by the driver gas. Figure 4.3 shows the first 1.5 ms of the driven section reservoir pressure and the measured pitot pressure in the test section for shot number 242.

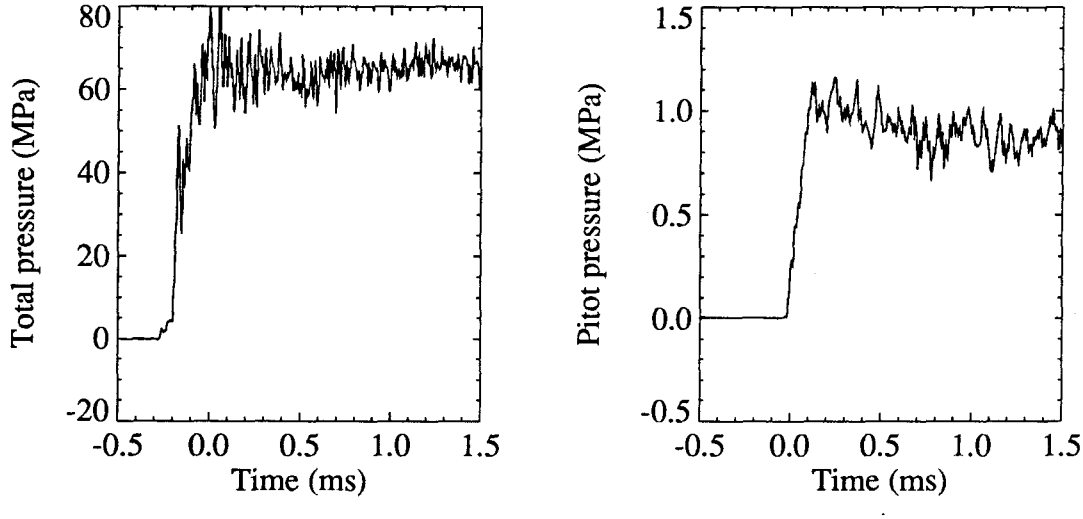

Figure 4.3 Total reservoir pressure and pitot pressure measurement for shot 242; data not filtered.

The pressure transducers used on the models have a built-in charge amplifier, so the output voltage is proportional to the pressure. The discharge time constant is 1 s, which is about 500 times the event duration. The time response is one microsecond with a resonance frequency of 500 kHz. Thei quartz element is acceleration-compensated but, as

may be seen in figure 4.4, the noise level can be very large. Shot 242, on the left, is with the flat plate model made of aluminum and can be compared to shot 391, with the combustor model made of steel. The pressure transducers were mounted the same way in both models making the ringing of the aluminum the most probable cause of the very high noise level. As it turned out, the pressure measurements with the aluminum flat plate model did not reveal any useful information and so none of the important results in chapter 5 depend on them.

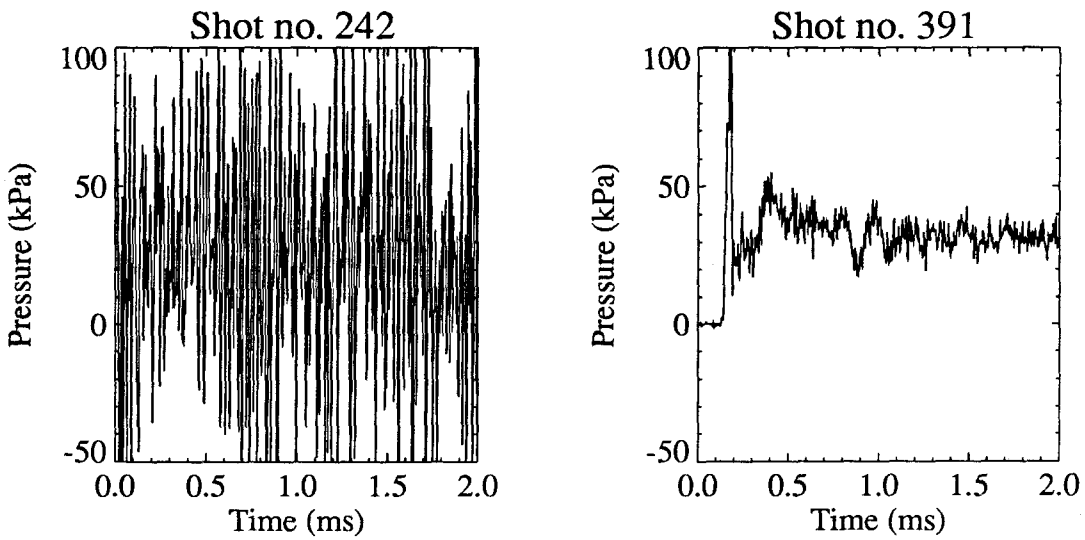

Figure 4.4 Surface pressure measurement for shot 242 on an aluminum flat plate and for shot 391 inside a steel duct; data not filtered.

The coaxial thermocouples used have a diameter of 1.6 mm and are the chromel-constantan type (type E). Their response time is claimed by the manufacturer to be as little as 1 microsecond. Figure 4.5 shows the unfiltered data recorded by the data acquisition system after being amplified by a factor of 500. Also presented on this figure is the converted voltage to temperature change using the polynomial fit by Avallone and Bannierster (1987). These data also come from shot 242 and, as may be seen, the thermocouples are much less sensitive to vibrations.

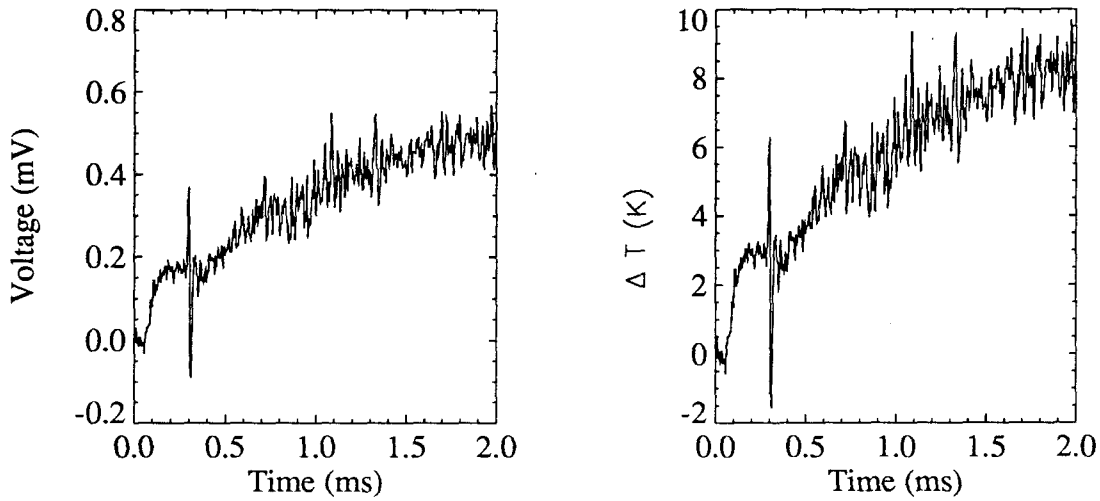

Figure 4.5 Thermocouple voltage measurements and conversion to temperature change for shot 242 on the surface of the flat plate; data not filtered.

The relationship between the surface temperature and the heating rate for one-dimensional heat conduction into a homogenous semi-infinite solid is given by

$$\dot{q}(t) = \sqrt{\frac{\rho c k}{\pi}} \int_0^t \frac{dT(\tau)}{d\tau} \frac{d\tau}{\sqrt{t - \tau}}, \tag{4.1}$$

where ρ, c and k are, respectively, the gage material density, specific heat, and thermal conductivity; t is the time from the start of the heating; and finally T(t) is the surface temperature rise. This semi-infinite model is an excellent approximation in this case because, the test time being less than 2 ms, the heat penetration is less than a millimeter.

A finite-difference representation of equation 4.1 can be used to determine the heat transfer rate. However, to use this method it is necessary to eliminate noise from the data using some filtering technique before the integration can be performed. The method used instead, called the indirect method, computes the cumulative heat input Q(t) and then differentiates the results to obtain the heating rate. The cumulative heat input to a semi-infinite solid is given by

$$Q(t) = \sqrt{\frac{\rho c k}{\pi}} \int_0^t \frac{T(\tau)}{\sqrt{t - \tau}} d\tau , \tag{4.2}$$

and the finite-difference representation is

$$Q(t) = \sqrt{\frac{\rho c k}{\pi}} \sum_{j=1}^{n} \frac{T_j + T_{j-1}}{\sqrt{t_n - t_j} + \sqrt{t_n - t_{j-1}}} (t_n - t_{n-1}) . \tag{4.3}$$

The expression used for differentiating the discrete function Q(t) is

$$\dot{q}_n = \frac{dQ_n}{dt} = \frac{1}{40(t_n - t_{n-1})} [-2Q_{n-8} - Q_{n-4} + Q_{n+4} + 2Q_{n+8}] . \tag{4.4}$$

The initial integration to obtain Q(t) is good enough to smooth the data sufficiently so that no filtering is required. Figure 4.6 shows the cumulative heat input and heat transfer rate for shot 242 using equation 4.3 and 4.4. Once again, a time average lasting 0.75 ms, 0.5 ms after flow start, was used for all the data presented in chapter 5.

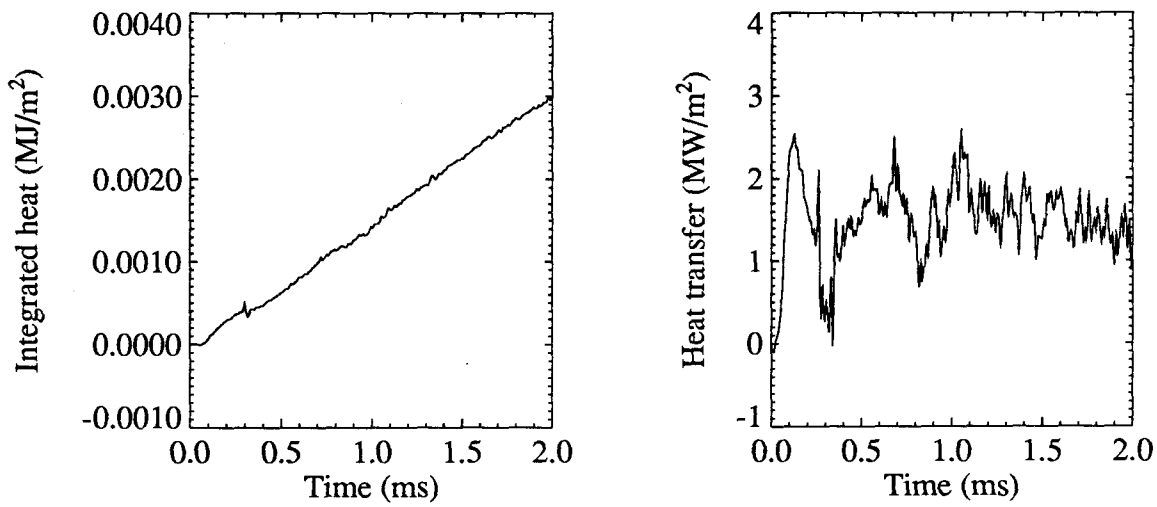

Figure 4.6 Cumulative heat input and heat transfer rate for shot 242 on the surface of the flat plate; data not filtered.

The heat transfer rates were then normalized using the Stanton number

$$St = \frac{\dot{q}}{\rho_\infty u_\infty (c_{p\infty} T_\infty + \frac{r u_\infty^2}{2} - c_{pw} T_w)}, \qquad (4.5)$$

where r, the recovery factor, is taken to be $Pr^{1/2}$ with Pr = 0.7 for both air and nitrogen.

4.3.2 Flow Visualization

In chapter 5, experiments using a simple differential laser interferometry system are presented. The interferogram was made using a Wollaston prism with a divergence angle of 2'15". The optical layout was a typical z shape single pass system with one optical table on each side of the test section. The spherical mirrors had a focal length of 10' (3.049 m) and a diameter of 8 in. (203.2 mm), the same diameter as the test section windows. The light source was an injection-seeded, frequency-doubled, Nd:YAG laser producing pulses at 532 nm wavelength, about 5 mJ pulse energy, and 6 ns pulse width. The laser can produce up to 200 mJ pulses.

In chapter 6, the same optical layout for differential interferometry was used. The Wollaston prism used in this case had a divergence angle of 34", giving the interferometry a better spatial resolution. To increase the sensitivity of the system, resonant enhancement of the refractive index of the medium was used. The technique relies on the fact that the refractive index of a gas goes through a maximum very close to a spectral line of the medium. The value of the refractive index at this maximum is very considerably above the broad-band value. This technique was achieved in these experiments by seeding the hydrogen jet with sodium in the form of salt and using a light source with a wavelength just off on the red side of the higher energy D-line of sodium. To give an idea of the increase in sensitivity, only 100 parts per billion of sodium would have to be present in the flow to get good sensitivity. The light source was a tunable dye laser built in the laboratory for that purpose. The laser is pumped by the Nd:YAG laser

and can produce 40 mJ pulse at about 589 nm wavelength with a bandwidth of about 3 GHz. The dye used is Rhodamine 610. Help from Eric Cummings and Patrick Germain, both from the T5 group, was instrumental in making this technique work for this research project.

Chapter 5
Flat Plate Experiments

5.1 Introduction

This chapter presents the results of the experiments on hydrogen injection from a flat plate at zero angle of attack in the flow of T5. The main goal of this part of the research was to determine to what extent it is possible to mix and burn hot hydrogen in an hypersonic air flow. According to data available (see Huber et al., 1979), in the case of a transverse fuel jet into a supersonic air stream:

- in the typical case of fuel stagnation temperature much less than air stagnation temperature, the ignition very likely occurs in those regions where the mixture equivalence ratio is approximately 0.2;
- the likely regions for self-ignition in the combustor seem to be
  1- the upstream recirculation region of the transverse jet,
  2- the bow shock region of the fuel jet.

The signs for combustion in the first region will be examined using the pressure transducers and the thermocouples on the plate, downstream of the injector. It is believed that if there is ignition in the upstream recirculation region, the combustion will be convected downstream in the boundary layer and will be picked up by the instrumentation there. The bow-shock self-ignition region will be examined using flow visualization by differential interferometry. A comparison of the position of the bow-shock will tell us if enough energy is released in the combustion case to move the bow shock upstream.

A description of the test model is presented in section 5.3 and the tests conditions, for each case studied, are described in section 5.4. All the experimental results from the pressure transducers, the thermocouples, and the optical system are presented in section

5.5, followed by a discussion of these results in section 5.6. But first, let's look back at previous work that has been done in this type of flow.

5.2 Research Review

In the 1960's and early 1970's, a group of researchers became interested in the flow generated by injection of an axisymmetric transverse jet into supersonic flows mainly for fuel injection purposes, but some researchers were also interested in thrust vector control of rocket motors. Zukoski and Spaid (1964), Orth and Funk (1967), Schetz et al. (1968), and Rogers (1971) were all primarily interested in determining penetration depth and mixing quality of normal injection into the supersonic airstream. The penetration height of the jet was determined using gas chromatography and also schlieren and shadowgraph pictures. More recent work by Papamoschou et al. (1991) using a schlieren system and also by McDaniel and Graves (1986), Lee and Linevsky (1992), and Rothstein and Wantuck (1992) using planar laser induced fluorescence has brought a considerable amount of new data on the subject. The problem today is that all these data do not correlate very well and attempts to define an empirical formula for the penetration height of the jet have not been successful. Theoretical studies were also published by Schetz and Billig (1966) and, more recently, by Quan et al. (1990) and numerical simulations were done by Heister and Karagozian (1990) and Fujimori et al.(1991).

The first experimental work on a transverse jet at an angle different than 90^{o}, known to the author, was done by McClinton (1972). He found that he could reduce free-stream momentum and total pressure losses and improve fuel distribution and mixing by injecting at angles as low as 30^{o}. In the last few years, this low angle injection geometry was experimentally studied by Mays et al. (1989), Lee et al. (1990), Morgan and Casey (1990), Riggins and McClinton (1991), and Loomis et al. (1992). The last two groups also used extensive CFD calculations in an attempt to correlate their results.

Since 1989, quite a few different techniques for injecting fuel have been tested. The transverse slot injection has been studied experimentally by Aso et al. (1991) and

Wantuck et al. (1991) and numerically by Takahashi and Hayashi (1991). The case of tangential slot injection was looked at by Anderson et al. (1990) and Casy et al. (1992). Another technique used in many experiments is the transverse injection behind a rearward-facing step. The step creates a large recirculation zone used as a flame holder. Work by Uenishi et al. (1989), Fletcher and McDaniel (1989), Correa et al. (1990), Segal et al.(1991), and Parker et al. (1992) presents some of the results using that technique. More complex injector configurations involving ramps and other mixing enhancement techniques have also been tested but will not be discussed here.

It is interesting to note that in all these studies no one has tried to inject hot fuel. Except for tests done in T5 for Rocketdyne and the hot Ludwieg tube at Boeing, the only published attempt to inject hot hydrogen is underway in Queensland, Australia by Wendt (1990).

5.3 Test Model

The nozzle exit of the injection system was mounted flush with the surface of the flat plate for all cases. The width of the flat plate is 28 cm and its total length is 50 cm. The plate was mounted 2.5 cm lower than the centerline of the nozzle of T5 so that the core of the flow could pass over the plate.

Figure 5.1 shows the position of the injection point relative to the leading edge of the flat plate. The injector shown here is the Mach 2, 30^{o} injector. The positions of the pressure transducers and the thermocouples are also shown on the figure. The injector nozzle is 292 mm from the leading edge of the plate and the first pressure transducer is 63.5 mm downstream of the injector.

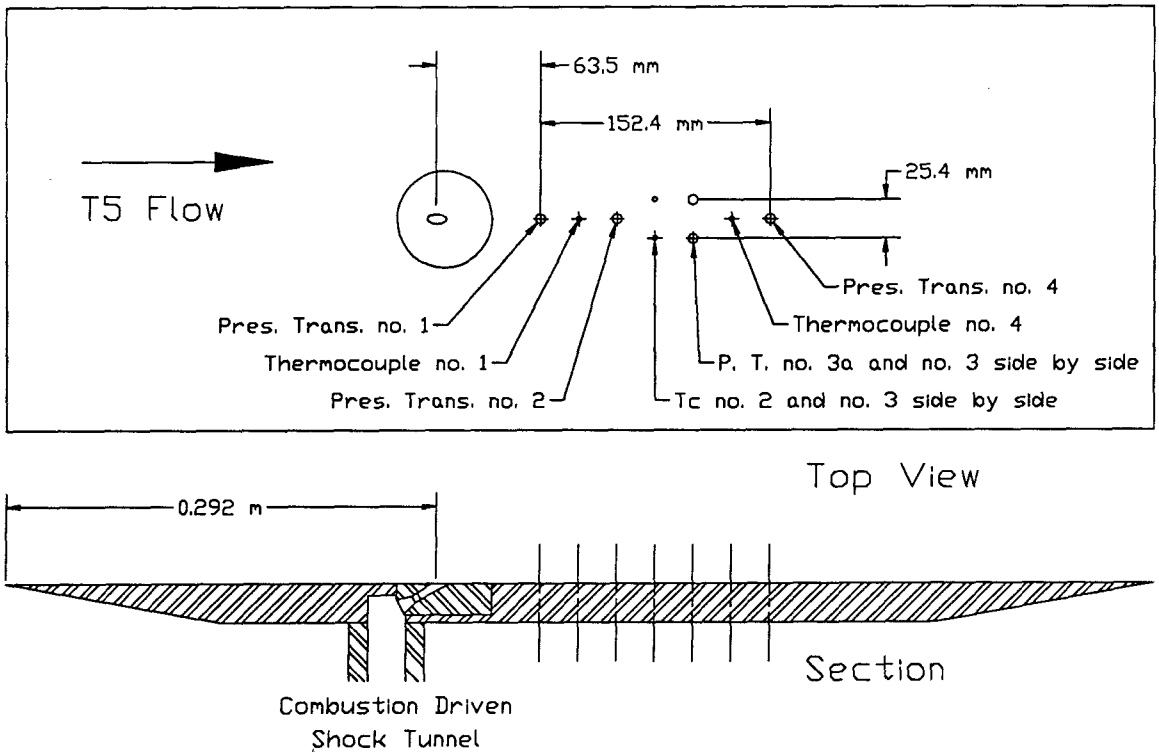

Figure 5.1 Top view and side view of the flat plate with injector nozzle position and instrumentation location.

	x (mm)	y (mm)
Pressure Transducer no. 1	63.5	0.0
Pressure Transducer no. 2	114.3	0.0
Pressure Transducer no. 3	165.1	12.7
Pressure Transducer no. 4	215.9	0.0
Thermocouple no. 1	88.9	0.0
Thermocouple no. 2	139.7	-12.7
Thermocouple no. 3	139.7	12.7
Thermocouple no. 4	190.5	0.0

Table 5.1 Position of the instruments relative to the injection nozzle, x being along the flow direction and y perpendicular to it.

The pressure transducer no. 3a shown on the figure was not reliable and none of the measurements from it will be presented here. Table 5.1 shows the exact position of the other instruments relative to the center of the injection nozzle, x being along the flow direction and y perpendicular to it.

5.4 Test Conditions

Five different cases were studied, three involving a transverse jet at Mach 2 injecting at a angle of 30° relative to the main flow. The difference between these three cases is the differences in the flow conditions of T5. The two last cases repeat one of the three previous T5 flow conditions, but use different injectors. Table 5.2 shows the reservoir conditions and the test section conditions of T5 in air with the injector type for each case. The contoured nozzle of T5 has an area ratio of 100. Conditions in the test section are computed using the quasi one-dimensional reacting nozzle flow code NENZFG (Lodi, 1965).

Case		1	2	3	4	5
T5 Reservoir Conditions:						
Total Pressure	(MPa)	56.9	42.2	65.6	54.5	56.9
Total Temperature	(K)	6250	8135	8380	8200	8245
Total Enthalpy	(MJ/kg)	10.4	16.3	16.5	16.1	16.2
T5 Test Section Conditions						
Temperature	(K)	1545	2255	2450	2335	2365
Pressure	(kPa)	26.6	20.9	33.8	27.6	28.9
Density	(kg/m^3)	0.059	0.030	0.045	0.039	0.040
Velocity	(m/s)	4060	4920	4980	4915	4935
Mach Number		5.33	5.26	5.19	5.22	5.21
Injector Configuration						
Nozzle injector angle	(degree)	30	30	30	30	15
Nozzle injector Mach number		2	2	2	5	5

Table 5.2 Main flow characteristics and injector configuration for the five cases studied in air.

The Mach 5 nozzle injectors are also contoured with a throat diameter of 1.25 mm. The shape of these injectors was computed using the Rockwell International 9R-313 computer code where an approximation of the displacement thickness was added to the nozzle contour. The Mach 2 nozzle is conical with 2.5° half angle and a throat diameter of 4.75 mm.

The three first cases were studied to see if a combustion limit could be determined. Case no. 1, with lower enthalpy than the two other cases, will be referred to as the high pressure-low enthalpy case. In the same way, case no. 2 will be referred as the low pressure-high enthalpy case and case no. 3 as the high pressure-high enthalpy case. The two other cases, combined with case no. 3, were studied to see if there was a significant difference in the combustion between the high exit temperature of the hydrogen with the Mach 2 nozzle compared to the much colder hydrogen jet in the Mach 5 case. The 15° injection angle was also studied to see if combustion was significantly reduced at this low injection angle. Cases no 4 and 5 will be referred to as the Mach 5, 30° case and the Mach 5, 15° case, respectively.

Case		1	2	3	4	5
T5 Reservoir Conditions:						
Total Pressure	(MPa)	56.9	42.2	65.6	54.5	56.9
Total Temperature	(K)	7340	8740	8995	8830	8871
Total Enthalpy	(MJ/kg)	10.6	16.5	16.8	16.4	16.5
T5 Test Section Conditions						
Temperature	(K)	1395	2175	2325	2225	2250
Pressure	(kPa)	22.0	19.2	30.7	25.1	26.3
Density	(kg/m^3)	0.053	0.029	0.043	0.037	0.038
Velocity	(m/s)	4230	5030	5115	5045	5065
Mach Number		5.75	5.50	5.43	5.46	5.46

Table 5.3 Main flow characteristics for the five cases studied in nitrogen.

For each of these five cases, four different tests were performed. Hydrogen was injected into both air and nitrogen to compare experiments with and without combustion, and helium was injected into both gases to see the differences between air and nitrogen in a non-combustion condition. These four different tests were necessary because a first set of experiments without helium injection were almost impossible to interpret. The condition differences between air and nitrogen in the test section made a direct comparison of the results very difficult. Table 5.3, showing the flow conditions for the nitrogen tests, can be compared to table 5.2 for the air, to get an idea of the differences between the two flows.

The oblique shock angle at the injection point may be estimated using an axisymmetric flow approximation. This approximation gives an oblique shock angle of 36^o for the 30^o injection angle and 20^o for the 15^o injection angle. It is very difficult to estimate the flow conditions behind this shock at the injection point, first, because the problem is not really axisymmetric and second, because the flow is not in equilibrium and nonuniform. An estimate of these conditions was necessary because it was decided to try to match the pressure and the velocity of the two flows at the injection point for at least the three first cases studied.

Case		1	2	3	4	5
Hydrogen Injection						
Total Pressure	(MPa)	1.22	2.37	1.83	14.1	5.47
Total Temperature	(K)	1060	1070	1075	770	1035
Exit Pressure	(kPa)	156	303	234	26.6	10.3
Exit Temperature	(K)	590	595	600	130	173
Exit Velocity	(m/s)	3690	3705	3715	4305	4990
Helium Injection						
Total Pressure	(MPa)	1.22	2.37	1.83	14.1	5.47
Total Temperature	(K)	2000	1960	1800	1130	1680
Exit Pressure	(kPa)	147	285	220	53.0	20.6
Exit Temperature	(K)	855	840	771	120	180
Exit Velocity	(m/s)	3445	3410	3270	3235	3945

Table 5.4 Injection conditions for hydrogen and helium in the five cases studied.

It was not possible to match the pressures for the Mach 5 injector nozzles; it would have implied a stagnation pressure in the injector of 140 MPa. A reservoir pressure of about 14 MPa was chosen for the case no. 4 and a similar p_{jet} / p_{flow} at the injection point was used for the case no. 5. Using these criteria, the injector conditions for hydrogen and helium were determined and are presented in table 5.4. The same conditions were used for tests in air and in nitrogen. The hydrogen injections were done with reservoir temperature of about 1050 K, except for case no. 4, where the temperature was lowered to keep the relative velocity of the air and hydrogen at about the same level. For each case, the velocities at the injection point were matched to within 400 m/s.

The Reynolds numbers based on x near the injection point for the air flow in each of the five cases are presented in table 5.5. The Sutherland law was used to determine the viscosity of the air flow. With the Reynolds number, it was possible to estimate the compressible laminar boundary layer thickness using the similarity solution of Cohen (1956) . The exit diameter of the injector is also given so that the ratio δ/d could be evaluated. This parameter is important if penetration height needs to be estimated. Finally, velocity ratio, mass flux ratio, and dynamic pressure ratio are tabulated for each case. All these values pertain to the tests where hydrogen is injected into air.

Case	1	2	3	4	5
Reynolds Number ($\times 10^{-6}$)	1.3	0.65	0.95	0.82	0.85
δ (mm)	2.0	2.9	2.4	2.6	2.5
Exit Diameter of Injector (mm)	6.20	6.20	6.20	6.25	6.25
δ / d	0.32	0.47	0.39	0.42	0.40
v_{jet} / v_{flow}	0.91	0.75	0.75	0.88	1.01
$(\rho v)_{jet} / (\rho v)_{flow}$	0.98	3.11	1.56	1.15	0.37
$(\rho v^2)_{jet} / (\rho v^2)_{flow}$	0.89	2.33	1.17	1.01	0.37

Table 5.5 Some nondimensional numbers for hydrogen injection into air.

5.5 Experimental Results

Results of each of the three diagnostic techniques used will be discussed separately. Heat transfer measurements on the surface of the plate will be presented first, followed by the pressure measurements, and the differential interferometry pictures of the flow.

5.5.1 Heat Transfer Rate Measurements

Figure 5.2 shows the heat transfer rate for three experiments with hydrogen injection in the high pressure-low enthalpy case. The heat transfer rate is up to 50% higher when the experiments are done in air instead of nitrogen. These experiments did not show if the difference is due to combustion or simply because of the differences in the heat transfer rate with the wall for the air flow compared to the nitrogen one.

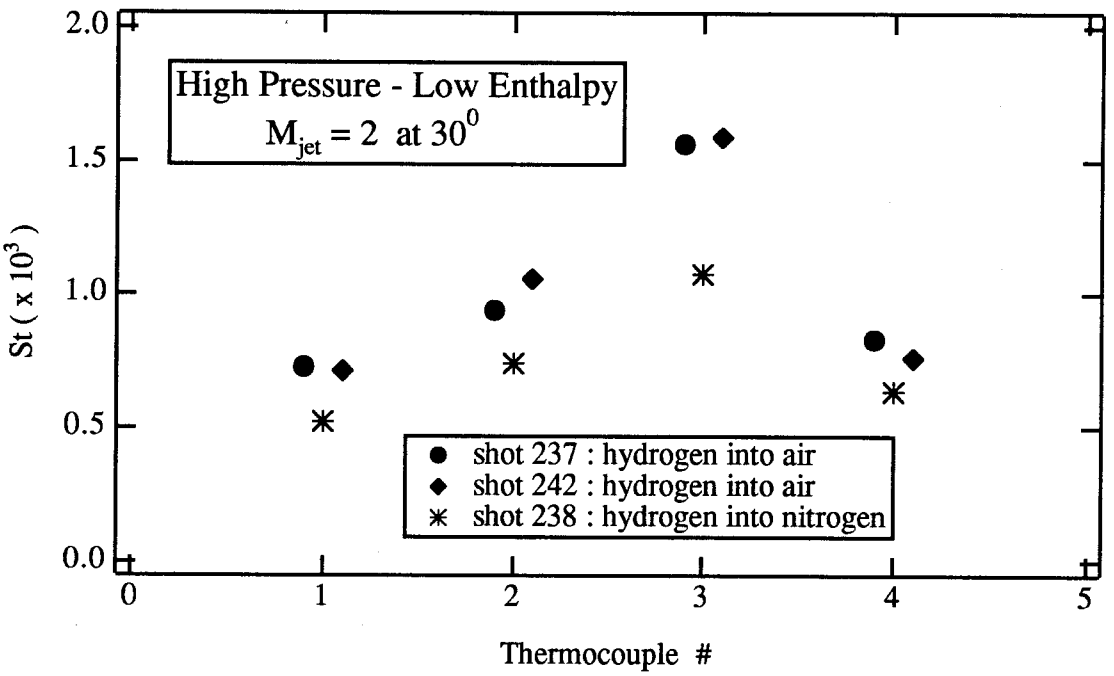

Figure 5.2 Heat flux rate for hydrogen injection in the high pressure-low enthalpy case.

The same tests were done using helium as the injected gas. The results are shown in figure 5.3. The same increase in heat transfer rate between the air flow and the nitrogen flow appears to have occurred. Figures 5.2 and 5.3 also show the very good repeatability of the heat transfer measurements for these experiments. The difference in the heat transfer rate between the air and nitrogen flows is believed to be caused by oxygen recombination in the boundary layer of the air flow. By increasing the temperature of the boundary layer, this recombination increases the heat flux to the wall. Measurements of boundary layer heat transfer rate in T5 by Germain et al. (1993) have shown the same results.

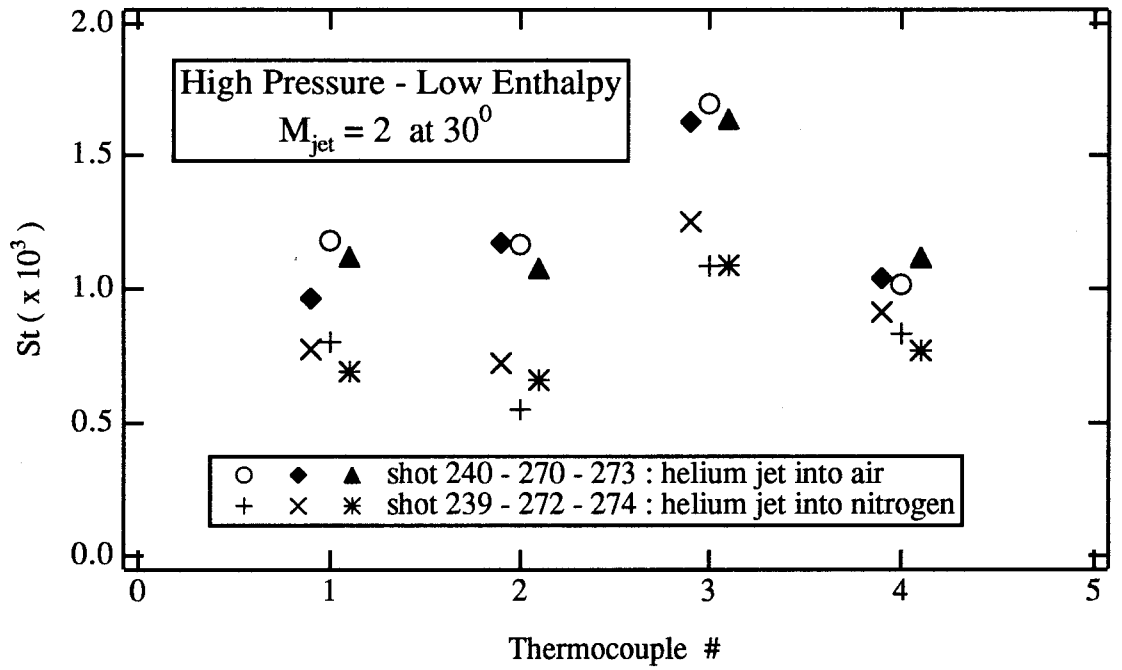

Figure 5.3 Heat flux rate for helium injection in the high pressure-low enthalpy case.

To determine if there was combustion in the boundary layer of the hydrogen-air test, the Stanton number ratios between the air flow and the nitrogen flow in the hydrogen experiments were compared to the same ratios in the helium injection tests. These ratios are presented in figure 5.4. According to this figure the hydrogen jet did not produce more heating at the surface of the plate than the helium jet did, and no detectable combustion occurred in the boundary layer for this high pressure-low enthalpy case.

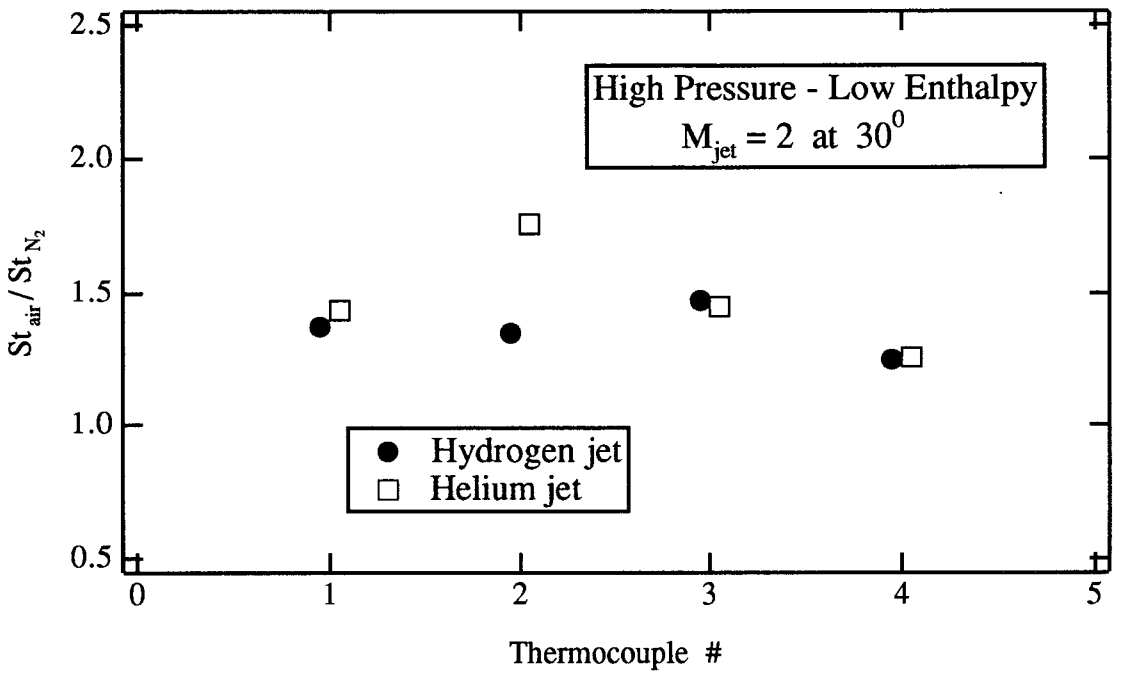

Figure 5.4 Heat flux ratio between air and nitrogen flows with hydrogen or helium injection in the high pressure-low enthalpy case.

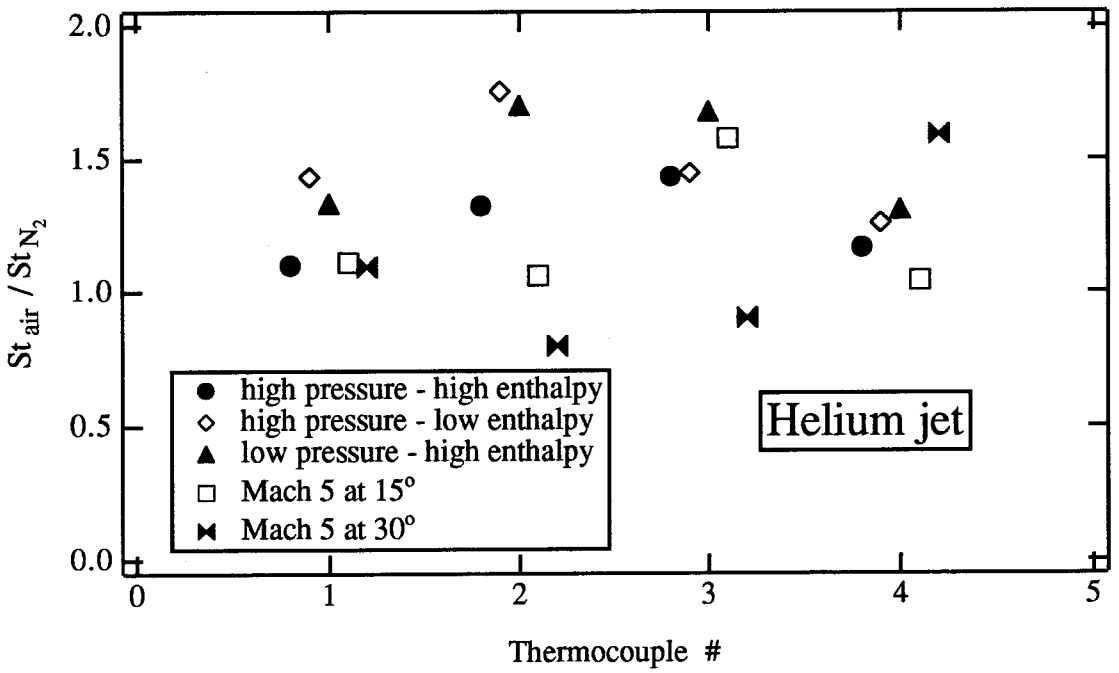

Figure 5.5 Heat flux ratio between air and nitrogen flows for helium injection in the five cases studied.

The low pressure-high enthalpy case was by far tested the most and was used to test repeatability. The four other cases were not tested as extensively and, as a result, it is very difficult to determine an error bar for these experiments. Some of these cases have only one successful experiment per condition.

The only guideline that can be used to determine if some combustion occurred is to look at the Stanton number ratio for helium injection in the five cases studied and define a maximum Stanton number ratio for the non-combustion cases. If this ratio is exceeded during a combustion test, it would indicate that some combustion really occurred in the flow. These five cases with helium injection are shown in figure 5.5.

According to figure 5.5, the Stanton number ratio for the non-combustion tests never exceeds 1.7. This general criterion will be used as a guideline for the four other cases. Applied to the first case, the same conclusion is reached as before; there is no detectable combustion in the boundary layer of the low pressure-high enthalpy case.

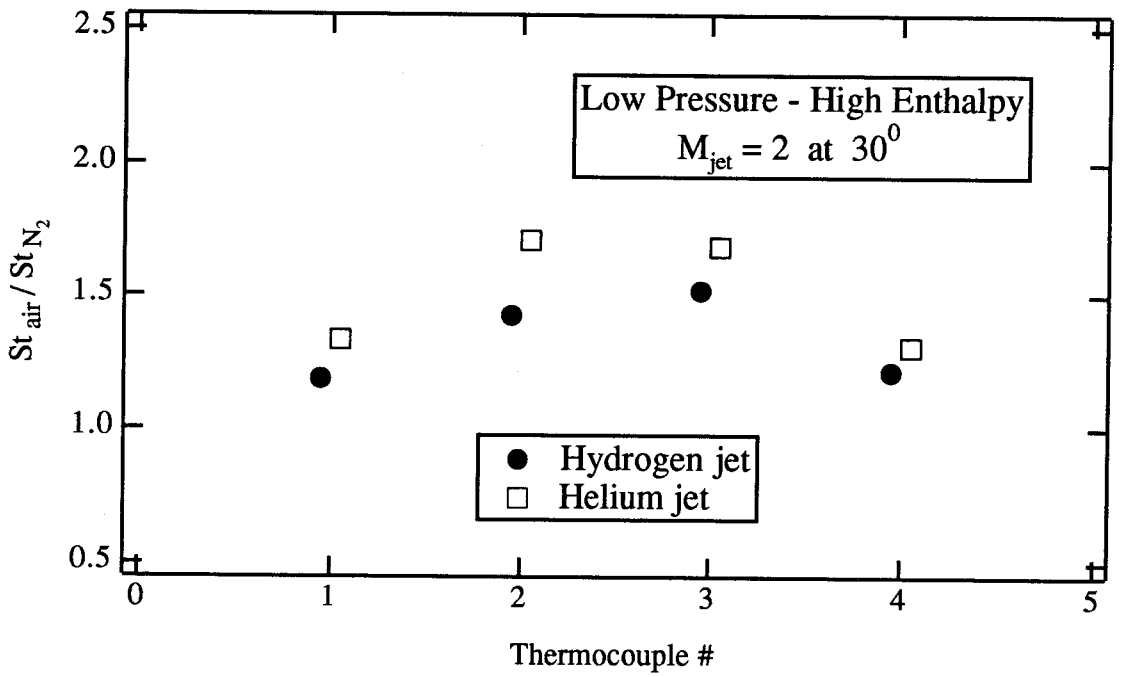

Figure 5.6 Heat flux ratio between air and nitrogen flows with hydrogen or helium injection in the low pressure-high enthalpy case.

The next case is the low pressure-high enthalpy one. Here again no detectable combustion can be seen comparing helium and hydrogen injection in figure 5.6. The Stanton number ratio also never exceeds 1.5 for the hydrogen experiments, supporting the conclusion that combustion was very limited.

Figures 5.7, 5.8 and 5.9 show the results for the last three cases with high pressure-high enthalpy flows and with different injection nozzles. In all three cases, Stanton number ratios over 2 were measured for the hydrogen injection. It is believed that detectable combustion has occurred in the boundary layer for the three cases.

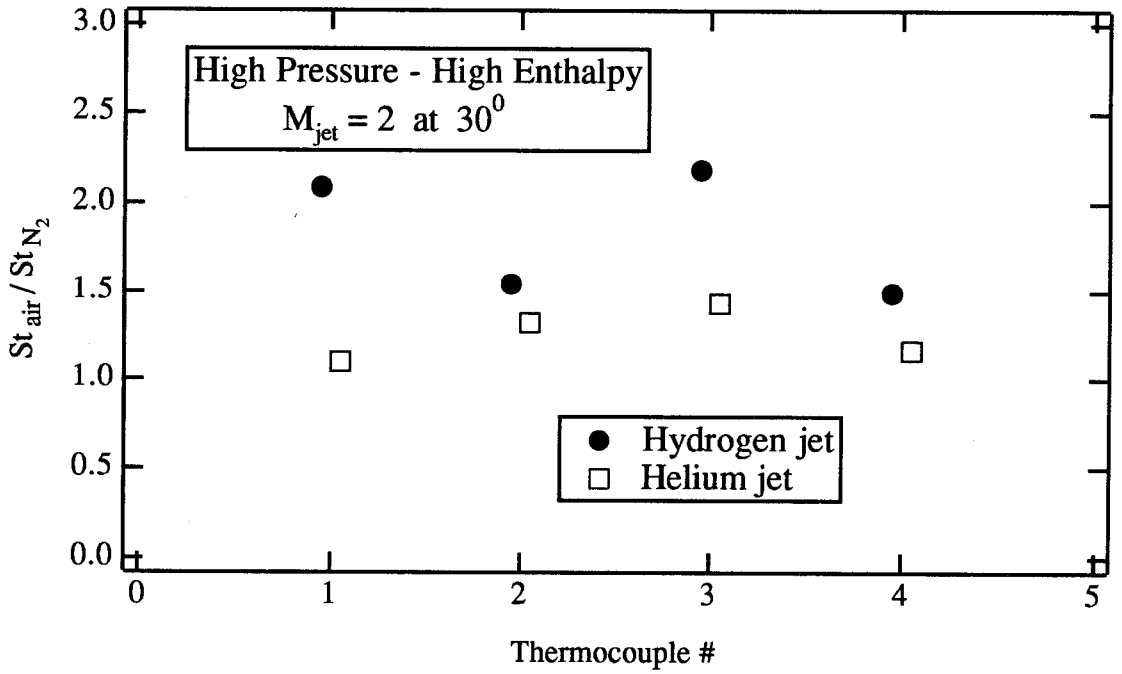

Figure 5.7 Heat flux ratio between air and nitrogen flows with hydrogen or helium injection in the high pressure-high enthalpy case.

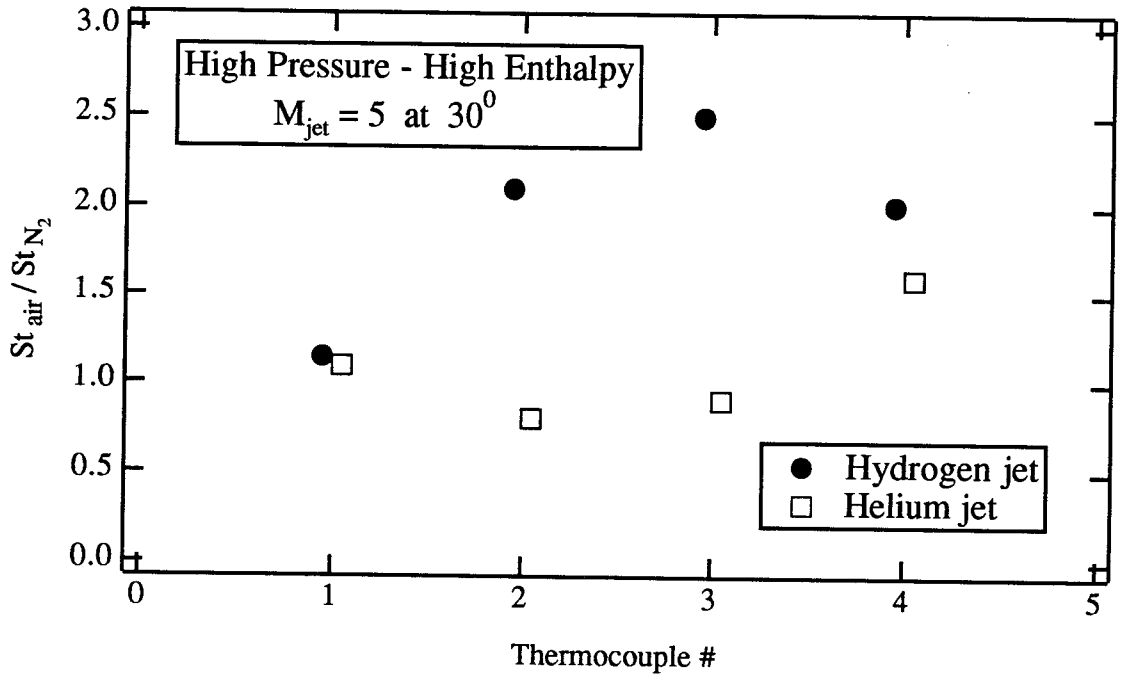

Figure 5.8 Heat flux ratio between air and nitrogen flows with hydrogen or helium injection in the high pressure-high enthalpy Mach 5, 30° case.

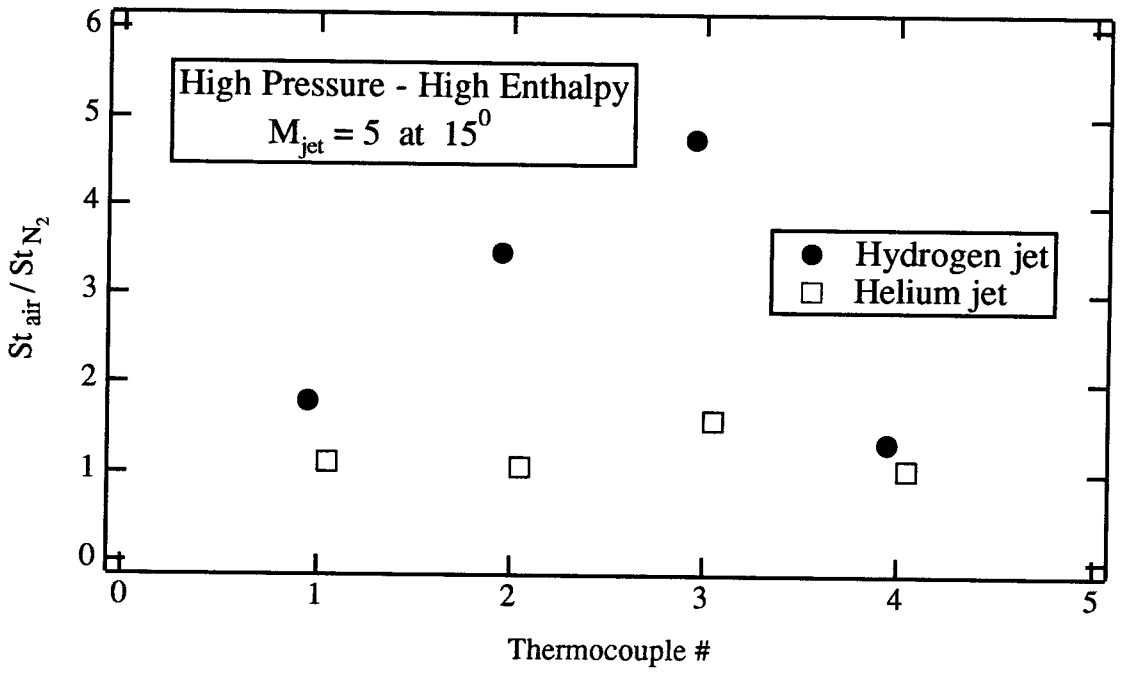

Figure 5.9 Heat flux ratio between air and nitrogen flows with hydrogen or helium injection in the high pressure-high enthalpy Mach 5, 15° case.

The very large Stanton number ratios measured with the Mach 5, 15° injector are probably due to the fact that a large amount of cold jet gas stays in the boundary layer in this case, making the boundary layer much colder. In the non-combustion tests, the cold boundary layer reduced the measured Stanton number significantly while in the combustion tests, the heat release from the combustion largely compensate for the colder boundary layer.

The only cases where detectable combustion occurs in the recirculating region in front of the jet and in the boundary layer downstream are with the high pressure-high enthalpy flows. Furthermore, the type of injector used does not have an effect on that result.

5.5.2 Pressure Measurement

As was discussed in chapter 4, the measurements from the pressure transducers are not very reliable due to a very large noise level on the data recorded. Furthermore, all the measurements with the Mach 5, 30° injection nozzle had to be discarded because of unacceptable variation of the pressure level during a test even after a strong smoothing of the data. This problem was probably related to the fact that, in that case, the total nozzle reservoir pressure of the injector was more than 14 MPa, by far the highest pressure used for this set of experiments. The flat plate is effectively the end-wall of the combustion driven shock tunnel used to supply the injected gas. The strong shock wave and the high pressure level probably increased the vibration level of the plate to a point where the pressure transducers could no longer compensate for the large accelerations.

Figure 5.10 shows the pressure ratio between the air and nitrogen tests for the experiments with helium injection. This average pressure ratio of about 1.2 is due to a stronger real gas effect in the nozzle of T5 for the air flow. According to tables 5.1 and 5.2, a ratio of about 1.10 to 1.15 might be expected according to the free stream conditions. The measured value of the ratio of 1.2 is from pressure transducers that are behind a bow shock where stronger real gas effects occurred. Figure 5.10 shows that even with very large noise levels, the results are quite consistent.

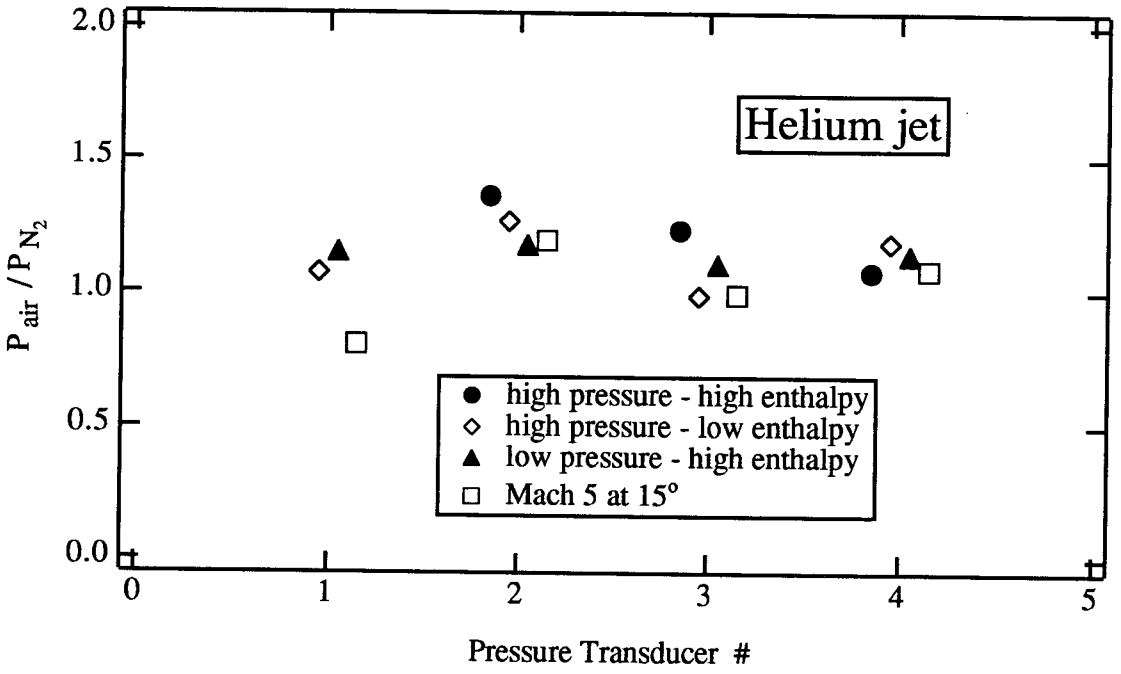

Figure 5.10 Pressure ratio between air and nitrogen flows for helium injection in four of the five cases studied.

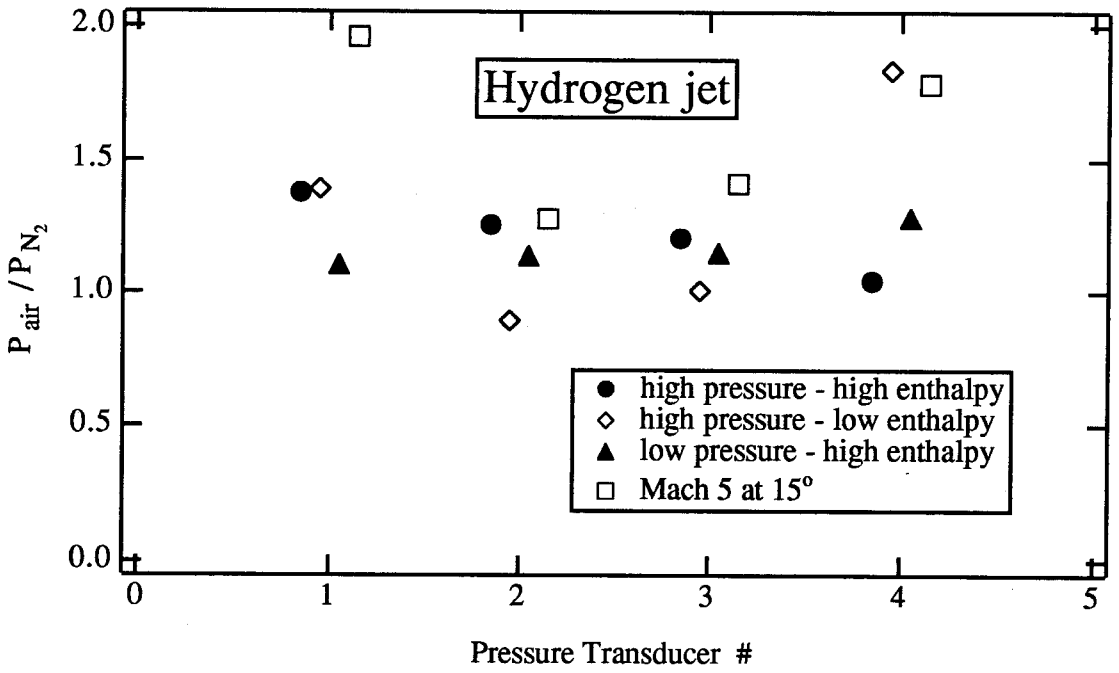

Figure 5.11 Pressure ratio between air and nitrogen flows for hydrogen injection in four of the five cases studied.

The pressure ratios for the hydrogen injections are presented in figure 5.11. For most of the cases, no significant increase in the pressure for the combustion tests was measured. Of the three data points showing an increase in the pressure ratio, two come from the Mach 5, 15° injection case where detectable combustion was measured by the thermocouples. The third data point comes from the pressure transducer no. 4 in the high pressure-low enthalpy case. If this point, indicating some combustion, was supported by an increase in the heat transfer rate in that region, it could be a sign of combustion. A close look at the heat transfer ratio for thermocouple no. 4 in figure 5.4 does not support this supposition, and therefore this data point will not be considered conclusive of any significant combustion.

As can be seen, these pressure transducer measurements were not very useful in determining if any significant combustion occurred in the boundary layer. They are presented here mainly for completeness of the data taken during these tests. Furthermore, the fact that no noticeable pressure ratio increase was measured for the high pressure-high enthalpy case with the Mach 2, 30° injector does not, in the author's opinion, mean that no combustion occurred in the boundary layer for that case.

5.5.3 Differential Interferometry Measurements

Figure 5.12 shows the differential interferogram for shot no. 242 which was a high pressure-low enthalpy case with hydrogen injection into air. The bow shock is very well defined on this picture and it was possible to measure its position. The idea was to see if there was a difference in the position of the shock depending on whether it was a combustion or a non-combustion test. It is plausible that if some combustion occurs in the shear layer behind the bow shock, it may release enough energy to move the shock wave upstream.

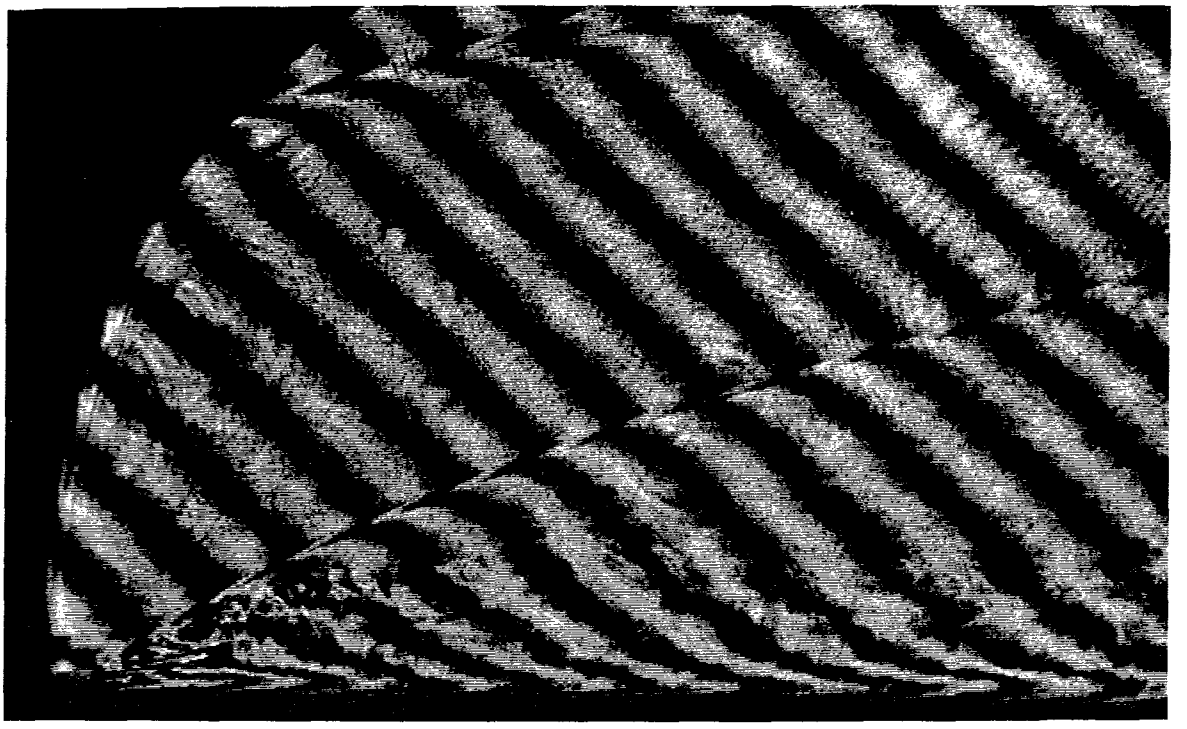

Figure 5.12 Differential interferogram for shot 242 which was a high pressure-low enthalpy case with hydrogen injection into air.

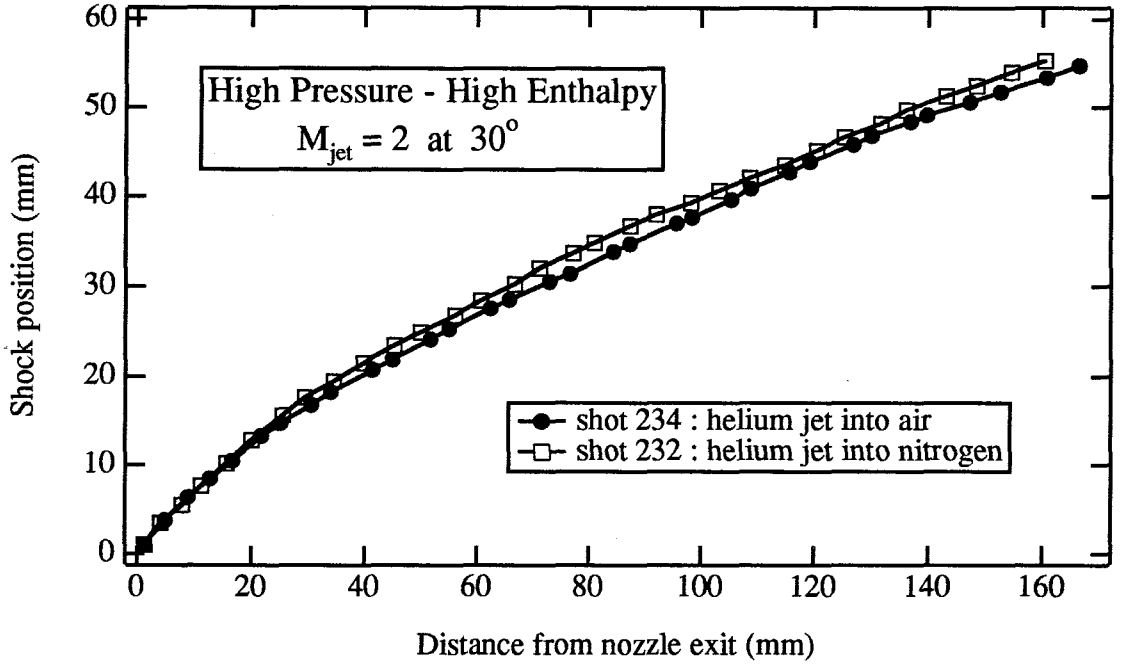

Figure 5.13 Bow shock position for the high pressure-high enthalpy case with helium injection.

To get a better idea of what we are trying to do here, consider the high pressure-high enthalpy case with the Mach 2, 30° injector. Figure 5.13 shows the position of the shock for experiments with helium injection . According to this figure, the bow shock was further away from the flat plate for the test in nitrogen. This result could be because, as we have seen earlier, the static pressure in the test section of T5 is lower for the nitrogen flow, making it easier for the jet to penetrate deeper into the flow.

The tests with hydrogen injection are shown in figure 5.14. For these experiments, the relative position is changed and, even if the static pressure is lower for the nitrogen experiments, the combustion seems to have a noticeable effect on the bow shock. A difference can be seen starting about 80 mm downstream of the injector. This difference indicates that significant combustion occurred in the bow shock region for this high pressure-high enthalpy case.

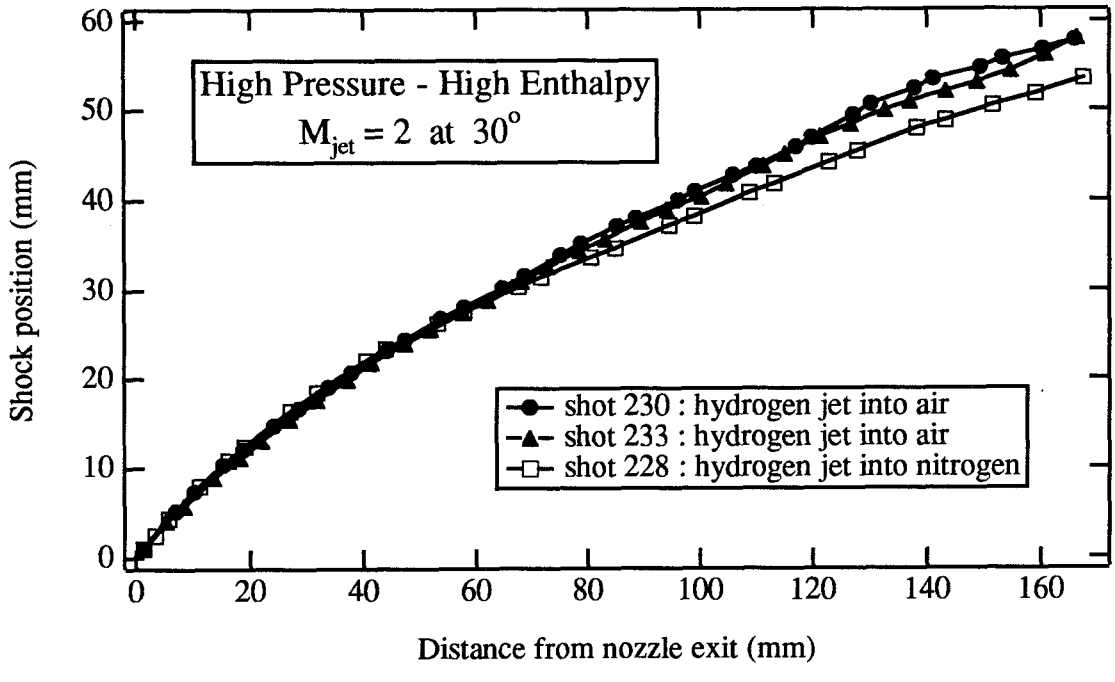

Figure 5.14 Bow shock position for the high pressure-high enthalpy case with hydrogen injection.

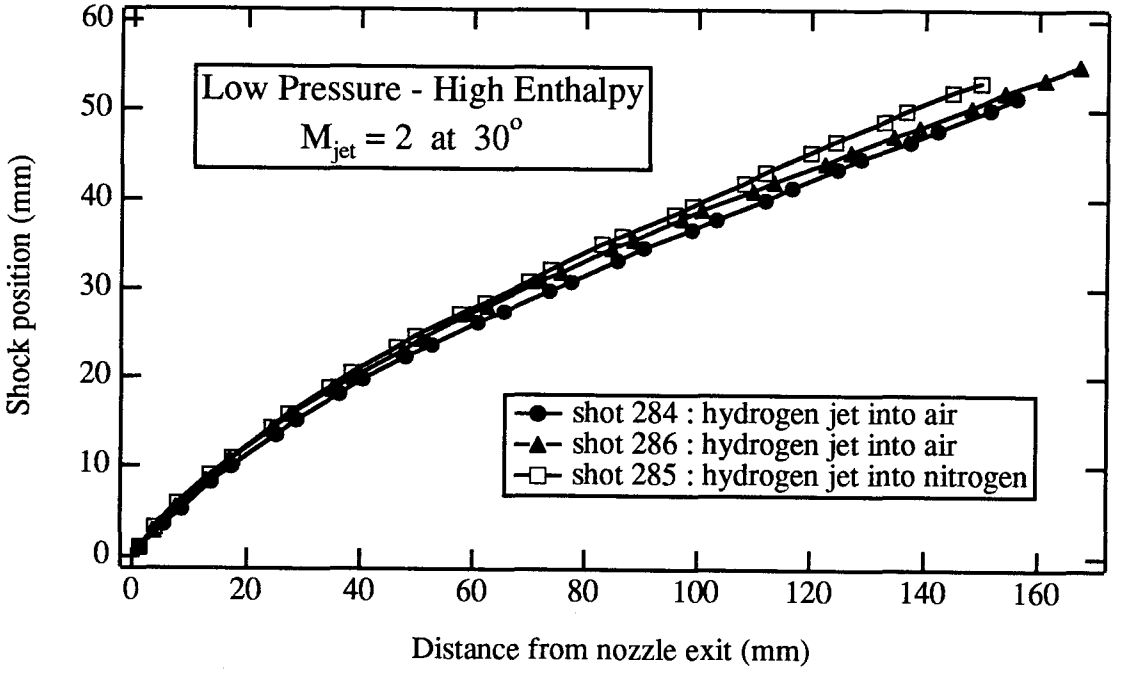

Figure 5.15 Bow shock position for the low pressure-high enthalpy case with hydrogen injection.

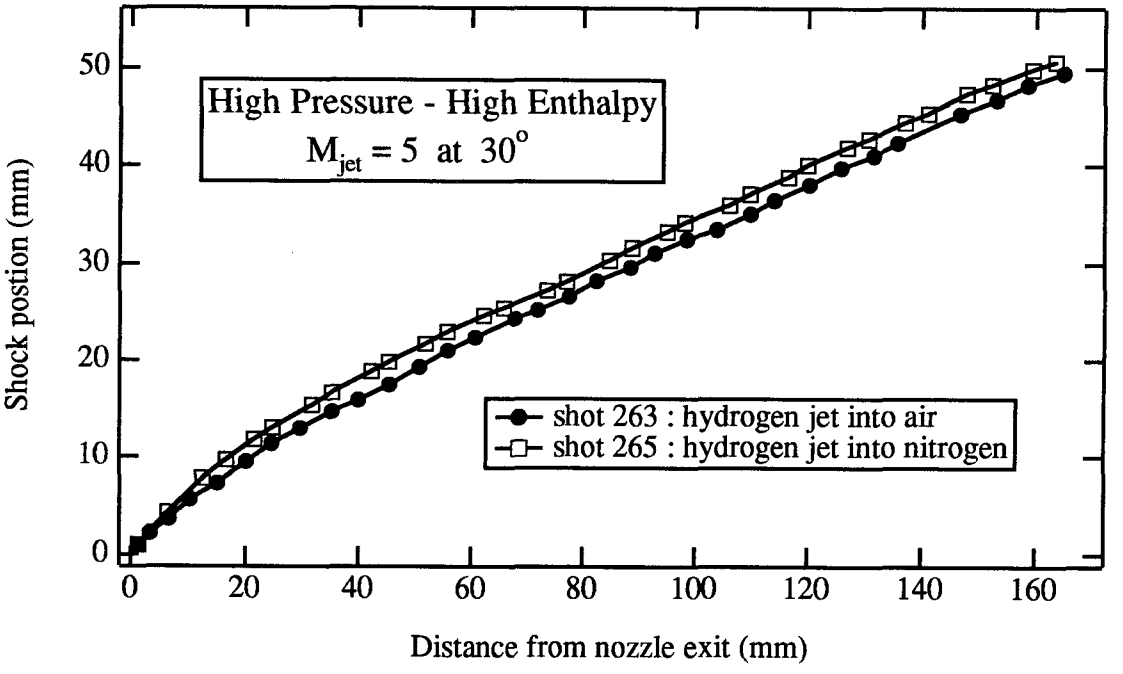

Figure 5.16 Bow shock position for the Mach 5, 30^o injector case with hydrogen injection.

The low pressure-high enthalpy case with hydrogen injection is shown in figure 5.15. The bow shock is further upstream in the nitrogen test, even though the air tests were potentially with combustion. In this case, therefore, it seems very clear that no significant combustion occurred near the bow shock.

Figure 5.16 is for the Mach 5, 30° injector case with hydrogen injection. As in the previous case, no noticeable combustion could be detected here in the bow shock region. It is possible that, because the hydrogen is much colder in this case, the combustion rate was extensively reduced although this is a high pressure-high enthalpy case.

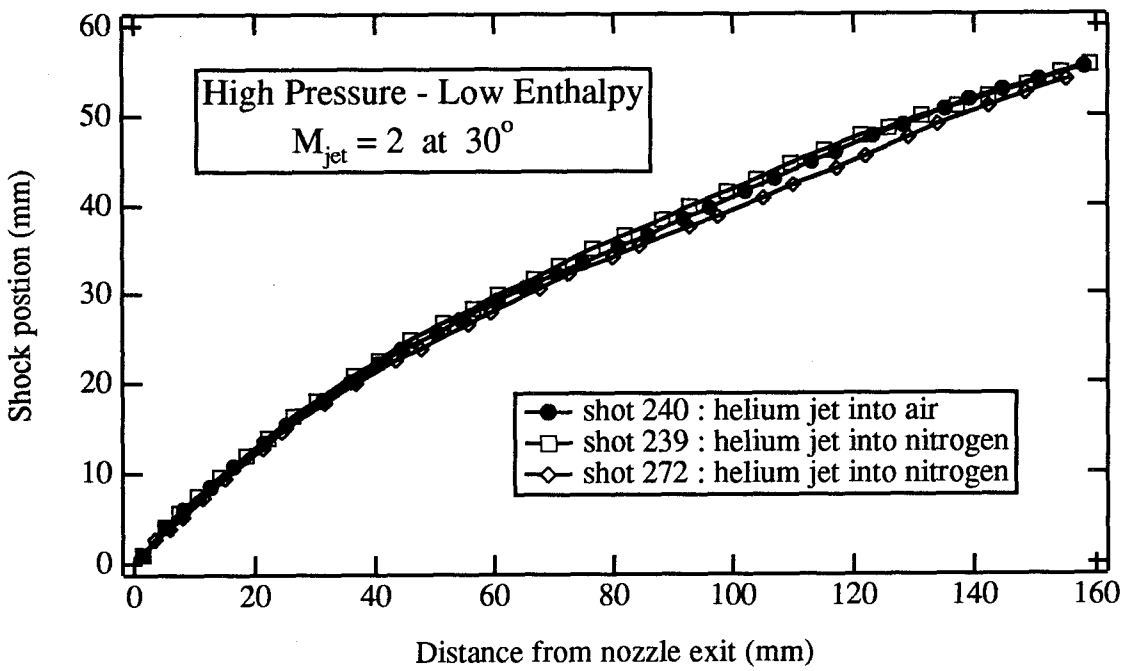

Figure 5.17 Bow shock position for the high pressure-low enthalpy case with helium injection.

The last case presented in this section is the high pressure-low enthalpy one. Although it is the case with the largest number of shots, the results are not as clear as those with the other conditions. Figure 5.17 shows the tests with helium injection and figure 5.18 those tests with hydrogen. As may be seen in figure 5.17, the difference between nitrogen and air flow for these non-combustion tests is not as significant as in the previous cases. It must be mentioned at this point that the injector reservoir pressure for

shot 272 was almost 10% lower than in the other tests, making this bow shock position questionable with respect to the others. Although this test is not taken into account, it shows that according to figure 5.17, the penetration of the helium jet is not greater in the nitrogen flow.

For the hydrogen injection presented in figure 5.18, the combustion tests seem to have moved the shock upstream. Though not as significant as for the high pressure-high enthalpy case, it looks like at least some combustion occurred in the bow shock region.

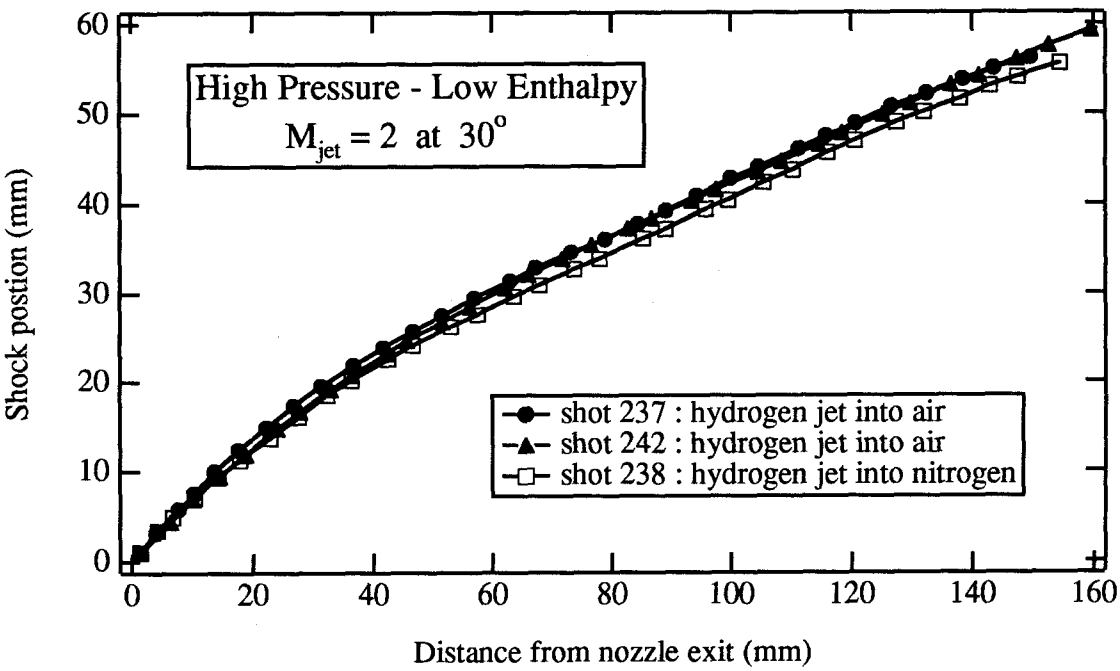

Figure 5.18 Bow shock position for the high pressure-low enthalpy case with hydrogen injection.

The Mach 5, 15° injector case could not be studied with this technique because the bow shock was much weaker, making it very difficult to define the exact position of the shock.

The only cases where some combustion occurred in the bow shock region are the high pressure-high enthalpy case and probably the high pressure-low enthalpy cases.

5.6 Conclusion

In this chapter the terms "detectable" or "significant" combustion are used to define cases where the instrumentation has detected a significant difference between a combustion and a non-combustion test. With the instrumentation used during these experiments, it is not possible to go further and attempt to quantify the amount of combustion. Techniques like Planar Laser Induced Fluorescence (PLIF) may one day be the tools used to answer some of these questions. But for now the PLIF technique must mature if quantitative measurement in very difficult environments such as that in the test section of T5 are to be performed. Efforts to get such a PLIF system for these tests, even for qualitative measurements, through the NASP program, Rocketdyne, and NASA Langley were not successful.

Table 5.6 gives a overall view of the results presented in this chapter. For each of the five cases and for the two regions where combustion could occur, the question asked is: was there any significant combustion in that region?

	Boundary layer	Bow shock
High pressure-low enthalpy	no	yes
Low pressure-high enthalpy	no	no
High pressure-high enthalpy	yes	yes
Mach 5 at 30° injector	yes	no
Mach 5 at 15° injector	yes	n.a.

Table 5.6 For the five cases studied, signs of significant combustion in the boundary layer and the bow shock region.

In the boundary layer, only the cases with high pressure and high enthalpy gave signs of combustion. In the bow shock region, the hot injection (Mach 2) in the high pressure-high enthalpy case also gave signs of combustion, but the cold injection (Mach 5) did not. The high pressure-low enthalpy case is not as clear, but some combustion seems to have occurred in the bow shock region.

It is important at this point to make the following comments. There are quite a few research groups around the world that have detected combustion at a much lower pressure in hypersonic facilities than the threshold observed here. The fundamental difference between the present experiments and the others is that the fuel here is injected at over 3600 m/s, making the time residency of the fuel over the instrumented part of the model less than 50 μs. It appears that this time is too short for significant combustion in some of the conditions tested. Since the size of the real air-breathing engine is considerably larger, the residence time will be increased correspondingly and may improve the ability of the flow to burn the hydrogen.

Chapter 6
Combustor Experiments

6.1 Introduction

The tests presented in this chapter were performed in a 50.8 mm by 25.4 mm cross section combustor model previously tested in the HYPULSE expansion tube facility at the General Applied Science Laboratories in Ronkonkoma, New York. One of the objectives of these experiments was to compare our results with those of identical tests previously made in the expansion tube. Because of the presence of dissociated oxygen and NO in the flow of free piston shock tunnels, it is possible that combustion experiments may not reproduce results obtained in "clean" air flows. The HYPULSE expansion tube does not have that problem because the high stagnation enthalpy flow is never actually stopped and therefore the molecules of O_2 and N_2 do not dissociate. The disadvantages of these facilities are their much shorter test time and smaller size.

All the experiments done in HYPULSE used a cold hydrogen injection system. To reproduce that part of the flow, the combustion driven shock tunnel was converted for some of the tests into a Ludwieg tube with which the fuel could be supplied to the injector without increasing its temperature. It was then possible to compare experiments with cold and hot hydrogen injection. A description of changes needed to convert the combustion driven shock tunnel into a Ludwieg tube is presented in section 6.1. No tests with helium injection were done in this set of experiments.

Another important goal of these experiments was to test this combustor at much higher static pressure. T5 can supply test gas with static pressure around 40 kPa, 2.5 times the maximum static pressure in the test section of HYPULSE. Because the combustion process is mostly a three-body reaction, this higher pressure can result in reaction rates

increased by a factor of 6, significantly improving the chance of detecting the combustion. This higher static pressure is also more representative of a real flying propulsion system where the static pressure would be about 50 kPa for the range of total enthalpy used here. These test results will also be used for comparison with a new set of numerical simulations underway at NASA Langley with the SPARK CFD code. Pressure transducer measurements and flow visualization pictures will be used in this comparison.

Previous results of experiments done in HYPULSE with this combustor were presented by Bakos et al. (1992a) for test conditions that will be reproduced here. They also published results for a set of experiments at lower enthalpy (see Bakos et al., 1992b). At the same time, there has been an important effort to make a computational investigation of these flows. Bobskill et al. (1991), Riggins and McClinton (1992a), and Riggins et al. (1992b) present some of these results.

The question of the effects of dissociated oxygen and NO_x in combustion experiments has been examined recently by Jachimowski (1992) and by Bakos and Morgan (1992c) in the case of dissociated oxygen and by Laster and Sojka (1989) for the NO_x.

The test model and the conversion of the combustion driven shock tunnel into a Ludwieg tube are discussed in section 6.2. The test conditions used for the experiments are presented in section 6.3. All the results are then shown in section 6.4 followed by a brief conclusion in section 6.5.

6.2 Test Model

The combustor has a cross section of 50.8 mm by 25.4 mm and is 711 mm long. Optical windows in the model side walls permit flow visualization extending from 83 mm to 387 mm from the inlet of the combustor. The only injector used during these tests was a Mach 1.7, flush-mounted nozzle injecting at an angle of 15° relative to the main flow. The injector nozzle is conical with an half angle of 1.25° and exits into the combustor 177 mm downstream of the inlet from the lower wall. The injector was mounted on the upper

wall for the HYPULSE tests. Therefore, to reduce the confusion to a minimum, from now on, only the terms injector wall and opposite wall will be used.

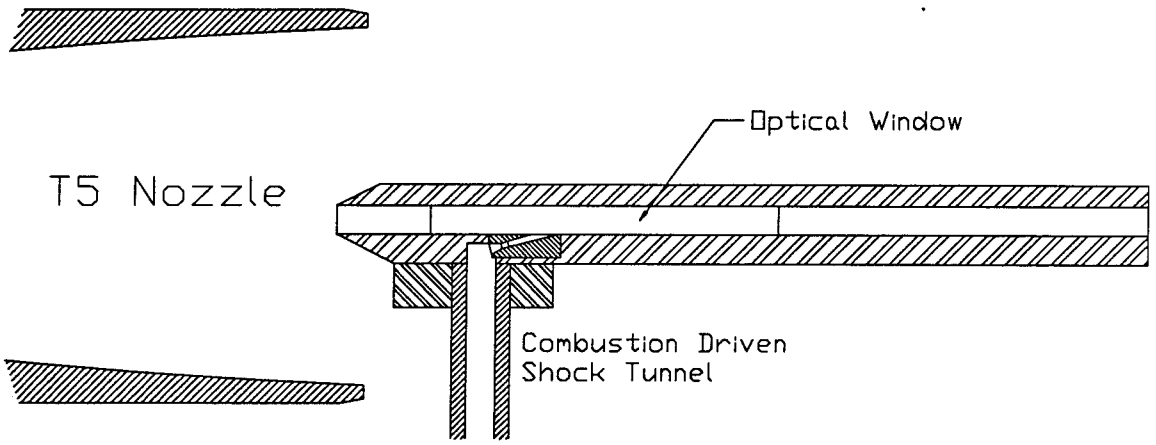

Figure 6.1 Sketch of the combustor and the combustion driven shock tunnel with respect to the exit nozzle of T5.

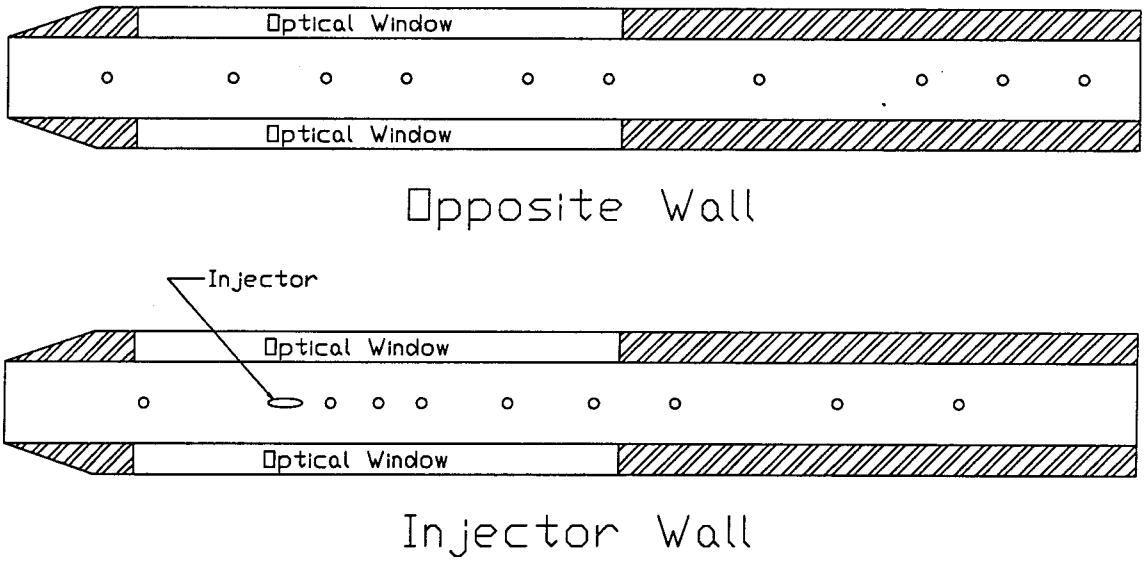

Figure 6.2 Sketch of the opposite wall and the injector wall of the combustor with the injector position, pressure transducers and optical window locations.

Figure 6.1 gives a general view of the combustor and the combustion driven shock tunnel inside the test section of T5. Figure 6.2 shows the relative position of the injector and the location of all the pressure transducers on both walls; the location of the optical windows is also shown. In all, nine pressure transducers are mounted on the centerline of the injector wall and ten on the centerline of the opposite wall. Their exact position in mm from the inlet of the combustor is shown in table 6.1.

Pressure Transducer no.	1	2	3	4	5
Injector Wall	89	206	236	263	318
Opposite Wall	63.5	144	201	252	328
Pressure Transducer no.	6	7	8	9	10
Injector Wall	372	422	524	600	-
Opposite Wall	379	473	575	626	676

Table 6.1 Position in mm from the inlet of the combustor of the 19 pressure transducers.

The combustion driven shock tunnel was converted into a Ludwieg tube for the cold hydrogen injection tests. The driver section of the system was used as the actual Ludwieg tube and filled with hydrogen. The driven section was left open to the test section of T5 by omitting the secondary diaphragm at the nozzle injector, leaving the driven section under vacuum before the tests. The diaphragms used between the driver and driven sections were thin aluminum ones, with a thickness between 0.075 mm and 0.15 mm.

The diaphragm bursting system was used to break the main diaphragm about 3 ms before the actual test time. During these 3 ms, the hydrogen had time to fill the long driven section and stabilize its pressure in the area of the nozzle injector. Figure 6.3 shows the injector nozzle reservoir pressure trace. The actual test time is between $t = 0$ and $t = 0.75$ ms. The electrical noise caused by the diaphragm bursting system can be seen at $t = -2.9$ ms.

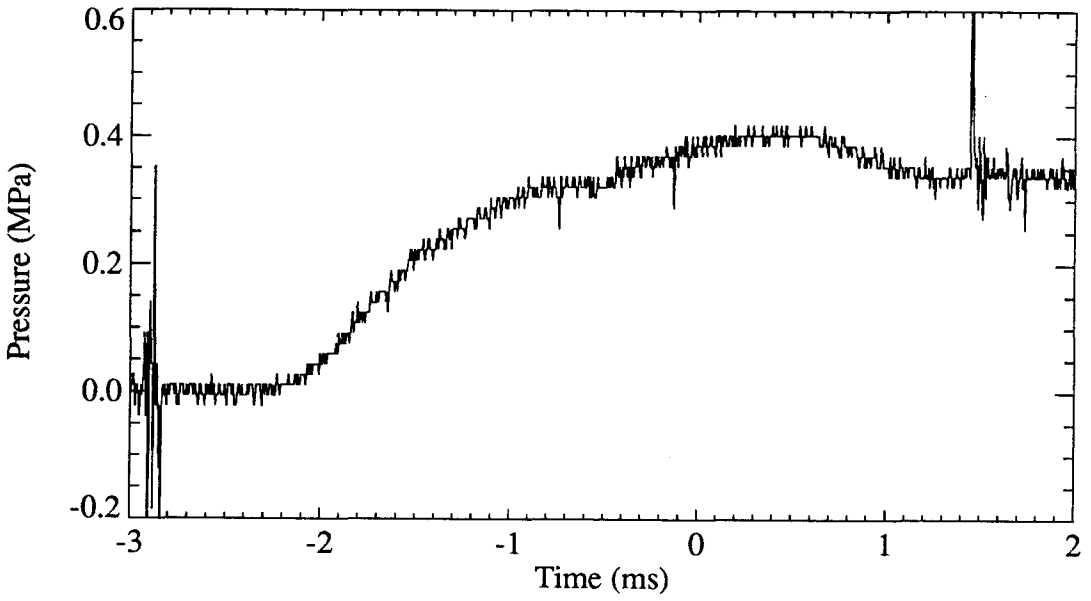

Figure 6.3 Injector nozzle reservoir pressure trace; the actual test time is between t = 0 and t = 0.75 ms.

6.3 Test Conditions

Only two different flow conditions in the test section of T5 were used for these tests. One was to reproduce the flow conditions of the HYPULSE experiments and the second one was to test a much higher pressure case. For each of these conditions, air and nitrogen were used to compare combustion and non-combustion tests. Table 6.2 presents the reservoir and test section conditions for the HYPULSE tests and the present ones for both air and nitrogen. The concentration ratio of O_2, O, and NO by mass is also presented in table 6.2 for each air flow to give an idea of the relative amount in each case.

For the low pressure case, three different fuel injection conditions were tested. The first two used cold hydrogen injection, and for these the combustion driven shock tunnel was converted into a Ludwieg tube. These conditions reproduce as closely as possible the experiments done in HYPULSE with fuel equivalence ratios of 1 and 2. The third injection condition for these low pressure tests was done with a fuel equivalence ratio of 2 but with hydrogen reservoir temperature of 1250 K.

Facility Test Gas		Hypulse air	T5 air	T5 N_2	T5 air	T5 N_2
Reservoir Conditions						
Total Pressure	(MPa)	142	37.5	37.5	85.0	85.0
Total Temperature	(K)	8350	7860	8476	8100	8875
Total Enthalpy	(MJ /kg)	15.2	15.3	15.3	15.4	15.7
Test Section Conditions						
Temperature	(K)	2090	2125	2015	2340	2210
Pressure	(kPa)	16.5	18.3	16.8	43.9	38.5
Density	(kg/m^3)	0.028	0.028	0.027	0.063	0.058
Velocity	(m/s)	5060	4785	4885	4805	5005
Mach Number		5.75	5.26	5.54	5.17	5.45
Concentration by mass						
$[O_2] / [O_2]_{air}$		0.973	0.521	-	0.672	-
$[O] / [O_2]_{air}$		0.003	0.361	-	0.201	-
$[NO] / [O_2]_{air}$		0.024	0.118	-	0.127	-

Table 6.2 Main flow conditions for the HYPULSE tests and for the two sets of experiments done in air and nitrogen with the free piston shock tunnel T5.

T5 Pressure Conditions Nominal Fuel equivalence ratio Hydrogen Injection		low 1 cold	low 2 cold	low 2 hot	high 1 hot	high 2 hot
Injection Conditions						
Total Pressure	(MPa)	0.41	0.79	1.5	2.4	4.8
Total Temperature	(K)	300	300	1250	1500	1500
Exit Pressure	(kPa)	83	160	305	485	970
Exit Temperature	(K)	190	190	790	950	950
Exit Velocity	(m/s)	1780	1780	3640	3980	3980
Actual Fuel equivalence ratio		1.0	1.9	1.8	1.1	2.2

Table 6.3 Hydrogen injection conditions for the five cases studied.

Two sets of experiments were conducted with the high pressure conditions, one with a fuel equivalence ratio of 1 and the second with a ratio of 2. Both were done with hot hydrogen at reservoir temperature of 1500 K. Table 6.3 shows the injector conditions for the three sets of experiments in the low pressure case and the two sets in the high pressure case.

6.4 Experimental Results

This section on the experimental results with the combustor model is divided into three parts. The first part presents a comparison of the low pressure cold injection tests with the previous results from the expansion tube HYPULSE. The second part discusses results from the pressure transducers inside the combustor for the five cases studied to search for evidence of combustion. The last part describes the flow visualization pictures taken during the experiments.

6.4.1 Pressure Measurement Comparison with HYPULSE

Figures 6.4 to 6.14 show comparisons of the present results with those from the expansion tube HYPULSE in the low pressure case with cold injection. First, results from the no injection tests are presented in figures 6.4 and 6.5 for air and nitrogen flows, respectively. The agreement is relatively good except for the first part of the combustor where very large pressure differences are found in the expansion tube experiments. These large pressure variations at the entrance of the combustor are due to a weak oblique shock formed in the diffuser mounted at the end of the expansion tube. The diffuser is needed for these tests to get the right flow total enthalpy.

The gradual pressure increase along the combustor is due to the growing boundary layer on its four walls. In both air and nitrogen, the total pressure increase is about 12 kPa. With a Reynolds number estimated at about 1.4×10^6 at the exit of the combustor, the boundary layer is believed to be laminar most of the way. The small variations of the pressure level from one location to the next are probably due to a calibration problem of the pressure transducers.

The set of experiments with the fuel equivalence ratio of 1 is compared with the HYPULSE tests in figures 6.6 to 6.9, figures 6.6 and 6.7 showing the results for the two different gases on the injector wall and figures 6.8 and 6.9 for the results on the opposite wall. In the same way, the sets of experiments for the fuel equivalence ratio of 2 are compared in figures 6.10 to 6.13.

All the pressure measurements presented in this section are nondimensionalized by the inlet pressure. For HYPULSE, this inlet pressure is the exit static pressure of the expansion tube and, for the present work, it is the average pressure of the two front pressure transducers. The first pressure transducer is 89 mm from the inlet on the injector wall and the second transducer is 63.5 mm from the inlet on the opposite wall.

The results show excellent agreement between the present experiments and those done in the expansion tube HYPULSE. The location of the bow shock multiple reflections was very well reproduced in the experiments. The overall pressure level was also well reproduced, except, once again, for some of the high pressure measurements in the first part of the combustor in the HYPULSE tests caused by the weak oblique shock coming from the diffuser.

It is particularly interesting to study the case with a fuel equivalence ratio of 2 from figures 6.10 to 6.13. The impingement of the incident bow shock on the opposite wall (fig. 6.12 and 6.13) at a distance of 250 mm from the inlet is extremely well reproduced for these tests, as well as the first reflection of the shock on the injector wall at a distance of 375 mm from the inlet (fig. 6.10 and 6.11). The large pressure levels measured on both walls between 500 and 600 mm from the inlet are believed to be caused by a side wall reflection of the bow shock.

Comparing the results from the two facilities, there is no sign of the effects of the presence of large quantities of dissociated oxygen and NO in the present set of experiments; although, in these tests, more than 1/3 of the oxygen was in the dissociated form and 2.5% of the test gas by volume was NO.

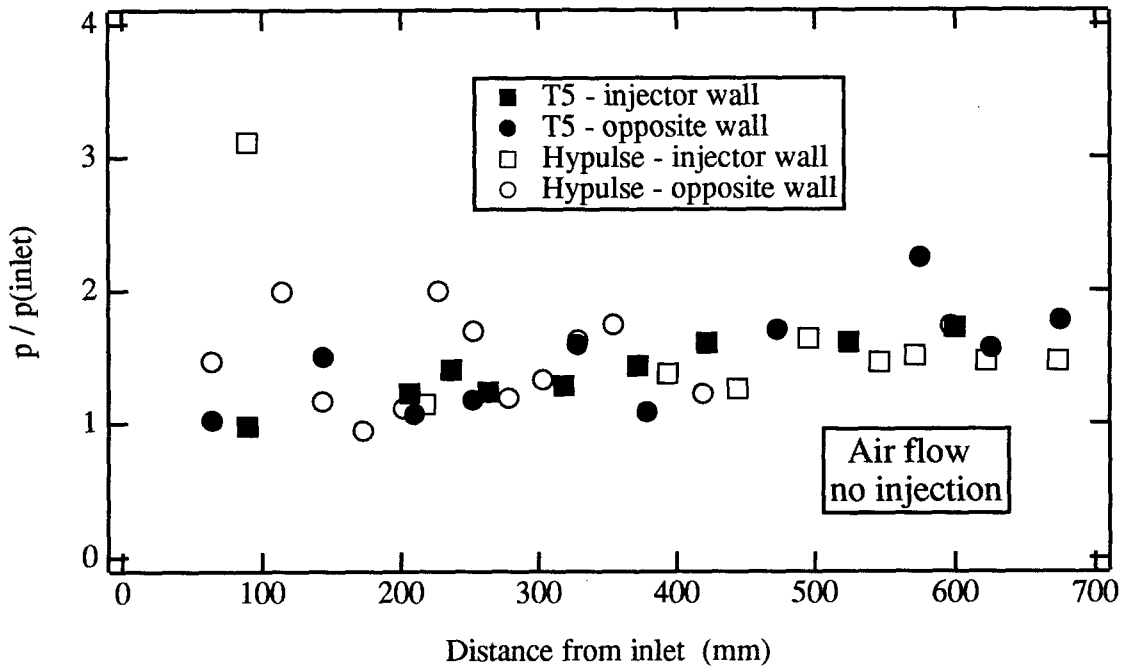

Figure 6.4 Pressure along the centerline of the injector wall and opposite wall for the low pressure, no injection case in air. The plot compares results from the expansion tube HYPULSE and the present work.

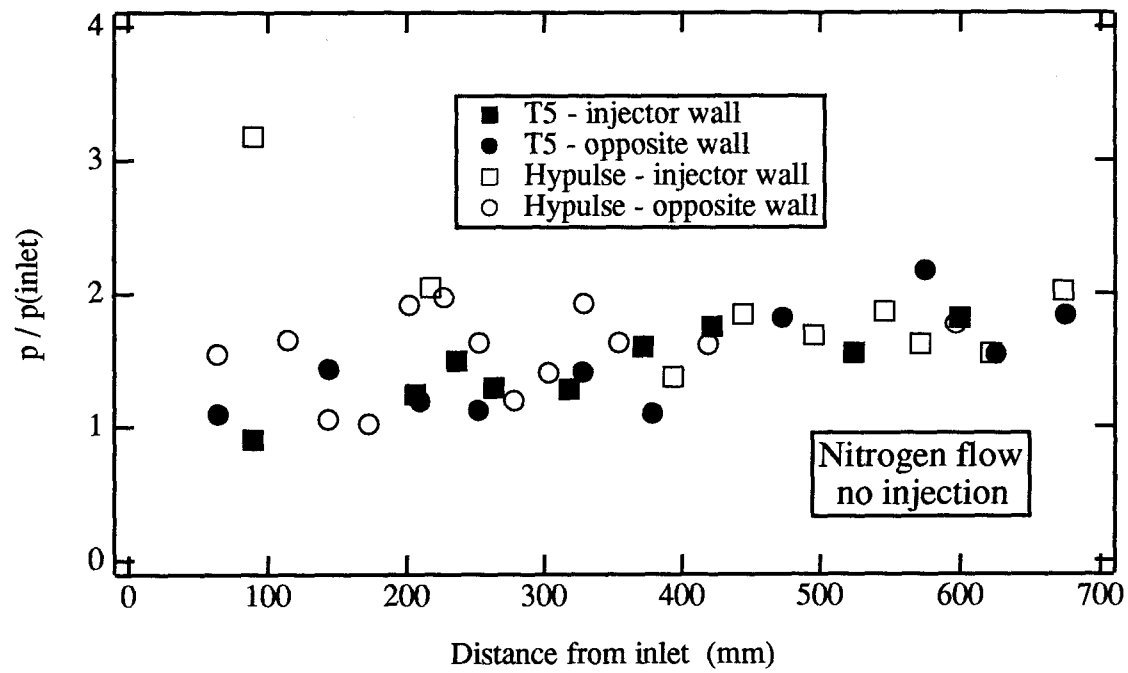

Figure 6.5 Pressure along the centerline of the injector wall and opposite wall for the low pressure, no injection case in nitrogen. The plot compares results from the expansion tube HYPULSE and the present work.

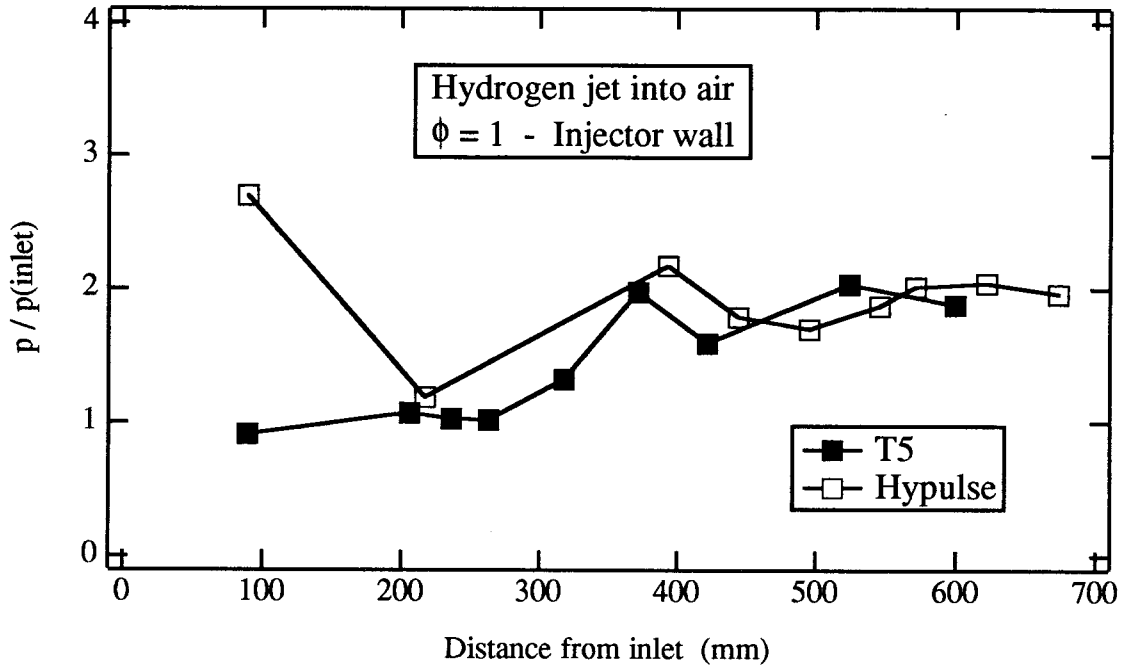

Figure 6.6 Pressure measurements on the injector wall for the low pressure case in air with a fuel equivalence ratio of 1. The plot compares results from HYPULSE and the present work. The injector is 177 mm from the inlet.

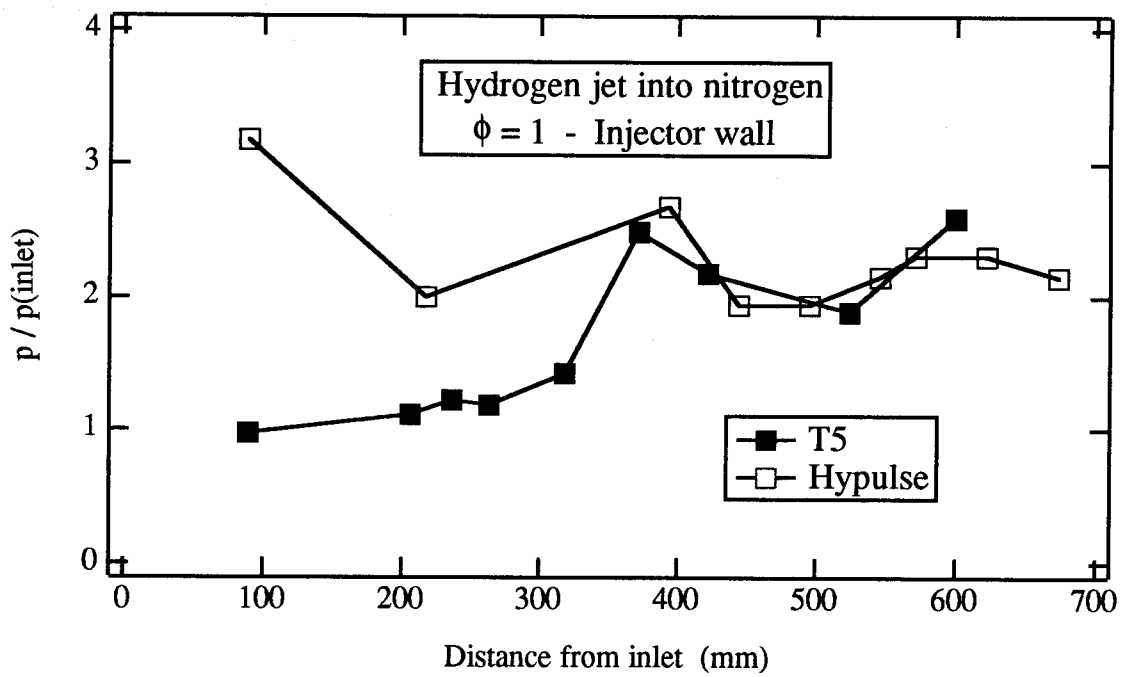

Figure 6.7 Pressure measurements on the injector wall for the low pressure case in nitrogen with a fuel equivalence ratio of 1. The plot compares results from HYPULSE and the present work. The injector is 177 mm from the inlet.

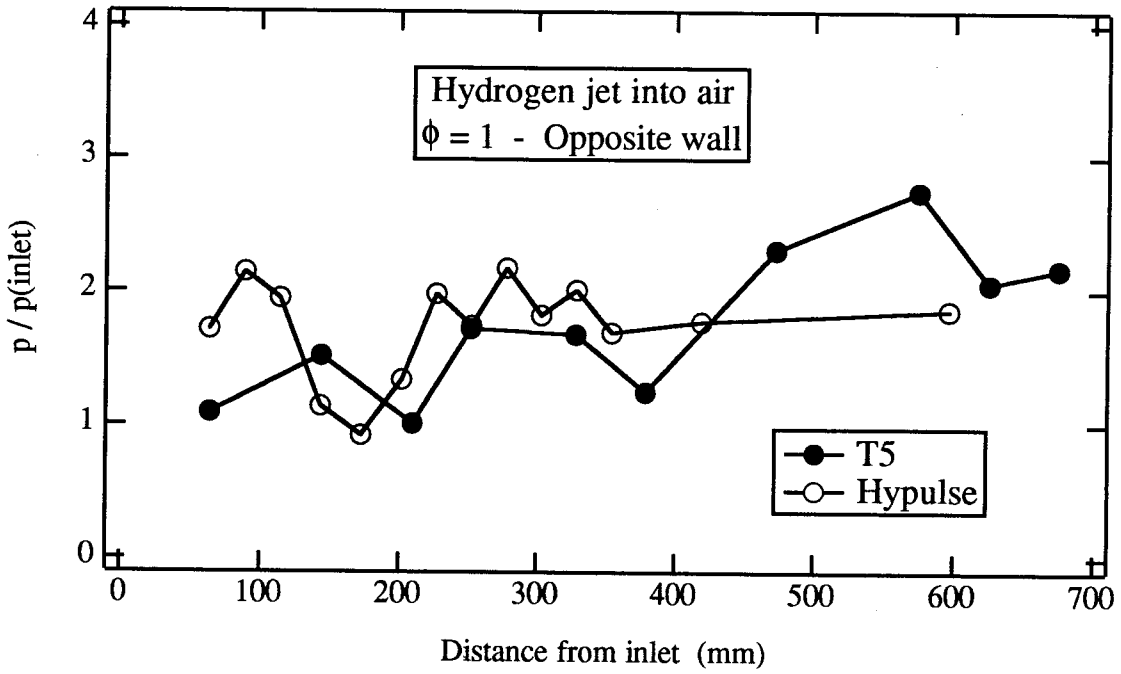

Figure 6.8 Pressure measurements on the opposite wall for the low pressure case in air with a fuel equivalence ratio of 1. The plot compares results from HYPULSE and the present work. The injector is 177 mm from the inlet.

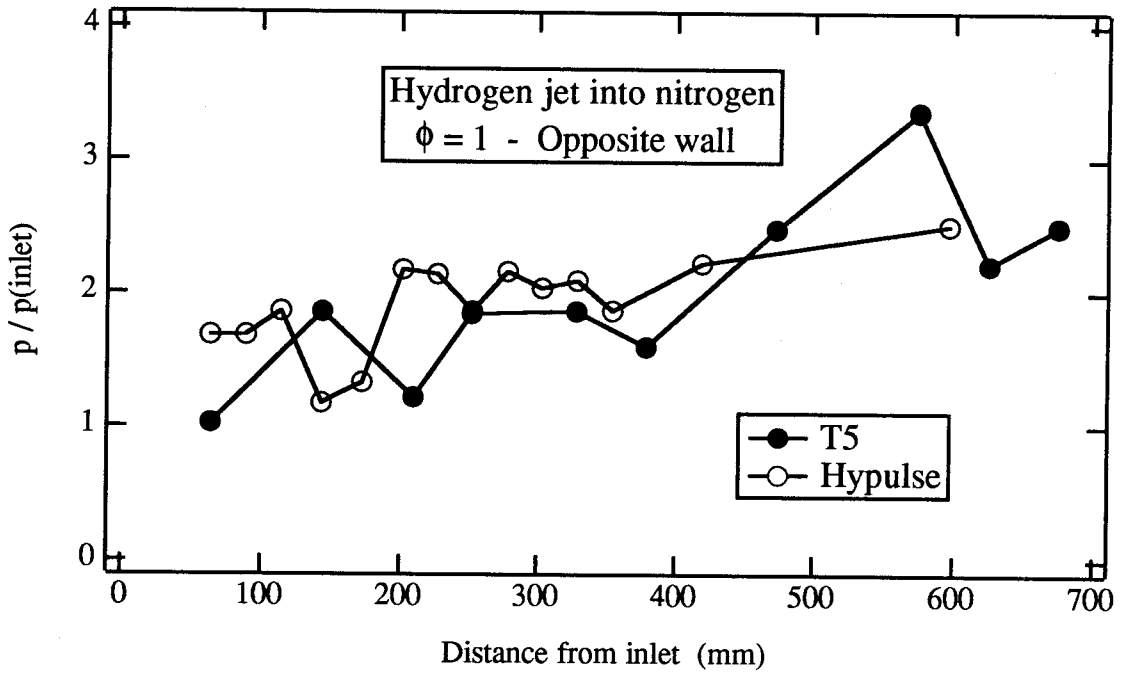

Figure 6.9 Pressure measurements on the opposite wall for the low pressure case in nitrogen with a fuel equivalence ratio of 1. The plot compares results from HYPULSE and the present work. The injector is 177 mm from the inlet.

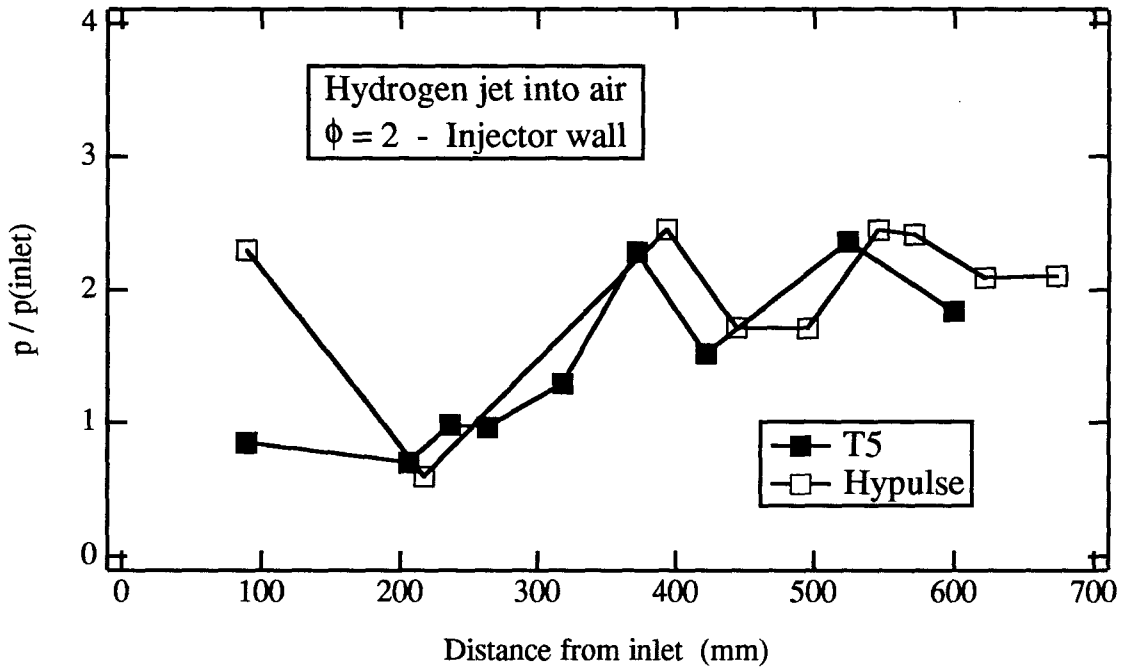

Figure 6.10 Pressure measurements on the injector wall for the low pressure case in air with a fuel equivalence ratio of 2. The plot compares results from HYPULSE and the present work. The injector is 177 mm from the inlet.

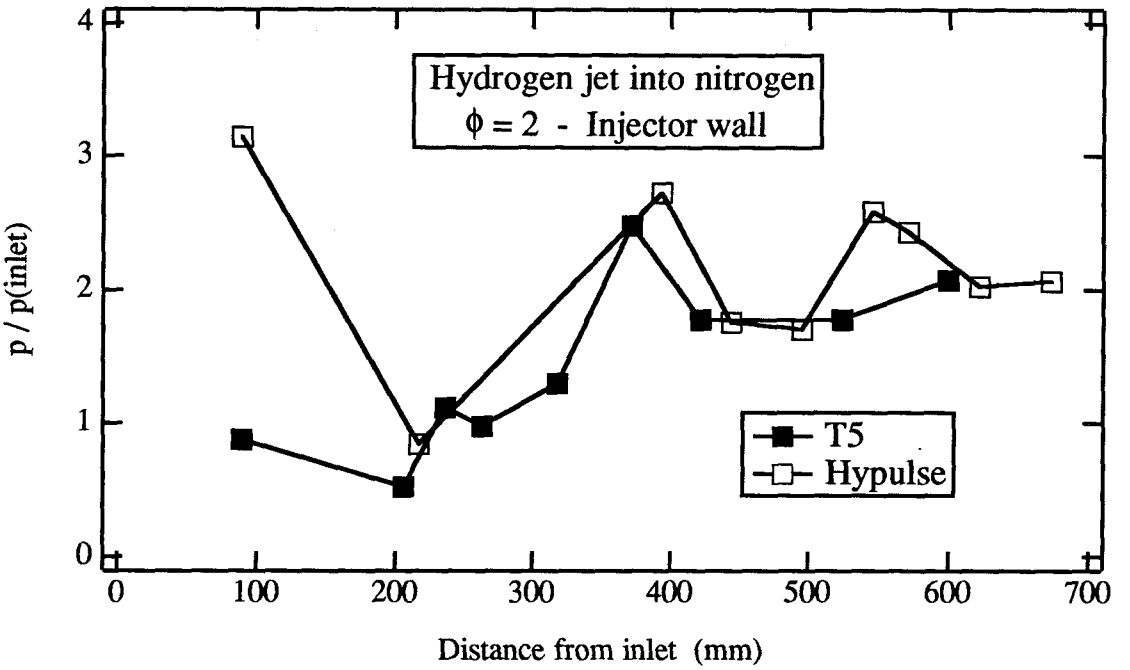

Figure 6.11 Pressure measurements on the injector wall for the low pressure case in nitrogen with a fuel equivalence ratio of 2. The plot compares results from HYPULSE and the present work. The injector is 177 mm from the inlet.

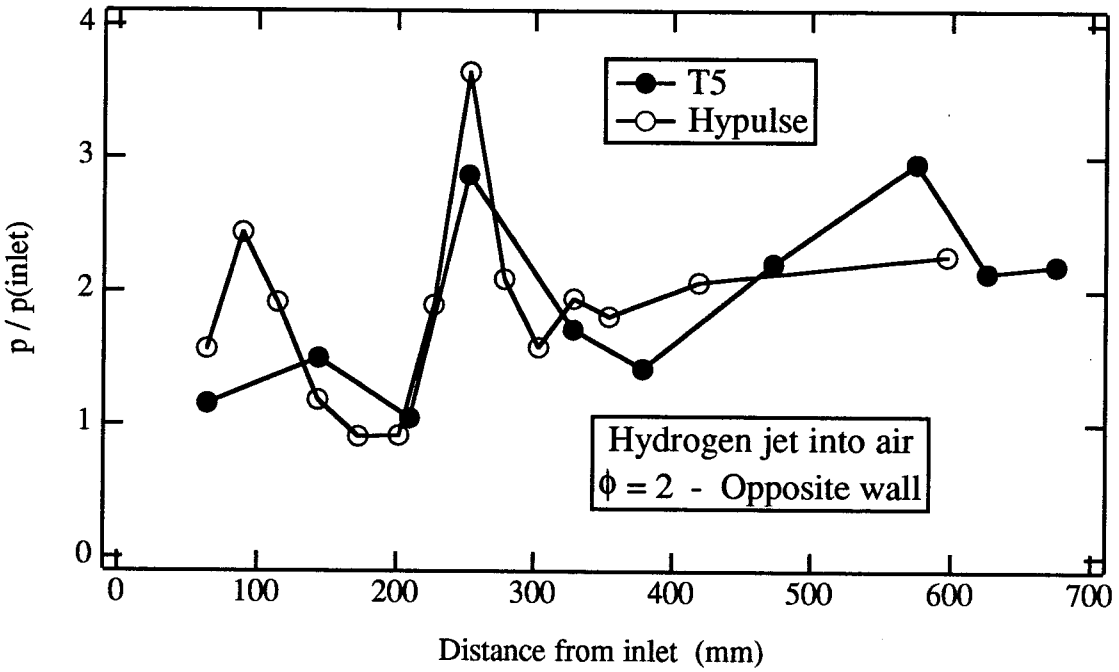

Figure 6.12 Pressure measurements on the opposite wall for the low pressure case in air with a fuel equivalence ratio of 2. The plot compares results from HYPULSE and the present work. The injector is 177 mm from the inlet.

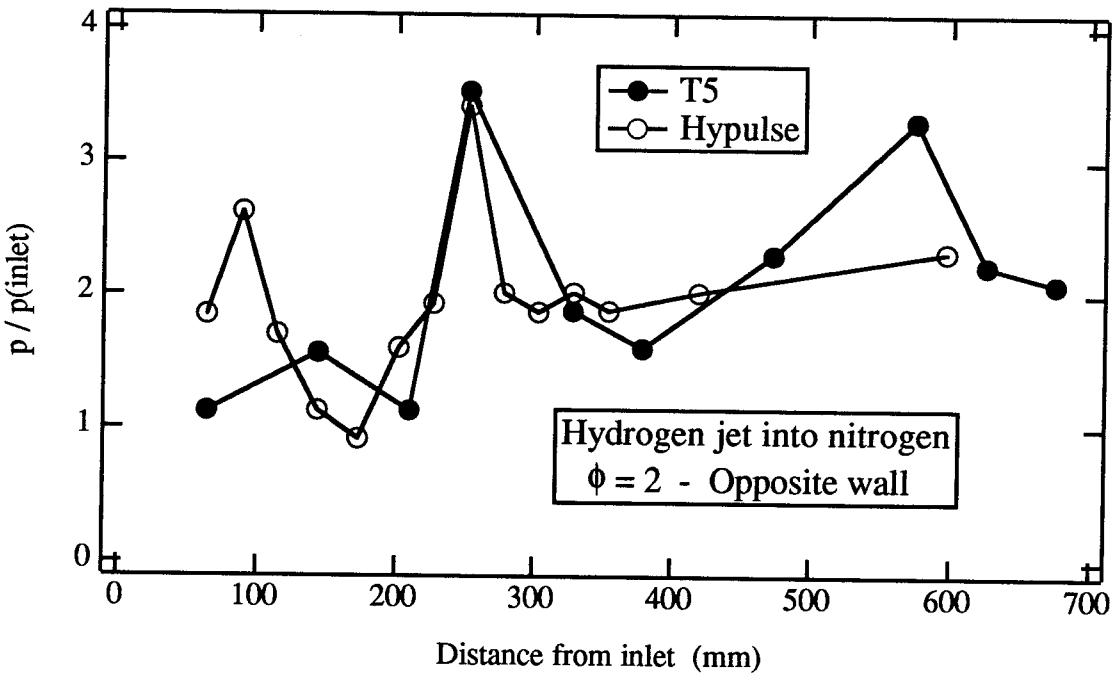

Figure 6.13 Pressure measurements on the opposite wall for the low pressure case in nitrogen with a fuel equivalence ratio of 2. The plot compares results from HYPULSE and the present work. The injector is 177 mm from the inlet.

6.4.2 Combustion Analysis

One of the main goals of these experiments has been to determine if it is possible to burn the hydrogen before it exits the combustor. To do so, combustion tests in air and non-combustion tests in nitrogen will be compared. As was shown in table 6.2, the static pressure in the air flow is expected to be 10% higher than the one in nitrogen due to the real gas effects in the nozzle of T5. Figure 6.14 shows the measured pressure ratio between the air and nitrogen flow for the low pressure case with no injection. The pressure ratio is very close to the expected value of 1.1 and stays at that level along the whole length of the combustor.

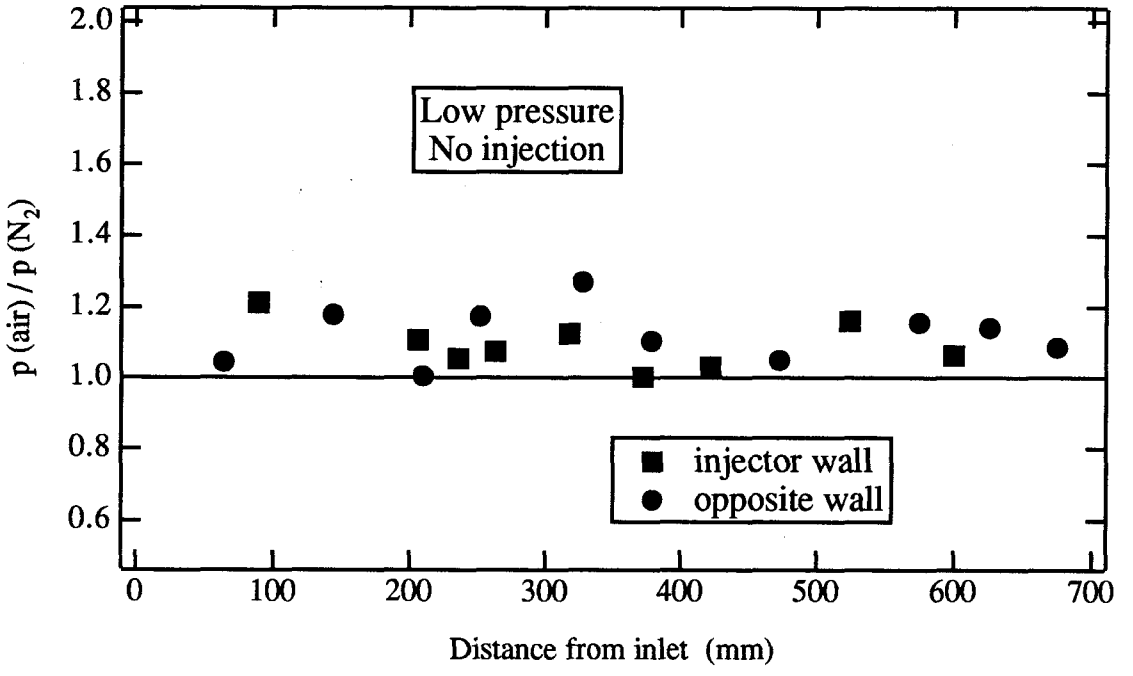

Figure 6.14 Pressure ratio between the air and nitrogen flow for the low pressure case with no injection.

Figures 6.15 and 6.16 show the pressure ratio between air and nitrogen flows for the two sets of experiments with cold injection, figure 6.15 for the tests with the fuel equivalence ratio of 1, and figure 6.16 for those with the fuel equivalence ratio of 2. The pressure level for each one of the injection conditions and for each test gas is determined

using an average over two experiments. The worst case error bar for those pressure ratios is estimated at ± 0.15.

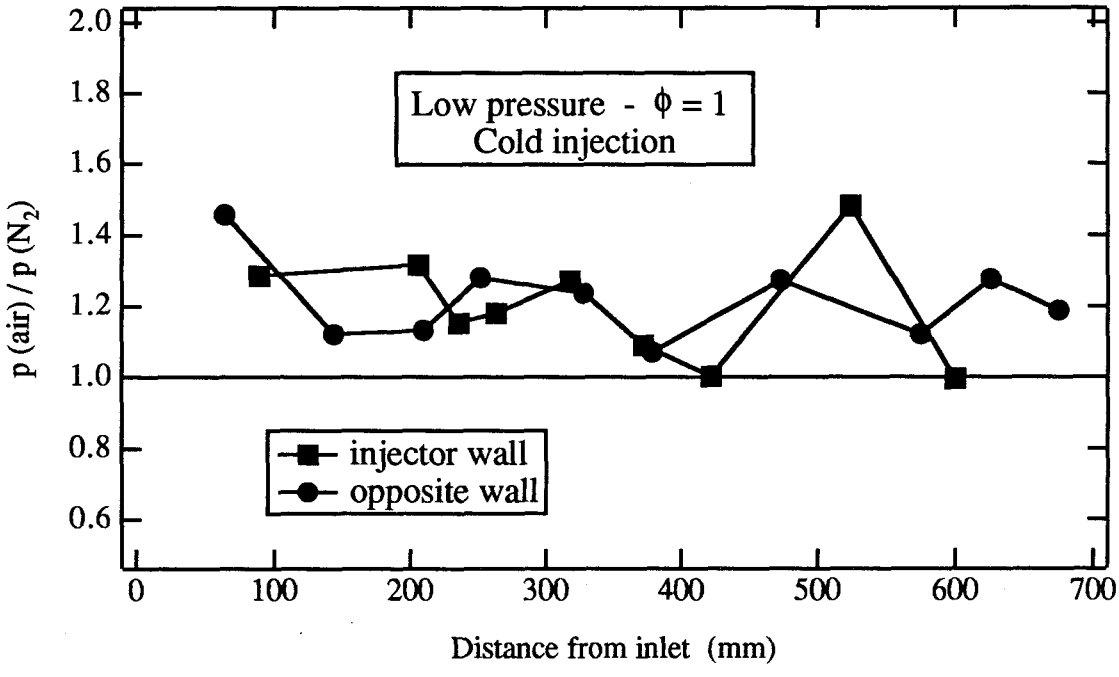

Figure 6.15 Pressure ratio between the air and nitrogen flow for the low pressure case with cold hydrogen injection with fuel equivalence ratio of 1.

Figure 6.15 shows, for the fuel equivalence ratio of 1, a net increase from the pressure ratio of 1.1 seen in the no injection case. It is rather hard to determine exactly what the pressure ratio is at the exit of the combustor, but a fair approximation should be around 1.3. To determine how much fuel has burned to produce this pressure rise, a simple one-dimensional flow approximation with heat addition will be used here. A better approximation is not felt necessary at this time because of the investigation now underway with these flows at NASA Langley with the 3-D SPARK code.

With this 1-D approximation, if all the fuel could be burned, heat addition of about 3.2 MJ/kg of air could be added to the flow. This addition would result in a Mach number at the end of the combustion of close to 3.25 and a pressure ratio between the initial and final pressure of 2.5. But the pressure rise due to the boundary layers must also be taken into account to evaluate the final pressure ratio. With an initial pressure of 16

kPa for air and 14 kPa for nitrogen and a increase of 12 kPa due to the boundary layer, the expected final pressure ratio would be ((2.5 x 16) + 12) / (14 + 12) = 2.0. But according to Riggins et al. (1992b), who ran this particular test numerically before with the 3-D SPARK code, only 20% of the combustion should be completed after 600 mm. Taking this combustion approximation into the simple model, a pressure ratio of 1.3 is calculated, making the final pressure ratio ((1.3 x 16) + 12) / (14 + 12) = 1.26. This pressure ratio is close to the one measured in the present experiments.

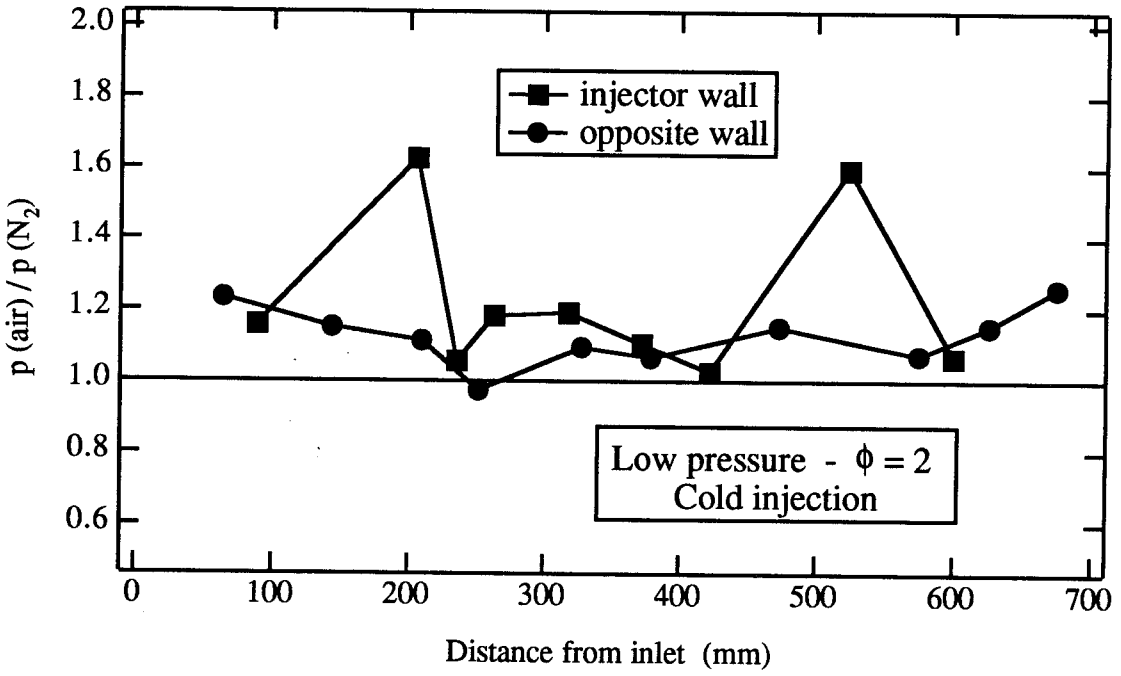

Figure 6.16 Pressure ratio between the air and nitrogen flow for the low pressure case with cold hydrogen injection with fuel equivalence ratio of 2.

Figure 6.16 shows the results for the fuel equivalence ratio of 2. The pressure ratio rise is not as clear as in figure 6.15, but can probably be put at about 1.2. This somewhat lower combustion efficiency probably comes from the rather large uncertainty in the pressure measurement coupled with a small pressure rise expected from these combustion tests. But once again, this value of 1.2 is close to that predicted by the 3-D model and well within the error bars compared to the tests with the fuel equivalence ratio of 1. It is important to point out here that the very large pressure ratio of 1.6 measured on the

injector wall at 525 mm from the inlet was a very consistent measurement, making the combustion very significant in that region of the flow.

Figure 6.17 presents the pressure ratio results for the low pressure case with hot injection at a fuel equivalence ratio of 2. Even if some of the pressure ratios are very high in the first part of the combustor, the ratios seem to settle rapidly to about 1.1, a value indicating that no significant combustion occurred in these tests. This result corroborates one of the results presented in chapter 5 because this flow condition is very close to the low pressure-high enthalpy case presented in that chapter, where no significant combustion was detected.

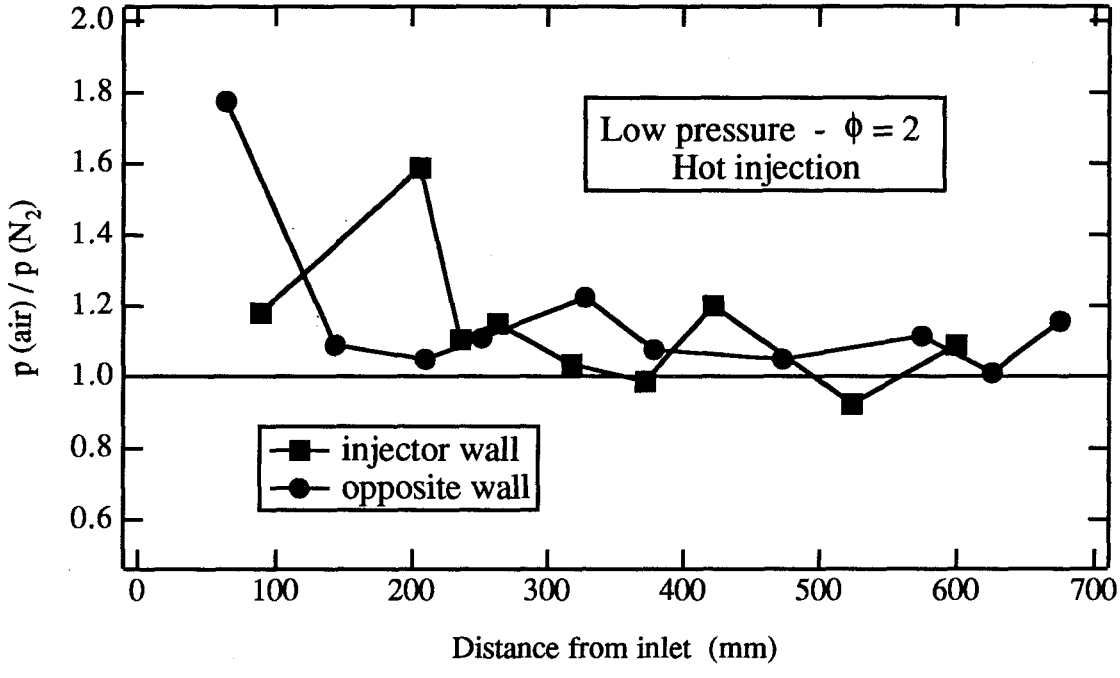

Figure 6.17 Pressure ratio between the air and nitrogen flow for the low pressure case with hot hydrogen injection and fuel equivalence ratio of 2.

The fact that the hydrogen at the exit of the injector is almost 800 K for the hot injection case may leave the impression that it would burn better than the cold injection case. But a close look at the problem shows two important facts. First, in the hot hydrogen case, the hydrogen velocity is about 3600 m/s compared to 1700 m/s for the cold case, making the shear layer much less effective in mixing the hydrogen and the

4600 m/s air flow. The second point is the time residency of the fuel in the combustor. The hot fuel stays in the combustor only 200 μs, half the residence time of the cold fuel.

It is a very difficult task to try to measure a variation of pressure of about 5 kPa due to a 20% hydrogen combustion when, at the same time, the pressure rise due to the boundary layer in the combustor is about 12 kPa. This problem is much less severe in the second set of experiments done at high pressure. With a static pressure of about 40 kPa, a 20% hydrogen combustion would cause a pressure rise of about 12 kPa, about the same as the 14 kPa due to the boundary layer. Another advantage is the increased density, making the combustion rate much faster. All these high pressure tests were done with hot hydrogen injection, making it more difficult for the combustor to burn the fuel according to the previous results.

Figure 6.18 presents the pressure ratio for the no-injection tests between the air and the nitrogen flows in the high pressure case. The results show the expected pressure ratio of 1.1.

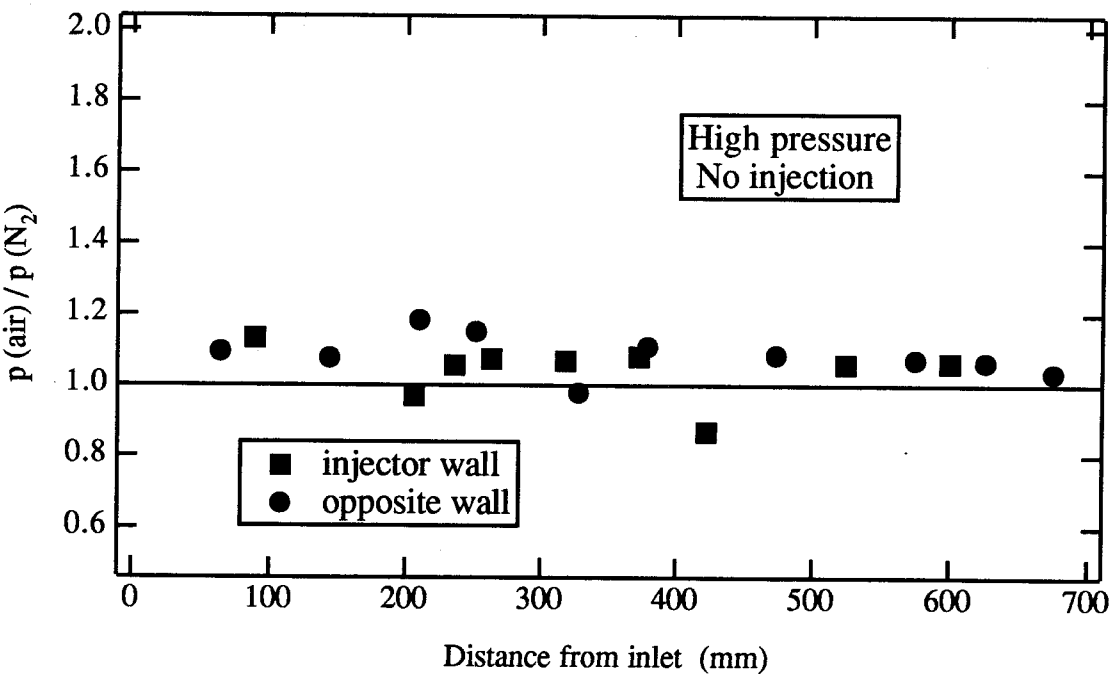

Figure 6.18 Pressure ratio for the no-injection tests in the high pressure case, with the typical pressure ratio of 1.1 between the air and the nitrogen flows.

As was mentioned before and is not clearly shown here, the total pressure increase along the combustor in this case is about 14 kPa. Because the Reynolds number is estimated at about 3 x 10^6 at the exit of the combustor in this case, the boundary layer is most likely turbulent in part of the combustor. This transition from laminar to turbulent could explain why the relative pressure rise due to the boundary layer is much less in this case than in the low pressure one. The displacement thickness of this turbulent boundary layer is smaller than its laminar counterpart under the present conditions.

Figures 6.19 and 6.20 show the results for the injection with fuel equivalence ratios of 1 and 2, respectively. The case with a fuel equivalence ratio of 1 shows a small pressure ratio increase compared to the no-injection case presented in figure 6.18. The pressure ratio may have reached a value of about 1.25. Using the simple 1-D approximation, a combustion pressure ratio of 1.2 would give a final pressure ratio of (1.2 x 40 +14) / (36 + 14) = 1.24. This represents a combustion of about 15% of the hydrogen.

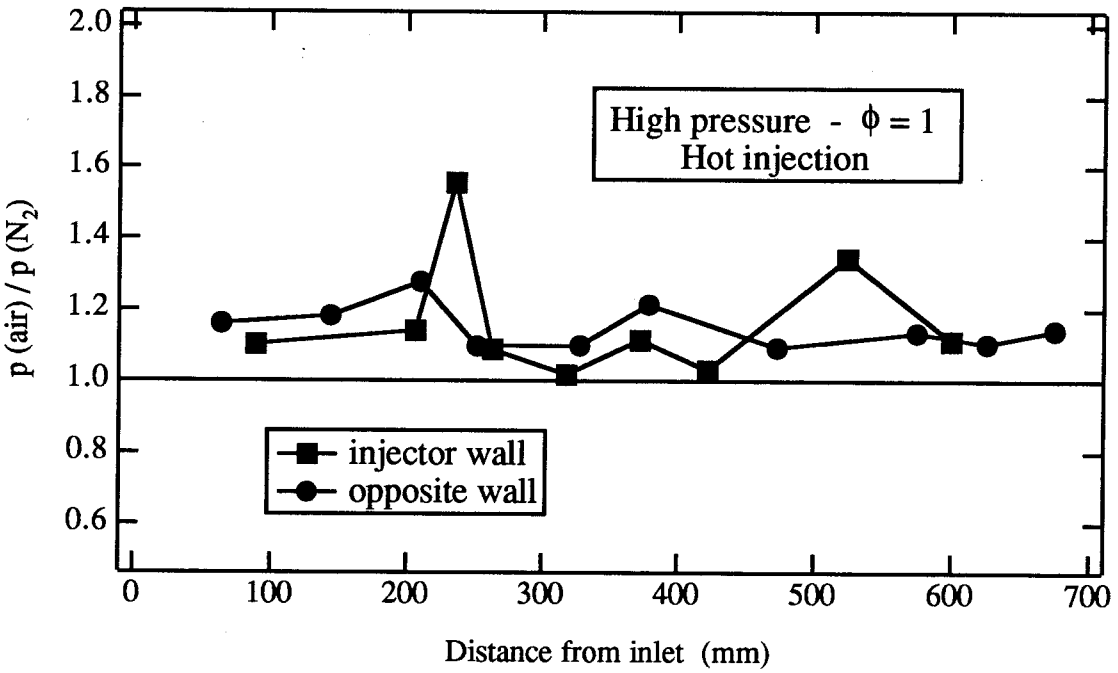

Figure 6.19 Pressure ratio between the air and nitrogen flows for the high pressure case with hot hydrogen injection and fuel equivalence ratio of 1.

The case with the fuel equivalence ratio of 2 shown in figure 6.20 shows a much more significant pressure ratio rise. The value of the ratio here is about 1.6 at the exit of the combustor, making the combustion efficiency using the 1-D model about 40%. This is a very large percentage taking into account the fact that the fuel stays in the combustor only 200 μs, since according to Dimotakis and Hall (1987), the complete combustion should take more than 1 ms. It is possible that a significant portion of this combustion occurs in the boundary layer of the combustor where the time residency of the fuel is much longer and also where the temperature of the air is higher, making the combustion rate go up. There is also some evidence, and it will be presented in the next section, that some of the combustion occurred in the bow shock region.

Dimotakis and Hall also discuss the fact that for high enthalpy flows like the one tested here, the temperature rise is much less than the one predicted by the simple 1-D model. This is due to a significant participation of energetic species in the final equilibrium population.

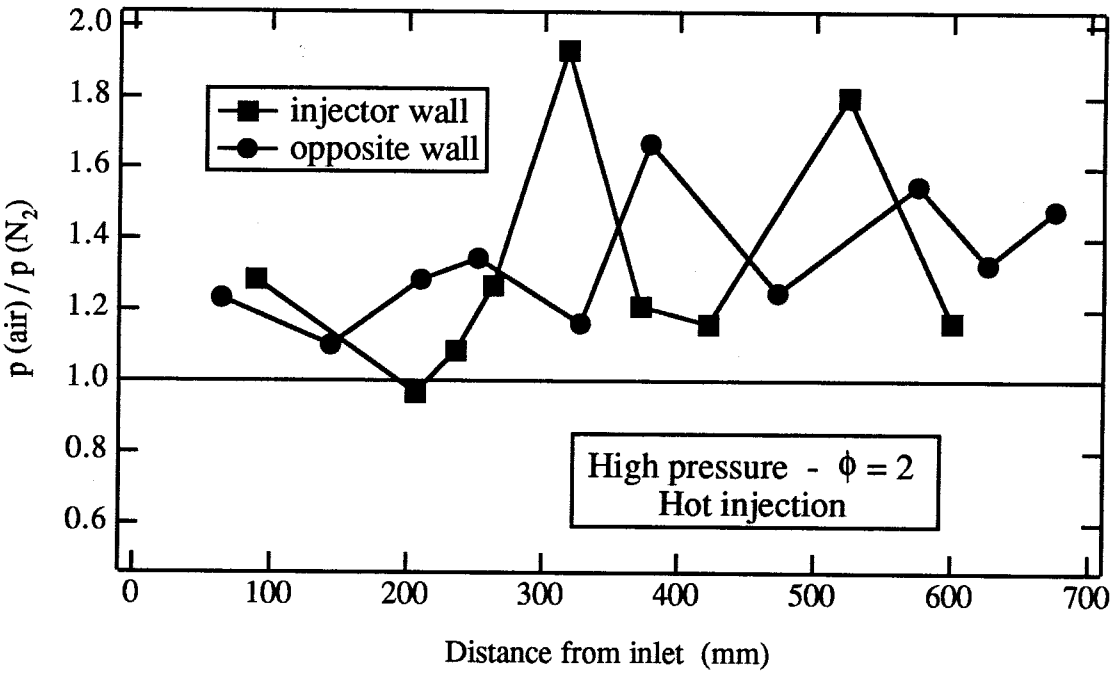

Figure 6.20 Pressure ratio between the air and nitrogen flows for the high pressure case with hot hydrogen injection and fuel equivalence ratio of 2.

6.4.3 Flow Visualization

In the next three pages, flow visualization pictures obtained with the simple differential interferometry system and the increased sensitivity system using resonant enhancement are presented. Information on the position of the bow shock and its subsequent reflections as well as the jet penetration height will be used to correlate the numerical simulations now underway at NASA Langley.

The cases presented here are first the low pressure ones with cold injection for a fuel ratio of 1 and 2 in air in figures 6.21 and 6.22, respectively. It is possible to see in those pictures the bow shock and its reflection on the opposite wall. The definition of the reflected shock is not very good due to the 3-D shape of the shock. The fuel penetration into the main flow is also very well defined in those two flows.

Figures 6.23 and 6.24 are from the low pressure, hot hydrogen case in air and in nitrogen. The difference between the differential interferogram and the resonantly enhanced interferogram can be seen here. The shock position is better defined with the differential interferogram, but the position and the structure of the jet is much clearer with the resonantly enhanced interferogram presented in figure 6.24. The higher penetration of the jet compared to the cold injection is due to a higher static pressure of the jet at the exit of the injector.

Finally, figures 6.25 and 6.26 show the flow visualization for the high pressure tests with a fuel ratio of 2 in air and in nitrogen, respectively. These are the two best pictures taken during these combustor experiments. They were taken at the same time, and the stagnation conditions of the combustion driven shock tunnel and T5 were the same within a margin of error of 2%. Even with all these similar conditions, these air and nitrogen flows are quite different. The penetration of the jet seems much stronger in the air flow, but, most importantly, the large structures on the interface of the jet and the main flow do not show the same length scale. The nitrogen flow in figure 6.26 shows large structures with characteristic length of about 4 mm, where the structures in the air flow of figure 6.25 show much smaller structure scales.

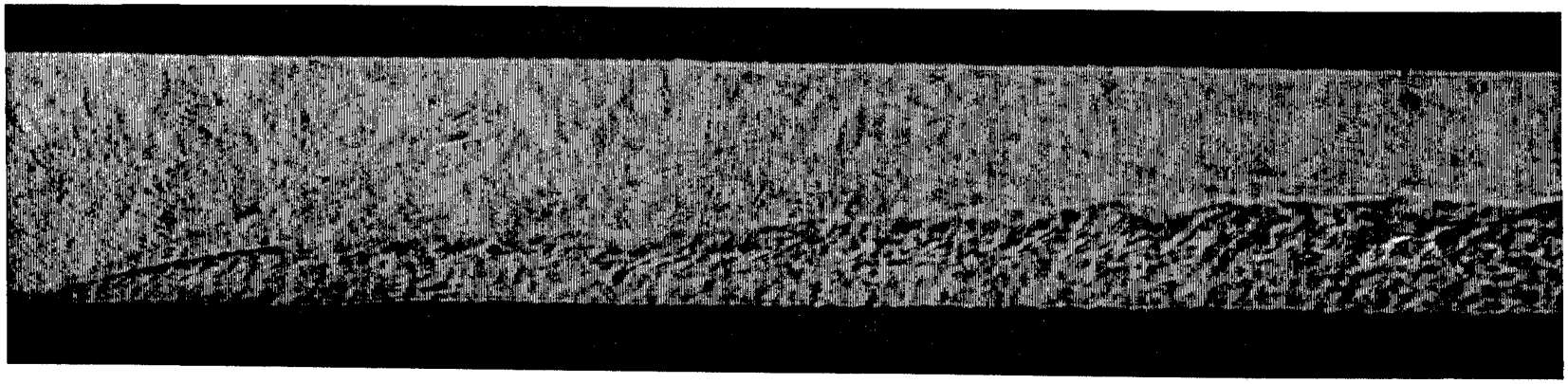

Figure 6.21 Resonantly enhanced interferogram of the low pressure case in air with cold hydrogen injection and a fuel equivalence ratio of 1. The combustor cross section is 25.4 mm and the 15° flush wall injector exit extends 21.4 mm downstream of the initial bow shock position.

Figure 6.22 Resonantly enhanced interferogram of the low pressure case in air with cold hydrogen injection and a fuel equivalence ratio of 2. The combustor cross section is 25.4 mm and the 15° flush wall injector exit extends 21.4 mm downstream of the initial bow shock position.

Figure 6.23 Differential interferogram of the low pressure case in air with hot hydrogen injection and a fuel equivalence ratio of 2. The combustor cross section is 25.4 mm and the 15° flush wall injector exit extends 21.4 mm downstream of the initial bow shock position.

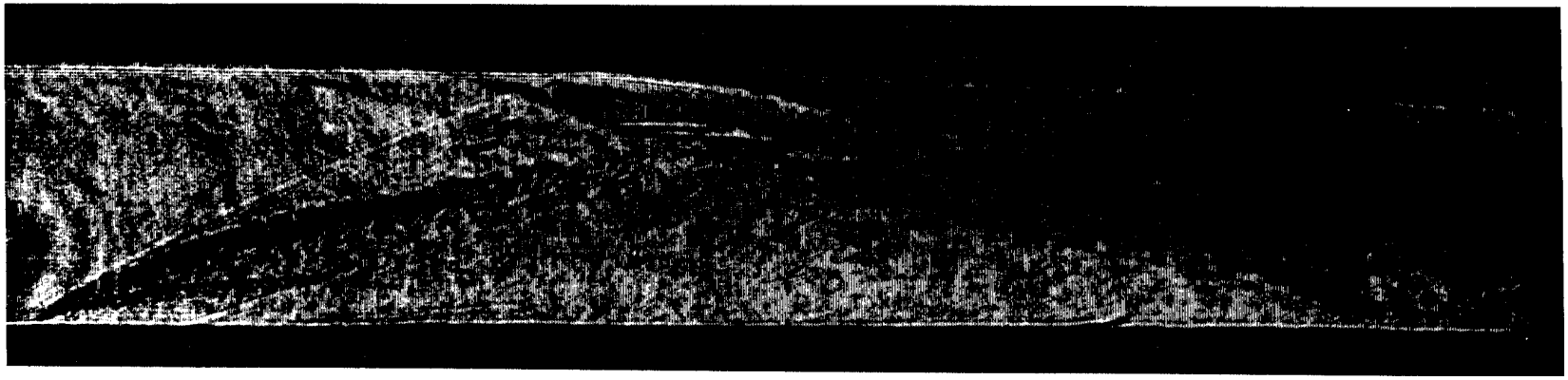

Figure 6.24 Resonantly enhanced interferogram of the low pressure case in nitrogen with hot hydrogen injection and a fuel equivalence ratio of 2. The combustor cross section is 25.4 mm and the 15° flush wall injector exit extends 21.4 mm downstream of the initial bow shock position.

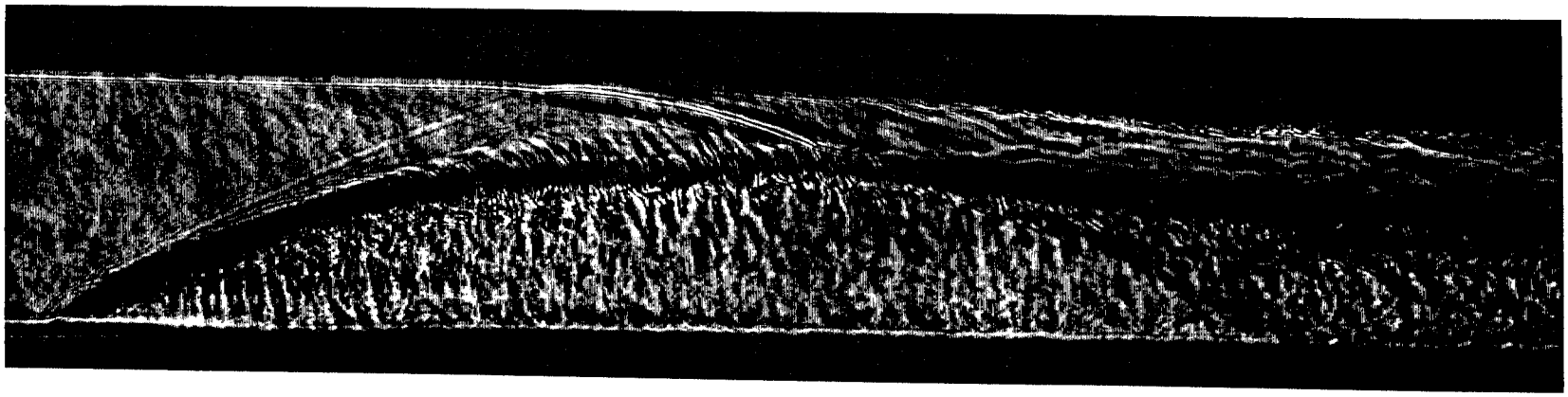

Figure 6.25 Resonantly enhanced interferogram of the high pressure case in air with hot hydrogen injection and a fuel equivalence ratio of 2. The combustor cross section is 25.4 mm and the 15° flush wall injector exit extends 21.4 mm downstream of the initial bow shock position.

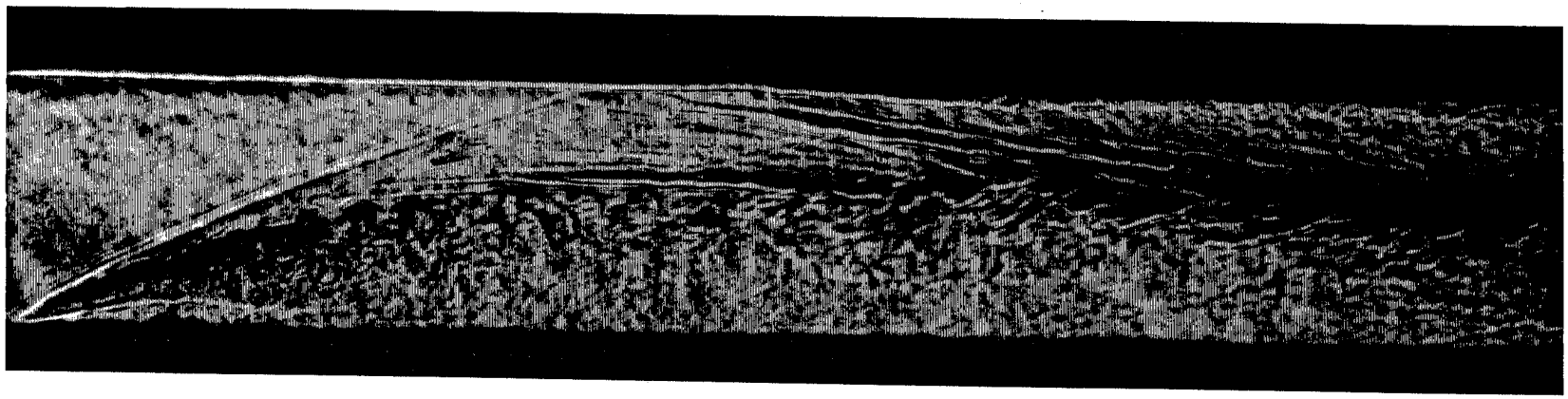

Figure 6.26 Resonantly enhanced interferogram of the high pressure case in nitrogen with hot hydrogen injection and a fuel equivalence ratio of 2. The combustor cross section is 25.4 mm and the 15° flush wall injector exit extends 21.4 mm downstream of the initial bow shock position.

According to Hermanson and Dimotakis (1989), this difference in the length scale of the structures is probably due to a significant heat release at the interface of the jet and the main flow. For the case of a shear layer, they have shown experimentally that the growth rate of the shear layer thickness decreases with increasing heat release, and at the same time, the size of the large structure inside the shear layer decreases with respect to the shear layer thickness as the heat release increases. These two effects add up to significantly reduce the size of the large structures for the cases where combustion occurred.

6.5 Conclusion

There is very good agreement between the HYPULSE test results and those performed in the T5 facility. No significant effects of the relatively large quantities of dissociated oxygen and NO in the T5 flow have been detected compared to the "clean-air" HYPULSE expansion tube flow.

It is believed that about 20% of the fuel was burned in the combustor in the low pressure case with cold injection. In the case of the low pressure with hot injection, there is no trace of significant combustion. Up to 40% of the fuel was burned before exiting the combustor in the tests with the fuel equivalence ratio of 2 in the high pressure case. The flow visualization in that case also confirms that some combustion occurred in the bow shock region of the flow. The combustion efficiency for the tests with the fuel equivalence ratio of 1 is significantly less, probably around 15%.

The flow visualization pictures, combined with the pressure measurements, will be very valuable for the validation of the numerical runs underway at NASA Langley.

Chapter 7
Conclusion

The ability to build an air-breathing single-stage-to-orbit propulsion system requires examination of key elements such as fuel penetration, turbulent mixing rates, especially at the "zero shear" fuel-air mixing condition, and combustion efficiency. The required data can only be obtained in experiments which simultaneously match the flight total pressure and total enthalpy as well as the fuel conditions. Starting from there, the basic guidelines for this research were drawn.

First, it was felt that there was a need to simulate the gas dynamical processes in the free piston shock tunnel and later in the combustion driven shock tunnel so that both systems could be used as efficiently as possible. The numerical code helped explain the piston motion in the driver section of the free piston shock tunnel and has also indicated that the drop in the shock speed is not due to the rate of pressure drop in the driver section but to very significant viscous losses in the driven section. The code was also very useful for the design of the combustion driven shock tunnel.

Because the hydrogen has to be injected into the combustion chamber of the propulsion system after being used as a cooling fluid, the combustion driven shock tunnel was built to reproduce this "hot" hydrogen fuel. All the problems related to the tunnel were solved and the system has been used successfully to supply hydrogen at up to 1500 K for the combustion experiments. The viscous effects in the tunnel are believed to be responsible for its lower than predicted overall efficiency.

To reduce the complexity of the problem, and give a better insight into the combustion process, a very basic configuration for the hydrogen injection system was tested. This was first done with an injection system mounted flush with the surface of a

flat plate in the test section of T5. Different test conditions as well as Mach 2 and 5 nozzle injectors at angles of 15^{o} or 30^{o} were tested to determine criteria for significant combustion. Lower limits in pressure and enthalpy were found where hydrogen combustion becomes very limited using this "hot" hydrogen fuel.

The second set of experiments still used an injection system mounted flush with the surface but involved a small combustor model previously tested in the hypervelocity expansion tube facility HYPULSE. The 15^{o}, Mach 1.7 injector nozzle exits into a rectangular combustor with a cross section of 50.8 mm by 25.4 mm and length of 711 mm. Low pressure experiments were performed to reproduce some of the HYPULSE tests and the agreement is excellent. Experiments at high pressure were also performed to better match the real flight total pressure and significant hydrogen combustion was detected in these tests both with the pressure transducers and the flow visualization technique.

All the combustion experiments presented here and performed in T5 with the new combustion driven shock tunnel were mostly exploratory ones. Efforts are now underway to improve the flow visualization and the diagnostic techniques to hopefully get better quantitative results in future experiments.

References

Anderson, G., A. Kumar, and J. Erdos (1990); "Progress in Hypersonic Combustion Technology with Computation and Exeriment," AIAA 2nd International Aerospace Planes Conference, AIAA 90-5254, Orlando, Florida, October 29-31.

Anderson, John D. Jr. (1982); *Modern Compressible Flow with Historical Perspective*, McGraw-Hill Book Company.

Anderson, John D. Jr. (1989); *Hypersonic and High Temperature Gas Dynamics*, McGraw-Hill Book Company.

Aso, S., S. Okuyama, M. Kawai, and Y. Ando (1991); "Experimental Study on Mixing Phenomena in Supersonic Flows with Slot Injection," AIAA 29th Aerospace Sciences Meeting, AIAA 91-0016, Reno, Nevada, January 7-10.

Avallone, Eugene A., and Theodore Bannierster III (1987); *Standard Handbook for Mechanical Engineers*, McGraw-Hill Book Company, Ninth Edition.

Bakos, R. J., J. Tamagno, O. Rizkalla, M. V. Pulsonetti, W. Chinitz, and J. I. Erdos (1992a); "Hypersonic Mixing and Combustion Studies in the Hypulse Facility," *Journal of Propulsion and Power*, Vol. 8, No. 4, July-Aug., pp. 900-906.

Bakos, R. J., J. Tamagno, R. Trucco, O. Rizkalla, W. Chinitz, and J. I. Erdos (1992b); "Mixing and Combustion Studies Using Discrete Orifice Injection at Hpervelocity Flight Conditions," *Journal of Propulsion and Power*, Vol. 8, No. 6, Nov.-Dec., pp. 1290-1296.

Bakos, R. J., R. G. Morgan, and J. Tamagno (1992c); "Effects of Oxygen Dissociation on Hypervelocity Combustion Experiments," AIAA 17th Aerospace Ground Testing Conference, AIAA 92-3964, Nashville, Tennessee, July 6-8.

Bélanger, Jacques (1990); "Description and Use of a Computer Program for Unsteady One-Dimensionnal Calculations of Shock Tunnel Processes," GALCIT Report FM90-3, October.

Becker, Ernst (1965); *Gasdynamik*, Teubner Verlagsgesellschaft GmbH, Stuttgart.

Bobskill, G., R. Bittner, D. Riggins, and C. McClinton (1991); "CFD Evaluation of Mach 17 HYPULSE Scramjet Combustor Data," AIAA 3rd International Aerospace Planes Conference, AIAA 91-5093, Orlando, Florida, December 3-5.

Boeing (1990); "Boeing 30 Inch Hypersonic Shock Tunnel," Private Publication, June 19.

Casey, R. T., R. J. Stalker, and C. Brescianini (1992); "Hydrogen Combustion in a Hypersonic Airstream," *Aeronautical Journal*, Vol. 96, No. 955, May, pp. 200-202.

Correa, S. M., R. E. Warren, F. F. Haler, and W. O. Kaiser (1990); "Supersonic Combustion of Hydrogen Jets Behind a Backward-Facing Step," AIAA 28th Aerospace Sciences Meeting, AIAA 90-0204, Reno, Nevada, January 8-11.

Dimotakis, P. E., and J. L. Hall (1987); "A Simple Model for Finite Chemical Kinetics Analysis of Supersonic Turbulent Shear Layer Combustion," AIAA/SAE/ASME/ASEE 23rd Joint Propulsion Conference, AIAA 87-1879, San Diego, California, June 29-July 2.

Eitelberg, G., T. J. McIntyre, and W. H. Beck (1992); "The High Enthalpy Shock Tunnel in Göttingen," AIAA 17th Aerospace Ground Testing Conference, AIAA 92-3942, Nashville, Tennessee, July 6-8.

Fletcher, D. G., and J. C. McDaniel (1989); "Laser-Induced Iodine Fluorescence Technique for Quantitative Measurement in a Nonreacting Supersonic Combustor," *AIAA Journal*, Vol. 27, No. 5, May, pp. 575-580.

Fujimori, T., M. Kawai, H. Ikeda, Y. Ando, Y. Ohmori, S. Aso, and M. Fukuda (1991); "Numerical Prediction of Two and Three Dimensional Sonic Gas Transverse Injections Into Supersonic Flow," AIAA 29th Aerospace Sciences Meeting, AIAA 91-0415, Reno, Nevada, January 7-10.

Germain, P., E. Cummings, and H. Hornung (1993); "Transition on a Sharp Cone at High Enthalpy; New Measurements in the Shock Tunnel T5 at GALCIT," AIAA 31st Aerospace Sciences Meeting & Exhibit, AIAA 93-0343, Reno, Nevada, January 11-14.

Heister, S. D., and A. R. Karagozian (1990); "Gaseous Jet in Supersonic Crossflow," *AIAA Journal*, Vol. 28, No. 5, May, pp. 819-827.

Hermanson, J. C., and P. E. Dimotakis (1989); "Effects of Heat Release in a Turbulent, Reacting Shear Layer," *Journal of Fluid Mechanics*, Vol. 199, pp. 333-375.

Hornung, Hans G. (1988); "The Piston Motion in a Free-Piston Driver for Shock Tubes and Tunnels," GALCIT Report FM88-1, January.

Hornung, H. G., and J. Bélanger (1990); "Role and Techniques of Ground Testing for Simulation of Flows Up to Orbital Speed," AIAA 16th Aerodynamic Ground Testing Conference, Seattle, Washington, June 18-20.

Hornung, H. G., B. Sturtevant, J. Bélanger, S. Sanderson, M. Brouillette, and M. Jenkins (1991); "Performance Data of the New Free Piston Shock Tunnel T5 at GALCIT," 18th International Symposium on Shock Wave and Shock Tubes, Sendai, Japan, July 21-26.

Huber, P. W., C. J. Schexnayder, Jr., and C. R. McClinton (1979); "Criteria for Self-Ignition of Supersonic Hydrogen-Air Mixtures," NASA Technical Paper 1457, August.

Jachimowski, Casimir J. (1992); "An Analysis of Combustion Studies in Shock Expansion Tunnels and Reflected Shock Tunnels," NASA Technical Paper 3224, July.

Jacobs, P. A. (1993); "Quasi-One-Dimensional Modelling of Free-Piston Shock Tunnels, 31st Aerospace Sciences Meeting & Exhibit," AIAA 93-0352, Reno, Nevada, January 11-14.

Lacey, John J. Jr., and Dean F. Long (1990); "A Wave Computational Method with Application to a Free-Piston Shock Tunnel," AIAA 16th Aerospace Ground Testing Conference, AIAA 90-1378, Seattle, Washington, June 18-20.

Laster, W. Ray, and Paul E. Sojka (1989); "Autoignition of H_2-Air: The Effect of NO_x Addition," *Journal of Propulsion and Power*, Vol. 5, No. 4, July-Aug., pp. 385-390.

Lee, M. P., B. K. McMillin, J. L. Palmer, and R. K. Hanson (1992); "Planar Fluorescence Imaging of a Transverse Jet in a Supersonic Crossflow," *Journal of Propulsion and Power,* Vol. 8, No. 4, July-Aug..

Lee, R. E., and M. J. Linevsky (1990); "Shadowgragh Studies of Angular Injection of a Sonic Jet Into a Mach 2.8 Supersonic Flow," AIAA 21st Fluid Dynamics, Plasma Dynamics and Lasers Conference, AIAA 90-1618, Seattle, Washigton, June 18-20.

Liepmann, Hans W., and Anatol Roshko (1957); *Elements of Gasdynamics*, John Wiley & Sons Inc.

Loomis, Mark P., H. A. Zambrana, D. W. Bogdanoff, T. C. Tam, J. A. Cavolowsky, M. E. Newfield, and R. D. Bittner (1992); "30 Degree Injectors at Hypervelocity Conditions," AIAA/SAE/ASME/ASEE 28th Joint Propulsion Conference and Exhibit, AIAA 92-3288, Nashville, Tennessee, July 6-8.

Lordi, J. A., R. E. Mates, and J. R. Mosella (1965); "Computer Program for the Numerical Solution of Nonequilibrium Expansions of Reacting Gas Mixtures," Contract No NASr-109, Cornell Aeronautical Laboratory Inc., Buffalo, N.Y.

Lukasiewicz, J. (1973); *Experimental Methods of Hypersonics*, Gasdynamics Series Volume 3, Marcel Dekker Inc.

Maus, J., M. Laster, and H. Hornung (1992); "The G-Range Impulse Facility A High-Performance Free-Piston Shock Tunnel," AIAA 17th Aerospace Ground Testing Conference, AIAA 92-3946, Nashville, Tennessee, July 6-8.

Mays, R. B., R. H. Thomas, and J. A. Schetz (1989); "Low Angle Injection Into a Supersonic Flow," AIAA/ASME/SAE/ASEE 25th Joint Propulsion Conference, AIAA 89-2461, Monterey, California, July 10-12.

McIntosh, M. K. (1971); ESTC Program ("Equilibrium Shock Tube Calculation"), WRE-Tech Note 180, Australian Defence Scientific Service, Weapons Research Establishment, Salisbury, South Australia.

McClinton, Charles R. (1972); "The Effect of Injection Angle on the Interaction Between Sonic Secondary Jets and a Supersonic Free Stream," NASA TN D-6669, February.

McDaniel, J. C., and J. Graves, Jr. (1986); "A Laser-Induced-Fluorescence Visualization Study of Transverse, Sonic Fuel Injection in a Nonreacting Supersonic Combustor," AIAA 24th Aerospace Sciences Meeting, AIAA 86-0507, Reno, Nevada, January 6-9.

Morgan, R. G., and Casey R. (1990); "Supersonic Combustion with Transverse, Circular Wall Jets," NASA Contractor Report 182096, October, pp. 20-39.

Morrison, W. R. B., R. J. Stalker, and J. Duffin (1989); "New Generation of Free-Piston Shock Tunnels," 17th International Symposium on Shock Waves, Bethlehem, Pennsylvania, July 17-21.

Nagamatsu, H.T., R. E. Sheer, Jr., L. A. Osburg, and K. H. Cary (1961); "Design Features of the General Electric Research Laboratory Hypersonic Shock Tunnel," GE Research Laboratory Report No. 61-RL-2711C, May.

Orth, Richard C., and John A. Funk (1967); "An Experimental and Comparative Study of Jet Penetration in Supersonic Flow," *Journal of Spacecraft and Rockets*, Vol. 4, No. 9, September, pp. 1236-1242.

Papamoschou, D., D. G. Hubbard, and M. Lin (1991); "Observations of Supersonic Transverse Jets," AIAA 22st Fluid Dynamics, Plasma Dynamics and Lasers Conference, AIAA 91-1723, Honolulu, Hawaii, June 24-26.

Parker, T. E., M. G. Allen, S. J. Davis, K. Donohue, R. R. Foutter, H. H. Legner, W. T. Rawlins, and Wm. G. Reinecke (1992); "Optical Diagnostics in Supersonic Combusting Systems," Wright Laboratory Report WL-TR-91-2101, April.

Quan, V., D. M. Smith, A. B. Mathur, and R. B. Edelman (1990); "A Three-Dimensional Approach for Analysis of Sidewall Injector Mixing and Combustion," AIAA 2nd International Aerospace Planes Conference, AIAA 90-5243, Orlando, Florida, October 29-31.

Rein, Martin (1989); SURF : "A Program for Calculating Inviscid Supersonic Reacting Flows in Nozzles," GALCIT Report FM89-1, November.

Riggins, D. W., and C. R. McClinton (1991); "Analysis of Losses in Supersonic Mixing and Reacting Flows," AIAA/ASME/SAE/ASEE 27th Joint Propulsion Conference, AIAA 91-2266, Sacramento, California, June 24-26.

Riggins, D. W., and C. R. McClinton (1992a); "A Computational Investigation of Mixing and Reacting Flows in Supersonic Combustor," AIAA 30th Aerospace Sciences Meeting & Exibit, AIAA 92-0626, Reno, Nevada, January 6-9.

Riggins, D. W., C. R. McClinton, R. C. Rogers, and R. D. Bittner (1992b); "A Comparative Study of Scramjet Injection Strategies for High Mach Number Flows," AIAA/SAE/ASME/ASEE/ 28th Joint Propulsion Conference and Exhibit, AIAA 92-3287, Nashville, Tennessee, July 6-8.

Rogers, R. Clayton (1971); "A Study of the Mixing of Hydrogen Injected Normal to a Supersonic Airstream," NASA TN D-6114, March.

Roshko, Anatol (1960); "On Flow Duration in Low-Pressure Shock Tubes," *Physics of Fluids*, Vol. 3, No. 6, Nov.-Dec., pp. 835-842.

Rothstein, A. D., and P. J. Wantuck (1992); "A Study of the Normal Injection of Hydrogen Into a Heated Supersonic Flow Using Planar Laser-Induced Fluorescence," AIAA/SAE/ASME/ASEE 28th Joint Propulsion Conference and Exhibit, AIAA 92-3423, Nashville, Tennessee, July 6-8.

Schetz, Joseph A., and Frederick S. Billig (1966); "Penetration of Gaseous Jets Injected Into a Supersonic Stream," *Journal of Spacecraft and Rockets*, Vol. 3, No. 11, September, pp. 1658-1665.

Schetz, J. A., R. Weinraub, and R. Mahaffey (1968); "Supersonic Transverse Jets in a Supersonic Stream," *AIAA Journal*, Vol. 6, May, pp. 933-934.

Segal, C., J. C. McDaniel, R. H. Krauss, and R. B. Whitehurst III (1991); "Combustion Efficiency Determined from Wall Pressure and Temperature Measurement in a Mach 2 Combustor," AIAA 29th Aerospace Sciences Meeting, AIAA 91-0017, Reno, Nevada, January 7-10.

Stalker, R. J. (1989); "Recent Developments with Free Piston Drivers," 17th International Symposium on Shock Waves, Bethlehem, PA, July 17-21.

STANJAN Chemical Equilibrium Solver (1987); (c) Stanford University, V 3.89 VAX.

Sturtevant, Bradford (1989); Non-Steady Gasdynamics, course notes, GALCIT, Jan.-Mars.

Takahashi, M., and A. K. Hayashi (1991); "Numerical Study on Mixing and Combustion of Injecting Hydrogen Jet in a Supersonic Air Flow," AIAA 29th Aerospace Sciences Meeting, AIAA 91-0574, Reno, Nevada, January 7-10.

Uenishi, K., R. C. Rogers, and G. B. Northam (1989); "Numerical Predictions of a Rearward-Facing-Step Flow in a Supersonic Combustor," *Journal of Propulsion and Power*, Vol. 5, No. 2, March-April, pp. 158-164.

Van Driest, E. R. (1952); "Investigation of Laminar Boundary Layer in Compressible Fluids Using the Crocco Method," NACA Tennessee 2597, January.

Wantuck P. J., R. A. Tennant, and H. H. Watanabe (1991); "Supersonic Combustion of a Transverse-Injected H_2 Jet in a Radio-Frequency-Heated Flow," AIAA/SEA/ASME/ASEE 27th Joint Propulsion Conference, AIAA 91-2393, Sacramento, California, June 24-26.

Wendt, M. (1990); "Hot Hydrogen Injection Technique for Shock Tunnels," NASA Contractor Report 182096, October, pp. 86-88.

Zukoski, Edward E., and Frank W. Spaid (1964); "Secondary Injection of Gases into a Supersonic Flow," *AIAA Journal*, Vol. 2, No. 10, October, pp. 1689-1696.